Spring 5-16-2014

X-Ray Structure Analysis and Topological Charge Density Studies of Gossypol Derivatives

Carlos Zelaya
czelaya@uno.edu

X-Ray Structure Analysis and Topological Charge Density Studies of Gossypol Derivatives

Submitted to the Graduate Faculty of the
University of New Orleans
in partial fulfillment of the
requirements for the degree of

A Dissertation

Doctor of Philosophy
in
Chemistry
Physical

by

Carlos A. Zelaya

B.S. University of New Orleans, 2006
B.A. University of New Orleans 2006
M.S. University of New Orleans 2011

May, 2014

Dedication

The following is dedicated to my parents Carlos Alfonso Zelaya Sr. and Dalia Zelaya for their unselfish dedication to their son in all aspects of life. Both of my parents came to the United States, as immigrants, not only to find a better life for themselves but to give their children a greater opportunity for an enriching life. Through their hard work and love, my parents have fulfilled the promise of giving their children a more meaningful life. Without them I would have never had the opportunities offered to me. Without them I would not be. I would also like to dedicate this dissertation to Evelyn, Claudia, and Eric Zelaya. Not only have I been blessed with superb parents but with loving siblings. My love for my daughter, Mia Elisia, who has given me the desire to become a more conscious and humble man. No greater gift can be bestowed upon a man than that of a beautiful child. Mia you have been my greatest joy, and the reason I wish to live my life in full. Most importantly, I dedicate all my work to GOD.

Acknowledgements

I would first like to take the opportunity to thank Dr. Michael Dowd and Professor Edwin Stevens. Dr. Dowd has exhibited a tremendous amount of patience and understanding throughout the years that have made him an excellent mentor. Dr. Dowd's thorough and complete understanding of chemical engineering, crystallography, chemistry, and computational analysis have been impressive. He's ability to examine and solve scientific problems via analysis have had a profound impact on my understanding on what being a scientist entails. Professor Stevens has been a tremendous teacher, mentor, and scientist. His ability to teach mathematics, physics, and its application to physical chemistry, theoretical chemistry, and chemical physics has been exemplary. Professor Stevens' passion for learning is not only integral to his well being but thankfully contagious. I would also like to thank Professor Steve Rick, who has been my principle instructor in the majority of my course work. Dr. Rick always had an open door policy and has taken considerable time, not only to teach but has made sure that I, the student, understood the material thoroughly. Scott Pelitire, from Dr. Dowd's research group, has also taken great care in teaching a multitude of instrumentation, problem solving skills, laboratory techniques, and scientific application. Mr. Pelitire has not only been an outstanding scientist but a genuine friend.

Table of Contents

List of Figures

List of Tables

Abstract

Gossypol and gossypol derivatives are natural byproducts of a variety of cotton plant species that poses interesting chemical, biological, and medicinal properties that are currently heavily researched. Supporting evidence suggest that gossypol and gossypol derivatives act on the Bcl-2 proteins that have been linked to certain cancers. Gossypol amine derivatives, specifically, are actively researched and a variety of amine derivatives have already been synthesized. However, gossypol and its derivatives are challenging compounds to work with because many of its derivatives tend to exist in various tautomeric forms. When analyzing gossypol and its derivatives it is the complex electron configuration that dictates the chemical mechanism and biological activity. The following research provides a charge density study that describes, in detail, the electronic configuration via Bader's topological analysis of di(methoxy)gossypol and di(propylamino) gossypol. In addition, a series of crystallographic studies of gossypol amine derivatives and di(methoxy)gossypol are also analyzed.

Keywords: High resolution X-ray crystallography, topology, charge density studies, gossypol, tautomers, independent atom model

Introduction

Gossypol [1,1',6,6',7,7'-hexahydroxy-5,5'-diisopropyl-3-3'-dimethyl-(2,2'-binaphthalene)-8,8'-dicarboxaldehyde] is a natural occurring compound found in the cotton plant *Gossypium* species that has a multitude of interesting biological, chemical, and crystallographic properties [1,2]. Gossypol has been tested as an oral contraceptive [3], and a number of its derivatives are currently being tested as potential pharmaceutical drugs in human trials [4, 5]. Gossypol acts as a natural insecticide and contains both anti-viral and anti-fungal properties as well [6]. Gossypol contains a number of functional groups that includes six alcohol groups and two aldehyde groups, centered on two naphthalene rings. In addition, gossypol also contains aliphatic side chains consisting of two isopropyl and two methyl groups (Fig. 1.1). The presence of all the functional groups is a primary reason why gossypol exhibits a plethora of biological and chemical activity, and a primary reason why gossypol and its derivatives are currently being studied as potential medicinal agents in a numbers of areas. The structure of gossypol and how it behaves chemically is vital in understanding the pharmacological behavior of this polyphenolic terpene. Crystallographic data provides a very detailed description of the molecular structure of gossypol [7, 8] and further aids in understanding the intermolecular and intramolecular forces present within the molecule. The following dissertation provides information on how one of gossypol's naturally occurring derivatives, 6,6'-dimethoxy gossypol (MG), forms polymorphs and solvates (Fig. 1.2). Like gossypol, 6,6'-dimethoxy gossypol has an array of interesting biological and chemical properties that further elucidate the complex interactions between gossypol and its derivatives and the chemical and biological environment.

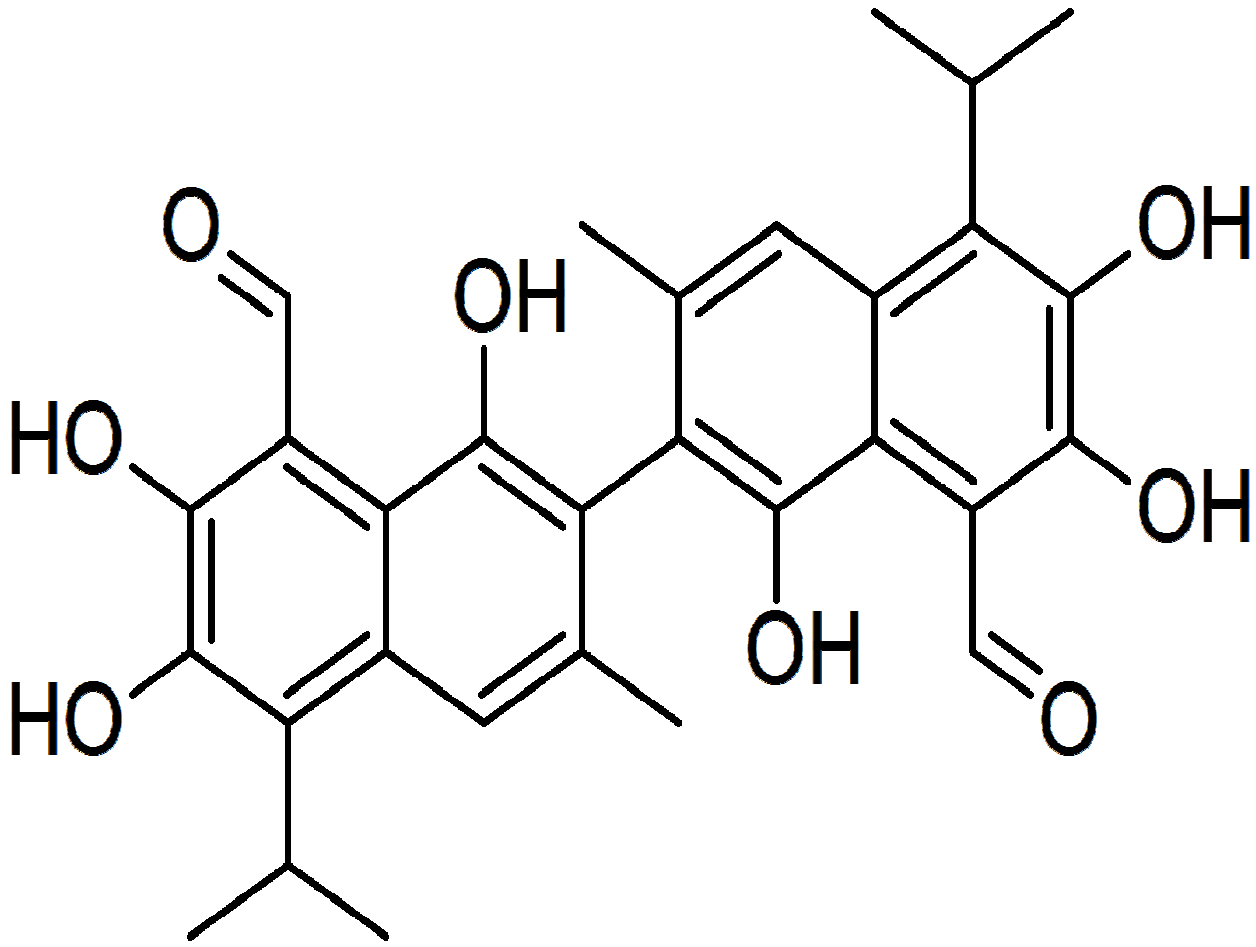

Figure 1.1 Gossypol [1,1',6,6',7,7'-hexahydroxy-5,5'-diisopropyl-3-3'-dimethyl-(2,2'-binaphthalene)-8,8'-dicarboxaldehyde] molecule. Specifically, the molecule consist of the two naphthalene rings has six alcohol groups, two aldehyde groups, an isopropyl group, and two methyl group.

Furthermore, seven amine gossypol structures are also presented which have similar chemical and crystallographic properties where di(aminopropyl) gossypol (Fig. 1.3) is analyzed in detail.

Gossypol was first discovered and isolated in the late ninetieth century by Marchlewski [9] and Longmore [10] as a natural occurring yellow pigment present in the intercellular pigment glands of leaves, stems, roots, and seeds of the cotton plant. The initial research conducted by Adams and coworkers [11-25] led to the structural elucidation of gossypol through series of diverse chemical reactions that included degradation, esterfication, etherfication, oxidation, and substitution reactions. In the pioneering work of Edwards and coworkers [26-29], a total synthesis of gossypol was realized.

One of the first proposed applications of gossypol was its use as a dye, but it proved unsuccessful because of gossypol's instability in the presence of light. Until the early 20^{th} century, cottonseed meal was used as a feed in livestock because of its high protein content. However, in high dosages, cottonseed meal proved to be toxic and by 1915 it was suggested that gossypol was the main contributor to the toxicity of the cottonseed meal [30-32]. In the following years, further evidence accumulated that the yellow pigment was toxic to monogastric animals which included rodents, poultry, and swine. It was later discovered that cottonseed meal containing gossypol required cooking to promote unbound gossypol to the bound gossypol state which is evidently less toxic. Agriculture research, at this point, focused on methods of decreasing gossypol content in cotton varieties, and methods of removing gossypol from cotton derived products such as meals and naturally occurring cotton seed oil. The overall consensus was that gossypol was a toxic by product of the cotton plant that had little to no use in agriculture and farming. Then, during the 1960's research was begun on combating tumor cells with alkaloids that, fortunately,

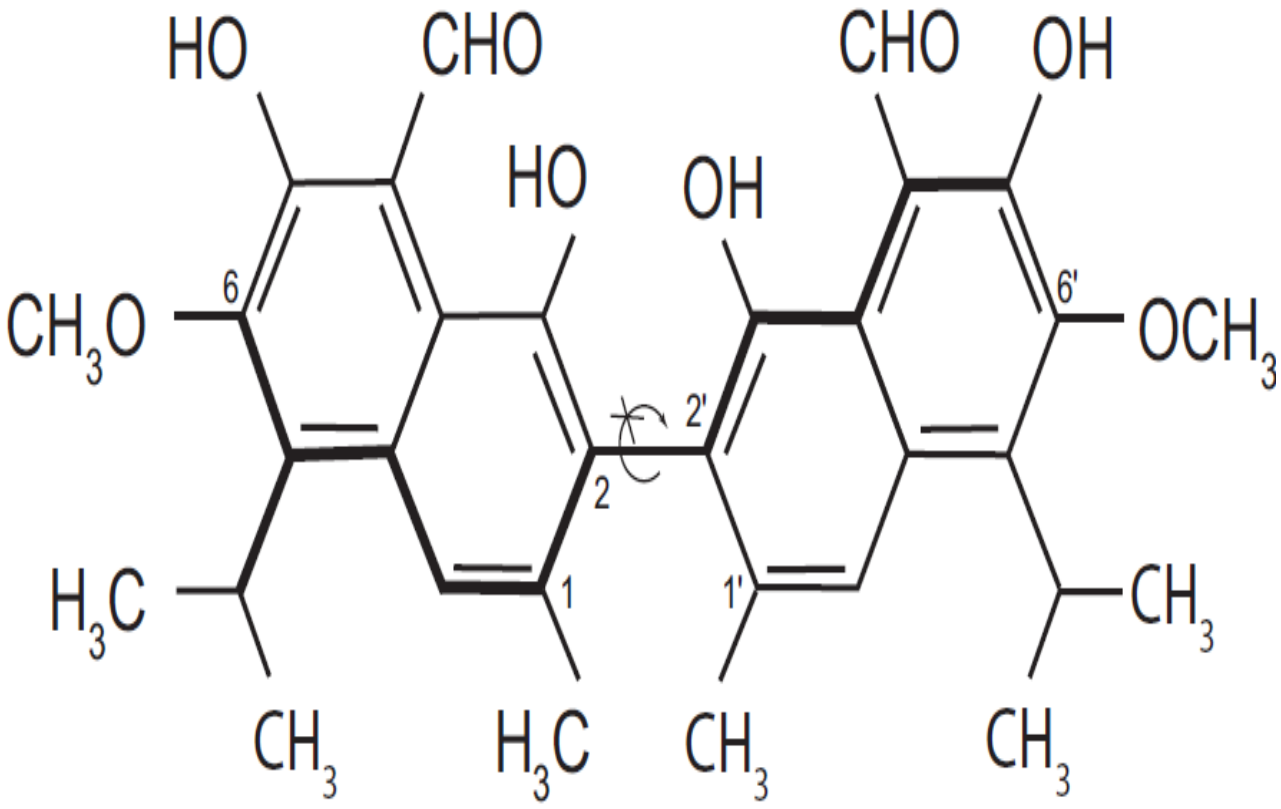

Figure 1.2 6,6'-Dimethoxygossypol (MG) structure. MG contains a crystallographic 2-fold axis between the 2 and 2' carbon atoms forming an internaphthyl bond. MG consist of two central naphthalene rings and several functional groups: 6 alcohol groups, 2 aldehyde groups, 2 isopropyl groups, and 2 methyl groups. Both the aldehyde and alcohol groups contribute to both inter and intramolecular bonding between adjacent MG molecules and solvates in crystallographic structures.

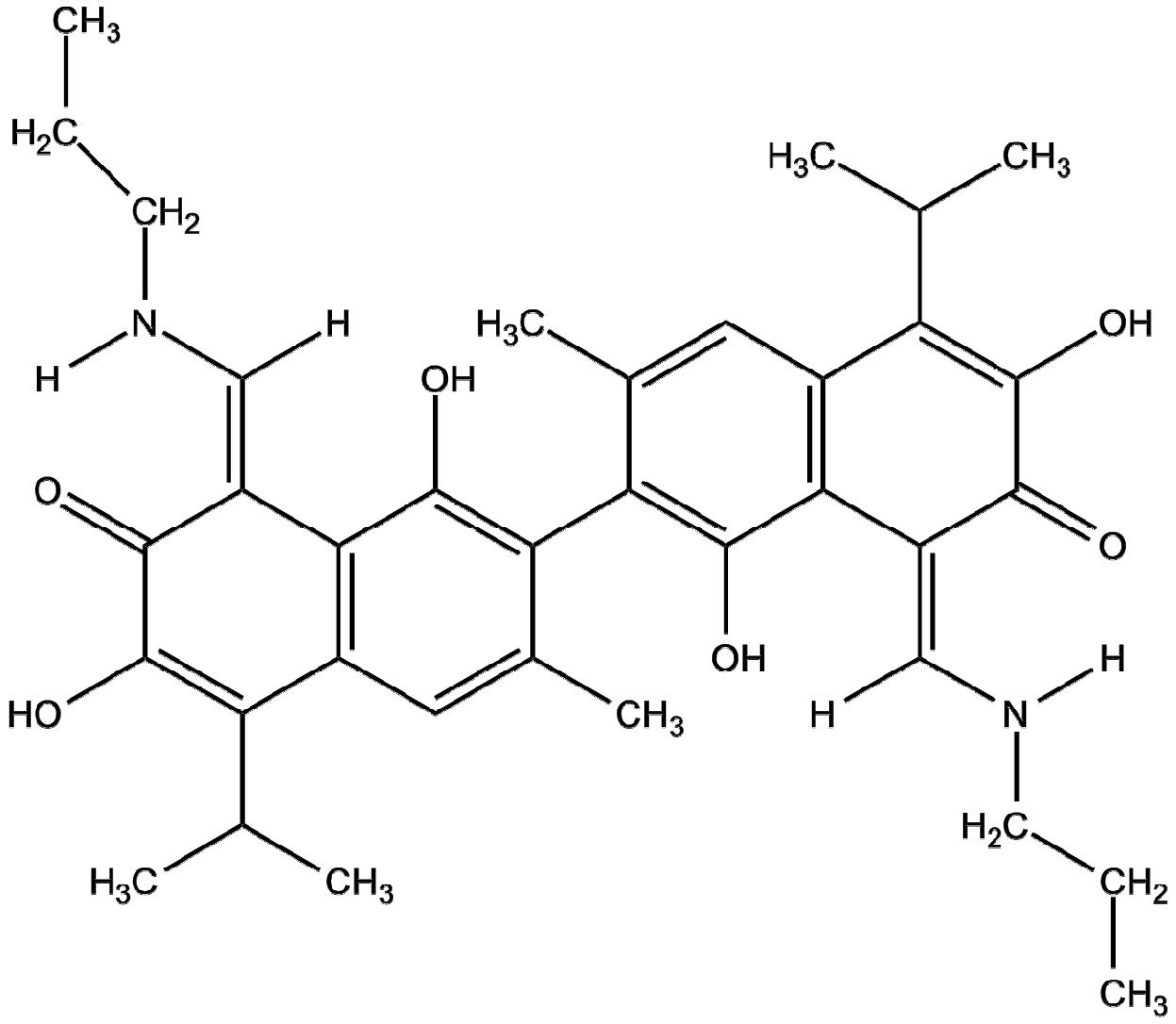

Figure 1.3 Di(propylamino)gossypol (PAG) contains two aminopropopyl groups substituted at the aldehyde positions in reference to gossypol. PAG still retains a number of functional groups: two alcohol groups, two amine group, two methyl groups, and two isopropyl groups.

included gossypol. It was this preliminary cancer research that helped catalyze a shift in the perception of gossypol from being a detrimental agent to a possible pharmaceutical drug [137].

In the 1970's, large scale testing was conducted with gossypol as a reversible oral contraceptive by Chinese scientists. It proved to be a highly successful contraceptive agent for 99.89% of male users where dosages consisted of 20 mg/daily for the first two months followed by 150-220 mg/month the next four months. While the initial studies provided supporting evidence for gossypol as a potential contraceptive in adult men, there were undesirable side effects that raised numerous concerns. The initial studies reported that 10% of patients acquired low potassium levels (hypokalemia) that were thought due to physiological changes in the sodium/potassium pump. Other symptoms included increased fatigue, decreased libido (6%), epigastric discomfort (2.0%), loss of appetite (2.4%), and nausea (1.0%). However, the most undesired effect was sustained or irreversible azoospermia in men (10%) after the initial study [33]. Azoospermia is a medical condition where there is no measurable amount of sperm in semen and is commonly confused with aspermia which is the absence of semen. A number of other researchers conducted similar experiments throughout the following years with conflicting data (34-37). A symposium was held in 1986 with leading gossypol researchers on the viability of gossypol as a potential contraceptive agent. It was concluded that because of the irreversible sterilization and the occurrence of hypokalemia, gossypol was not deemed a plausible antifertility drug. Since then, a number of other researchers have continued to study gossypol as a contraceptive agent and newer studies are beginning to shed light on the outcomes presented in the preliminary studies [38, 39]. A recent 10 year investigation, reported by Coutinhou, documents that blood potassium levels remained unchanged for the majority of gossypol users.

It was suggested that additional regional and economical factors that may have contributed to the ailments seen in the initial trials. The initial reports of hypokalemia may have been exaggerated, and mainly due to restrictions in the Chinese diet, which was already deficient in potassium and not a result of gossypol adversely effecting homeostatic renal physiology [40]. Specifically, samples of the testicular germinal epithelium showed no change after gossypol administration. Hormones, such as testosterone, were found at the same concentrations after the gossypol study and no permanent changes were seen in hormonal levels. Irreversible azoospermia was still present in a few subjects; however, recent studies have provided evidence that in many subjects, azoospermia was more likely due to subclinical varicocele. These recent findings have sparked renewed interest into gossypol's contraceptive abilities.

Gossypol also exhibits unique anticancer characteristics, and it is being investigated by a number of clinical researchers in combating a number of cancer types. Basic cell theory states that the homeostatic life cycle of tissue is regulated by the precise balance of both cellular proliferation and the death of cells. Defects that do not promote cell death lead to tumorgenesis if left unchecked, and in many cases chemoresistance. In general, gossypol and its derivatives affect the Bcl-2 (B-cell lymphocyte/leukemia-2) family of proteins that promotes the regulation of cellular apoptosis. It has been demonstrated that enantiomeric (-)-gossypol specifically inhibits Bcl-2, Bcl-xl, and Mcl-1 anti-apoptotic regulator proteins [41]. Bcl-2 inhibition or activation of cancer cells relies on the functionality of the mitochondria inner-membrane permeable transition pores which are responsible for calcium concentration, pH, voltage potential in the inner cristea, and the release of cytochrome c in the cytosol. The Bcl-2 gene has been presently linked to a number of cancers which include melanoma, breast, and prostate cancers, and this specific gene lineage has been associated with a number of autoimmune

diseases. Gossypol has been also tested at numerous cancer stages (stage 0 -stage IV) and cancer types. Currently, gossypol and gossypol derivatives are being tested as a potential pharmaceutical drug in the treatment of prostate cancer. Both androgen deprivation and chemotherapy have already proved unsuccessful methods in treating prostate cancer because of chemotherapeutic resistance. It has been known that prostate cancer is primarily due to over expression of antiapoptotic members of the Bcl-2 family of proteins which is believed to be the primary reason enantiomeric (-)-gossypol helps in regression of cancer growth. Specifically, Bcl-xL is over expressed in all refractory prostate cancers and further aids in metastasis, recurrence, and shortened survival. In other advanced human cancers, however, gossypol is unlikely to be clinically useful in the regression of cancer cells.

In other recent investigations, apogossypol, a derivative of gossypol where both aldehyde groups have been removed is being investigated in studies on cancer research [42]. Bcl-2 anti-apoptotic proteins, Bcl-2, Mcl-1, Bfl-1, Bcl-W, Bcl-Xl and Bcl-2 pro-apoptotic protein members, Bak, Bax, Bad, Bim, and Bid are able to form dimers that negate each other's functions in cell death or cell proliferation. Anti-apoptotic protein members contain a hydrophobic cavity, the BH3 domain, which binds to the pro-apoptotic proteins. Apogossypol mimics and binds to the BH3 domain of anti-apoptotic proteins which decreases anti-apoptotic behavior and promotes apoptosis. Apogossypolone, a derivative of apogossypol where the naphthalene ring is substituted for 1, 4-naphthoquinone, is currently being tested for follicular lymphoma (FL), the fifth leading cancer in the United States and the most common lymphoma worldwide [43]. Like apogossypol, apogossypolone acts as an antagonist against anti-apoptotic Bcl-2 protein members.

The gossypol molecule is composed of two naphthalene rings joined by an internapthyl bond at the 2- and 2'- carbon atoms such that the two rings are related by a 2-fold axis. It

contains a number of functional groups and aliphatic side chains (Fig. 1). Six hydroxyl groups exist within the substituted 2, 2' binaphthalene ring structure at positions 1, 1' and 6, 6' and 7, 7' positions. The hydroxyl groups existing at the 1- and 1'- positions are more reactive than the remaining hydroxyl groups. The aldehyde groups are located at the 8- and 8'- carbon positions, and because of aldehyde group's ability to lend pi electron character to the naphthalene rings give rise to the varied and rich chemistry that gossypol and many of its derivatives posses. Both the aldehyde and hydroxyl groups participate in extensive intramolecular hydrogen bonding networks within each naphthalene ring structure. There exists a strong intramolecular hydrogen bond between the aldehyde group at C-8 and the C-7 hydroxyl group that forms a pseudo third ring that is coplanar to each naphthalene structure. This particular hydrogen bond is the strongest of the all the hydrogen bonds, and has been estimated to be approximately 10.7 kcal/mol [44]. The locations of the hydroxyl and aldehyde groups form a lipophobic region within the gossypol molecule. Four alkyl groups exist on the other half of the gossypol structure, two methyl groups at the 3, 3'- positions and two isopropyl groups at 5, 5'- positions. The alkyl groups in some structural studies are generally oriented in the plane of both naphthalene rings, but both the 1, 1' hydroxyl groups and methyl substituents restrict rotation of the two naphthalene planes around the 2, 2'- internaphthyl bond.

The 8, 8'- aldehyde groups create the possibility of tautomerization in gossypol, and contributes to the complex chemistry inherent in the molecule. Gossypol may exist in three tautomeric states involving its aldehyde groups. These consist of an aldehyde tautomer, a ketone tautomer, and a lactol or hemiacetal tautomer. The environment and/or solvent that gossypol is immersed in will dictate which tautomeric state is thermodynamically favored. Chemical reactions of gossypol may thus produce a variety of products depending on which tautomers are

present. This can be illustrated with the following simple example. Suppose a specific chemical reaction, targeted for the aldehyde form reacts to form a single product. If the aldehyde form exists in a 50% equilibrium state with the ketone tautomer, then a number of other reaction products can ensue from the ketone form. Experimentally, this is what is observed with gossypol reactions.

The tautomeric aldehyde (-) - gossypol form has the highest biological activity, and it is believed that reactions with other tautomers, in vivo, produce by-products that contribute to the toxicity of gossypol [45]. Gossypol's complex reaction chemistry is further increased by its potential to form different tautomeric forms on each naphthalene ring simultaneously. As a consequence, it has been suggested that the aldehyde functional groups are the primary cause of toxicity for the gossypol molecule. Recent studies of apogossypol, a derivative of gossypol minus the aldehyde group, show that it seems to retain a majority of gossypol's therapeutic effects along with decreased toxicity [30].

Gossypol exists as a racemic mixture, naturally, in most cotton species. Both the (+)- and (-)- enantiomeric forms are stable at ambient temperature. The (+)- enantiomer has the S form designation and the (-)- enantiomer is labeled the R form. Crystallographic studies of a pure enantiomeric form have proven difficult because of the difficulty in growing pure R or S enantiomeric crystals suitable for x-ray structure analysis [16]. Certain varieties of cotton plants, however, favor production of either enantiomer, and ratios range from 97:3 to 31:69 for the (+)- and (-)- forms respectively. An abundance of research has suggested that (-)-gossypol is more biological active, but the (+)- gossypol form may serve as an advantage in specific cotton varieties. For example, in commercial cotton seed *Gossypium hirsutum,* the ratio between (+)- to (-)- enantiomers is 3:2. In other cotton species such as *Gossypium barbadense*, the (-)-

enantiomer predominates. Research conducted on the variety *Thespesia populnea* suggest that it produces enantiomerically pure (+)-gossypol [138]. Interestingly, the (+)- is less toxic to nonruminant animals, and feeds consisting of predominant (+)-gossypol are considered safe in general. More recently, research has focused on whether the (+)-enantiomer is toxic to insects [47] and certain studies suggest that there are benefits of the (+)-enantiomer as an active naturally occurring insecticide. Separation of racemic mixtures of gossypol have proven difficult, but reacting gossypol with amine groups to create Schiff bases and then using reverse phase high performance chromatography has proven a successful technique for separating the S and R forms.

Because gossypol has an extensive number of functional groups, mainly the alcohol and aldehyde groups, the combination of these reactive centers provide for an assortment of rich reaction chemistry. In addition, the conjugated dimeric naphthalene ring system further adds to the complexity of reaction products that gossypol and several of its derivatives exhibit in both chemical and biological environments. As previous stated, the conjugated bonds lend pi character to gossypol's functional groups, primarily the aldehyde groups and their various tautomeric states. In some cases, tautomerization restricts the types of reactions that are feasible with gossypol. This includes alkali-mediated methylation due to gossypol's instability with basic ionic salts, and limitations in esterfication of gossypol's hydroxyl groups because it creates a number of undesired by-products. Researchers, however, have made significant progress in developing novel methods of modifying gossypol's central naphthalene framework and functional groups by imposing strict reaction conditions, and by an assortment of regimented processes such as protecting alcohol groups and the implementation of multiple catalysts for desired products.

There exists extensive research published not only on gossypol's rich chemistry but also on its derivatives. In many cases, the chemical processes are well understood but in other cases they are not. Structural studies of derivatives produced by various reactions are vital in aiding the understanding of reaction mechanisms and pathways. Furthermore, chemical reactions and crystallographic analysis of modified forms of gossypol, like dimethoxy gossypol, facilitate an understanding of how specific functional groups affect the overall chemistry of gossypol.

Etherification reactions were vital in deducing the structure of gossypol in the early to mid twentieth century [48-52]. Adams and coworkers conducted some of the pioneering work dealing with modifying and understanding basic principles of gossypol chemistry. Their initial starting point consisted of the synthesis of hexamethyl gossypol ether that was subjected to reduction, oxidation, alkylation, esterfication, hydrolysis, and Schiff's base reactions that aided in elucidating gossypol's complex and dynamic structural arrangement. One of first methods used in etherification was methylation of the aldehyde groups and 7, 7' alcohol groups with dimethyl sulfate and methanol, forming gossypol tetramethyl ether, and with further changes in reaction conditions, methylation of the 6, 6' alcohol groups, forming gossypol hexamethyl ether. These reactions served as the basis for the synthesis of more elaborate ether products. Synthesis of other ether derivatives involved replacement of hydrogen atoms with methyl groups at alcohol group locations that lead to the creation of gossypol dialdehyde hexamethyl ether, creating a new hexamethyl ether form altogether. Seshadri and coworkers [50, 51] focused on selectively methylating particular hydroxyl groups. These modifications lead to the formation of gossypol containing four, six, or eight ether groups that were positioned symmetrically or asymmetrically across the naphthalene rings. Ether synthesis has not been limited to methylation, and has included silylation with various combinations of gossypol's hydroxyl groups. Selective

methylation of gossypol's 6, 6' hydroxyl groups with sodium tetraborate has yielded the ability to synthesize 6-methoxy gossypol and 6, 6'-dimethoxy gossypol, which are naturally occurring gossypol products in *Gossypium barbadense.* Biological research has also been conducted with ether based gossypol products. Specifically, gossypol tetramethyl and hexamethyl ethers were tested for decreased metabolic fructose degradation in human sperm cells [53]. While research shows that gossypol ethers are biological active, they are not as active as gossypol. In addition, various reviews in the literature support the proposal that for gossypol derivatives to be biological active, a number of free hydroxyl groups must exist on the molecule [54].

Reactions promoting ester group synthesis on gossypol has proven difficult because of the electron delocalization present in gossypol's ring system. A number of esters have been synthesized that include the hexaacetate, hexabenzoate, and hexapmitate esters [55-58]. Acetylated gossypol has also been successfully separated via preparative HPLC analysis. However, gossypol acetylate groups have proven to be very unstable and degrade in multiple pathways.

Oxidation of gossypol is a relatively well known reaction because it degrades so easily in nature and at ambient conditions. Since the first large scale processing of cottonseed oil, oxidation has been observed and created undesirable and degraded cottonseed oil components [59]. Gossypol's aromatic rings are very susceptible to absorbing electromagnetic radiation within the visible spectrum. This creates the potential for highly energetic electron states that aid in the production of free radicals. In general, many oxidation reactions require protecting groups, such as acetyl groups and dithiane derivatives, on all six alcohol groups of gossypol [60]. A number of alkaline solutions also elicit favorable oxidation reactions. Reacting gossypol with ferric chloride in an acetic acid/acetone solution with heat oxidizes gossypol to gossypolone [61,

62]. This oxidation converts gossypol's naphthalene rings to 1, 4-napthoquinone ring structures. Recent studies have also shown that gossypolone is optically active and has biological activity [63].

The chemistry resulting in the synthesis of apogossypol was first discovered by Carruth in the late 1910's while investigating gossypol extractions with fatty acids and reacting gossypol with hot alkali solutions [64, 65]. The apogossypol reaction involves the removal of both aldehyde groups, and as previous stated, eradicates gossypol's tautomeric properties. Apogossypol formation is also feasible with sodium hydroxide, potassium hydroxide, and other strong bases under nitrogen atmospheres for prolonged periods of times at moderately high temperatures [66]. Apogossypolone is produced by reacting apogossypol with aqueous ferric chloride in an acetone/acetic acid mixture with mild heat that removes two hydrogen atoms and replaces them with two ketone groups on both naphthalene rings creating a 1, 4-napthoquinone central backbone. Zhan and Jia [67] were able to convert apogossypol to apogossypolone using protecting groups of pyridine in acetic acid and subjecting the protected apogossypol structure to a Kiliani's solution, creating the quinone. Removal of the protecting groups on apogossypolone was achieved with a 20% sodium carbonate solution, dioxane, and a 4M hydrochloric solution at 80 degrees Celsius. Apogossypolone has shown significant biological activity, especially in cancer research. However, it's not known whether apogossypolone is more suitable for cancer studies than apogossypol. While apogossypol seems to be more unstable than apogossypolone at ambient temperatures, it's not well known whether this instability also exists in vitro.

Pharmacokinetical and metabolic analogs have been tested on gossypol, apogossypol, and apogossypol hexaacetate to better understand stability in vitro. A pharmaceutical study conducted by Lee and coworkers [68] provided evidence that gossypol, apogossypol, and

apogossypol hexaacetate are stable in vitro and clear from human plasma. Analogs were tested quantitavely and analyzed with liquid chromatography-mass spectrometry (LC/MS/MS). All three gossypol forms didn't exhibit any permanent conjugate binding to blood proteins but apogossypol binding to mono- and di-glucuronide conjugates were observed. Apogossypol was the most stable showing the lowest amount of metabolites but the slowest clearance rate. Interestingly, 20-40% of apogossypol hexaactetate was converted to apogossypol and the hexaacetate derivative formed various penta-acetate forms. Both gossypol and apogossypol had similar intravenous and oral pharmacokinetic rates and profiles. Apogossypol hexaacetate when administered orally converts to apogossypol and lacks any oral bioavailability [68].

Gossypol reactions involving ammonia and primary amines are some of the most researched and published studies [69-71]. Amination of gossypol usually involves a condensation reaction involving gossypol's aldehyde group. In general, the carbonyl bond on the aldehyde is replaced with a carbon-nitrogen double bond, where the nitrogen is bonded to a **R** group containing of a carbon backbone. The **R** groups themselves can consist of other functional groups such as alcohols, benzyl groups with complex aliphatic carbon chains, such as $-(CH_2)_{17}CH_3$ and aliphatic chains with their own functional groups. **R** groups that consist of aromatic groups have also been extensively studied and synthesized, ranging from phenolic to multi substituted alkene ring systems.

Reacting gossypol with amines ($R\text{-}NR_1R_2$ where R_1=H or C, R_2=H or C, and R=C) that react with its aldehyde groups, in general, forms Schiff's bases. Substitution of gossypol's aldehyde groups removes a degree of tautomerization and thus, decreases gossypol's toxicity while retaining its therapeutic effects. Gossypolone Schiff's bases, however, have been found to be more toxic than their gossypol counterparts [72-74]. Substitutions with primary amines that

form Schiff's bases are characterized by tautomerization that exists in the imine and enamine forms, and have been extensively studied by NMR, IR, and semiemperical molecular modeling [75-85]. Certain amine R groups, such as anilinogossypol ($R=C_6H_5$) register signals on NMR analysis indicating that the enamine structure is favored. Schiff's bases consisting of R groups belonging to hydrazines ($R=NHCH_2CH(OCH_2CH_3)_2$) favor a shift to the imine form. Thus, the identity of the R group and the chemical environment determines which tautomeric structure is chemically favored. It has been postulated that the degree of electronegativity that the R group imposes on the primary nitrogen of the Schiff's base determines the nucleophilicity of the nitrogen. The nitrogen group has a decreased electron environment creating an environment less likely to accept a proton required for tautomerization. Schiff's Base tautomeric equilibrium is also influenced by the presence of monovalent and bivalent metals, and involves complex electronic interactions from d-orbitals [86-89].

In many cases, synthesis of gossypol and gossypol Schiff's base derivatives require complete saturation of starting material in alcohols such as ethanol and methanol. An amine group is then added with other reagents to ensure amination, followed by heating. In recent studies, gossypol Schiff's bases have been synthesized with amino acids, specifically L-phenylalanine methyl ester, L-tyrosine methyl ester, and L-histidine methyl ester [90], adding to the family of gossypol amine substitutes. Other methods of synthesizing Schiff's bases include catalyzing agents such as N, N-dimethyformamidine [91], and the use of solid-state methods that have been successful in derivatizing only one aldehyde group [92].

Gossypol containing azo derivatives have been extensively studied and for good reason. Diaznonium ions or diazonium salts, RN_2X (X=an organic or inorganic anion) were first discovered by reacting sodium nitrite with phenolic compounds, specifically aniline, by Peter

Griess in the 1850's as an intermediate in the production of aryl sulfonyl compounds. Gossypol's substituted naphthalene ring structures serves as an ideal candidate for diazoniation and the choice of the R groups is extensive which includes aliphatic and aromatic groups [93-98]. In general, the reaction mechanism of diazonium compounds with gossypol involves both aldehyde groups, where electrophilic aromatic substitution occurs. The aldehyde group is kept intact and substitution occurs at the 6, 6'-, and 7, 7'- hydroxyl groups, and the 4, 4'- hydrogen atoms of the aromatic ring. These reactions are light sensitive due to u-v degradation of the salts themselves. The azo derivatives of gossypol, generally, aren't soluble in aqueous solutions unless $-SO_3$ and carboxylic acids are introduced into the azo groups, but are soluble in organic media. Azo gossypol compounds are well known as dyes in many cotton varieties where they serve as intermediates in aromatic chemistry [138]. Aryl azo derivatives of gossypol also display tautomerization between quinohydrazo and hydroxyazo forms and depending on the identity of the R group and chemical environment determines which form dominates. Aryl azo derivatives also appear to posses biological behavior by inducing interferon activity [30].

Hexamethyl apogossypol has been the central starting material for halogenation reactions involving gossypol compounds. Bromination of hexamethyl apogossypol has yielded a number of interesting derivatives, including the formation of brominated 5-membered ether rings in acidic conditions [99]. The reagents and the experimental conditions determine where bromines cleave on the starting material which include brominating the 3-, 3'- methyl groups, and direct cleavage of the phenyl rings at the 4-, 4'-, and 8-,8'- carbon positions. Halogenation has not been exclusive to just bromine and has included a limited number of products containing fluorine residues. Fluorination, in general, begins with the hexamethyl apogossypol already reacted with bromine. Potassium fluoride or silver fluoride is introduced with the appropriate experimental

conditions to yield a replacement reaction where bromine is exchanged for fluorine. Attempts to add fluorine directly to hexamethyl apogossypol have proved unsuccessful. So far, all fluorinated gossypol derivatives require use of brominated apogossypol derivatives.

Reacting gossypol with nitrile groups has been actively studied because of the removal of gossypol's aldehyde groups, which reduces tautomerization. Royer and coworkers have extensively researched the chemical processes in the synthesis of various nitrile groups [100]. Nitrile based reactions consist of reacting gossypol dioxime with acyl anhydrides, followed with heat and carboxylic acid sodium salt. Research into these compounds has concluded most biological active nitrile compounds are doubly substituted. Biological active nitrile derivatives consist of aldehyde groups that are substituted for simple nitrile groups but also the adjacent phenolic hydroxyl group, located at the 1-, 1'- carbon position, is substituted by acetyl groups [101]. Specifically, gossylic nitrile 1, 1'- diacetate exhibits antimalarial activity in *Plasmodium falciparum* by competitively inhibiting lactate dehydrogenase. Other nitrile derivatives, gossylic nitrile 1, 1'-dibutyrate substantially decrease the cellular metabolic pathway of malaria by binding to NADH.

Gossypol exhibits a wide range of reactions involving metals, ranging from light metals such as sodium and aluminum, to the lanthanides and even uranium [102-107]. Gossypol's ability to form an abundant number of metal complexes has generated interest in the areas of molecular biology, analytical chemistry, and genetic research [108-110]. For instance, gossypol complexed with copper (+2), mediates DNA cleavage by the reduction of copper to the plus (+1) state, and infers the possibility of using gossypol metal complex as catalytic precursors in future genetic studies [111-112]. Numerous theoretical studies, with density functional theory, have also been conducted on gossypol metal complexes, investigating how the presence of metals

affects the tautomeric equilibrium within gossypol. Like much of gossypol's rich chemistry, the ability for gossypol to form metal complexes is heavily dependent on the reactive hydroxyl groups present at the 1-, 1'- carbon positions and aldehyde groups.

Currently researchers are developing new reaction methods for the synthesis of new gossypol derivatives as future drug candidates for a variety of human ailments. The possibilities in modifying gossypol and its derivative's functional groups and ring system's have yet to be exhausted [113-119]. Amination, azo derivatives, and nitrogen based chemistry are the most abundant papers published on gossypol chemistry. Biological research with gossypol and its derivatives, in the last twenty years, has increased dramatically and yielded promising results. Research is also continuing on how to attain better yields of gossypol, gossypol enantiomers, and gossypol derivatives [120-122]. Recently, Dowd and coworkers have developed a method for separating gossypol and its methylated derivatives using an acetone extraction and separating the compounds in an acetonitrile/potassium phosphate buffer using reverse phase high performance chromatography. Apogossypol and apogossypolone are currently being used as therapeutic agents and are the most investigated form of gossypol tested for medicinal usage. A great deal of the literature, to date, reports low yields for both apogossypol and apogossypolone. Dowd and coworkers are currently developing methods for higher yields of both apogossypolone and apogossypol. Preliminary studies on increasing yields, by the Dowd research group, have already produced yields of apogossypolone as high 68%. In addition, research is being conducted on methylated derivatives of apogossypol and apogossypolone.

An extensive number of crystal structures for gossypol have been reported showing varied structural types [123-135, 140]. The gossypol molecule is very versatile in how it packs into the crystalline state due primarily to molecular flexibility both internally and externally with

itself and other molecules. Additionally, gossypol has the capacity to rearrange itself, in the crystalline state, to accommodate guest molecules. This has lead to an extensive list of gossypol crystal structures that are not only inclusion complexes but polymorphs as well.

Gossypol's ability to form a varied array of inclusion complexes, in general, is not difficult to understand since it contains all the basic components that promote inclusion formation: axial symmetry, a globular irregular composition, hydrophobic and hydrophilic regions, and a restricted number of conformational degrees of freedom between its ring system and functional groups. Examination of the gossypol molecule reveals a C_2 symmetry element at the center of the internaphthyl bond. Furthermore, rotation is restrictive at the aryl-aryl bond because of the methyl and hydroxy groups at 1, 1'- and 3, 3'- positions that give rise to severe steric hindrances.

Observations of intermolecular and intramolecular hydrogen bonding of gossypol in the crystalline solid state overlap with observations of chemical reactivity. The six alcohol and two aldehyde groups are primarily responsible for creating the majority of intermolecular interactions between adjacent gossypol and guest molecules within all gossypol crystal structures. The intramolecular hydrogen bonding between O3-H$^{\cdots}$ O-2 atoms and O7-H$^{\cdots}$ O6 atoms are quite strong, where the donor-acceptor distances between these bonds range from 242-250 pm. In comparison, the equivalent bond length in salicylaldehyde is approximately 261.2(5) pm [30]. The hydroxyl protons at the O3-H and O7-H positions are thus very inaccessible to intermolecular hydrogen bonding within crystals. The alcohol groups, O8-H and O4-H contribute to both intermolecular and intramolecular hydrogen bonding depending on the environment. In certain crystal structures, the O8-H atom forms hydrogen bonds with the O7 atom and the O4-H atom forms hydrogen bonds with the O3 atom. In other structures, the O8-H

and O4-H atoms hydrogen bond to neighboring gossypol molecules and or guest molecules, forming an extensive hydrogen-bonding network. This particular ability for the O8-H and O4-H hydroxyl groups to impart either intermolecular or intramolecular hydrogen bonding is probably the primary reason why, when both alcohol groups are substituted for methoxy groups, MG is still able to form a variety of crystal structures.

In all these cases it is the electronic structure that is of central importance in understanding chemical behavior, molecular geometry, and global structure. When considering gossypol and many gossypol derivatives, it is the electronic properties and its interactions that primarily govern the rich chemical, biological, crystallographic, and thermodynamical properties. Consequently, the study of the majority of chemistry, at all levels, essentially is the systematic study of electron(s) interactions at the atomic and molecular levels. With gossypol and gossypol derivatives in as medicinal agents, the overall molecular geometry and electronic behavior dictates how it interacts within the protein cavity of the BH3 domain. Basic gossypol chemistry is vastly complicated and in many instances difficult to predict. For example, when gossypol and methylated gossypol derivatives are subjected to Schiff's base oxidation with Ferric Chloride and then subjected to further derivatization to form apogossypol, a completely different set of reaction products are formed than if the synthesis of apogossypol is run first followed by oxidation. Basic understandings of the structural and electronic effects which mediate such changes in chemical reactivity are not fully understood. Gossypol and its derivatives thus represent an interesting system for investigation because of its complex electronic structure, and using high-resolution x-ray diffraction techniques to determine the electron density distribution aides in understanding.

With all the extraordinary progress made with molecular theories, is there a unifying method that doesn't rely on a complicated series of mathematical intensive and computational burdensome algorithms that is able to describe electronic molecular structure in a simple and uniformed manner? Specifically, are there any theories that are able to define atoms within the context of molecules based on simple principles? Richard Bader through a series of developments, starting in the 1960s, proposed his Atoms In Molecules (AIM) theory that uniformly proposes a series of concepts for how atoms and their respective electrons should be viewed locally within the context of molecules [149-159]. The AIM model argues that, when evaluating the molecular electron density using topological considerations, it is possible to identify chemical features of individual atoms electrons from the total molecular electron landscape.

Bader's initial analysis of understanding molecular structure first deals with a crucial but elementary question of whether to perceive the notion of a molecule as a whole unit, versus a molecule being understood as an amalgamation of individual atoms that retain identifiable observables. When observing spectroscopic measurements on molecule(s) with Raman, microwave, infrared, NMR, ultraviolet, or fluorescence spectroscopy it is easy to adopt the notion that the spectrum created by such measurements is an unequivocal characteristic of a holistic and distinct molecule. Under further inspection, the individual properties of individual atoms becomes transparent when analyzing how the spectrum changes with the inclusion or exclusion of an additional atom(s). This distinction of focusing on individual atom types within molecules is also observed in transition state theory, and organic mechanisms dealing with electron donation and capture. Theories that apply a reductionist view of molecules as individual atoms are an exception as opposed to the norm. In developing AIM theory, a strict criteria

becomes self evident: the individual properties of atoms, on average, must sum to the total properties of molecules. A prime example for this criteria can be naturally understood that the total electron density of a molecule is just the sums of the atomic electron densities that form the molecule. This criteria can be extended to the total energy of a molecule being the total summation of the atomic energies defining the molecule. When examining thermodynamical properties where there is an incremental increase of hydrocarbons per methylene group, a standard heat of formation of -20.6 ± 1.3 kJ/mol is obtained. Even when geometric considerations are imposed on methylene groups within cyclopropane, the overall energy changes to ~ 38 kJ/mol can be accounted for in the strain energy present within the bonds due to charge transfer from the hydrogen to carbon atoms. It becomes apparent that even more abstract principles such as the strain energy can be accounted by the individual properties of atoms embedded within molecules. While there are well established quantum mechanical procedures that relate spectroscopic changes in energies due to a molecule having an additional atom(s) and there are rigorous theoretical methods that relate atomic properties to bulk matter, like heats of formation, there is no single framework of study that incorporates chemical properties solely based on the individual atoms that embody the molecule.

AIM is a quantum mechanical theory. Like many molecular quantum theories, the AIM approach is a theory centered on the electron density that can be derived from wavefunctions. As a result, two conditions must be inherent with the AIM theory: the state wavefunction must contain all the requisite information that is axiomatic in partitioning atoms within molecules and there has to exist observables that manifest into testable, empirical data. The AIM theory central edifice is the charge density, defined as $|\psi^2|$ from molecular wavefunctions. As stated in Atoms

In Molecules: A Quantum Theory [141], "while the theory has its origin in quantum mechanics, its vehicle of expression is the charge density"-Bader.

When discussing the morphological properties of a real or complex coordinate system defined by a series of equations, what is being described essentially is its topology. In recent years, the mathematics of topology has shifted from an abstraction in theoretical chemistry and physics to an invaluable tool in mainstream research. Topology is primarily concerned with the overall qualitative properties of the shapes of functions in R^N and not properties dealing with metrics in distances, tangent spaces, or changes of coordinates within vector fields. For a function to be considered a topological space it must be homeomorphic: a continuous function whose inverse is a continuous function as well. While homeomorphism may seem like an abstract principle to apply on wavefunctions, the property becomes immediately apparent when dealing with the total charge density. Essentially homeomorphic functions are smooth functions that contain continuous derivatives. The basic elementary postulates that define well behaved wave functions already meet the requirements for topological spaces. Namely, that wave functions must be continuous and the derivatives of the wavefunctions must be continuous as well. Since wavefunctions meet this criteria, topological analysis can naturally be extended to evaluate atomic and molecular electron probabilities, specifically $|\Psi^2|$. Although Bader's theory only promotes a few applications and ideas from topology, it will soon become evident on how powerful its application is to evaluating chemical systems.

There exist several dominant morphological properties of interest defined within the spatial properties of the charge density, $\rho(\mathbf{r})$. The charge density is a physical three dimensional scalar field that has values at each point in space. The topological properties that are of primary concern occur when the gradient operator ∇ is applied to $\rho(\mathbf{r})$ and the first derivatives of $\rho(\mathbf{r})$

vanish (or $\nabla \rho(\mathbf{r}) = 0$). These points are known as the critical points, $\mathbf{r}_c$, specifically where the first derivatives of $\rho(\mathbf{r})$ vanish. These indicate points of extrema associated with the charge density that are indicative of maxima, minima, or saddle points. Evaluating and examining the topology of the charge density becomes more evident when surveying the associated gradient field of the charge density: $\nabla\rho(\mathbf{r})$. When applying the gradient operator to the charge density, each point within $\rho(\mathbf{r})$ is assigned both a direction and a magnitude. Principally, the gradient operator conveys the charge density function as a vector field which aids both in a visual and geometric assessment of the electron density. Furthermore, the localization of the dense positive charge of the nuclei and its attraction to electrons exhibits a landscape with predominant topological features in atoms and molecules where a maxima of charge density exists at the nuclear position(s).

The critical points can be further defined mathematically when examining the Hessian matrix of the charge density. The Hessian is a square matrix $[\mathbf{A}]_{ij}$ (where $i = j$) that has elements of second-order partial derivatives applied to a function defined in a set of coordinates. The Hessian is intrinsically a second derivative test on a function to ascertain when the function is convex or concave. When defining the Hessian matrix $[\mathbf{A}]_{ij}$ of the density ρ as

$$\begin{bmatrix} \frac{\partial^2\rho}{\partial x^2} & \frac{\partial^2\rho}{\partial x\partial y} & \frac{\partial^2\rho}{\partial x\partial z} \\ \frac{\partial^2\rho}{\partial y\partial x} & \frac{\partial^2\rho}{\partial y^2} & \frac{\partial^2\rho}{\partial y\partial z} \\ \frac{\partial^2\rho}{\partial z\partial x} & \frac{\partial^2\rho}{\partial z\partial y} & \frac{\partial^2\rho}{\partial z^2} \end{bmatrix}$$

we automatically see that many of the off diagonal second partial derivatives are redundant. When evaluating the Hessian for the charge density at the critical points: $\nabla \rho(\mathbf{r}_c) = 0$, the

diagonalization of the matrix $[\mathbf{A}]_{ij}$ reduces all non diagonal terms to zero and the matrix can be defined as $[\mathbf{\Lambda}]_{ij}$ where

$$\mathbf{\Lambda} = \begin{bmatrix} \frac{\partial^2 \rho}{\partial x'^2} & \mathbf{0} & \mathbf{0} \\ \mathbf{0} & \frac{\partial^2 \rho}{\partial y'^2} & \mathbf{0} \\ \mathbf{0} & \mathbf{0} & \frac{\partial^2 \rho}{\partial z'^2} \end{bmatrix} = \begin{bmatrix} \boldsymbol{\lambda_1} & \mathbf{0} & \mathbf{0} \\ \mathbf{0} & \boldsymbol{\lambda_2} & \mathbf{0} \\ \mathbf{0} & \mathbf{0} & \boldsymbol{\lambda_3} \end{bmatrix}$$

with Eigenvalues $\boldsymbol{\lambda}_i$. The trace of the Eigenvalues associated with the Hessian at $\rho(\mathbf{r}_c)$, when diagonalized, are real and special consideration is given to whether the values are positive or negative. Since the gradient of the charge density is naturally defined as vectors, the rank ω is the number of non zero column vectors within the Hessian. The algebraic sum of the signs of the Eigenvalues can be defined as the signature and denoted as σ. When coupling the values for both the signature and the rank as (ω, σ) we have a new method for defining the critical points based on these two properties.

Since the charge distribution of any neutral atom or molecule encompasses a span of three dimensional space, the rank is always equal to three. A rank of ω = 3 then becomes a topological property of any energetically stable charge density. Any critical point where ω □ 3 corresponds to a case where at least one curvature is zero and is defined as degenerate and unstable. A critical point where one of the curvatures is zero exists in an unstable state, where any slight change in the charge density induces it to either vanish or to bifurcate into a non-degenerate critical point that is stable and the rank becomes ω = 3. It is easy to understand that signatures of rank less than three are very volatile because they physically correspond to a flat plane of charge density spanning only two dimensions. Critical points of ω □ 3 may exists, momentarily, when dealing with charge densities evolving with time. Upon further

investigation, the topological properties inherent with the charge density of atoms and molecules where ω = 3 result in only four possible signatures are possible at the critical points:

(3, −3) All curvatures are negative and the density ρ is a local maximum at $\mathbf{r}_c$.

(3, −1) Two curvatures are negative and the density ρ is a maximum at $\mathbf{r}_c$ in the plane of defined by their corresponding axes. The density is a minimum at $\mathbf{r}_c$ along the third axes which is perpendicular to this plane.

(3, +1) Two curvatures are positive and the density ρ is a minimum at $\mathbf{r}_c$ in the plane defined by their corresponding axes. The density is a maximum at $\mathbf{r}_c$ along the third axes which is perpendicular to this plane.

(3, +3) All curvatures are positive and the density ρ is a local minimum at $\mathbf{r}_c$.

When examining the simple functions illustrated by figure 1.4, the application of signature points can be easily illustrated. The top portion of the figure 1.4 illustrates two parabolic curves that are mirror images of each other with a symmetry element horizontal to the page. One parabolic curve on the right opens up and contains a (1, +1) critical point at the midpoint of the curve. The parabolic is itself a one dimensional line denoting the first 1 in its signature (ω = 1). The curve itself can be defined as a function of one variable in R^1. The position of the critical point is the midpoint of the curve, specifically in this illustration the bottom of the curve because it is at this infinitesimal point that the curve has no slope (or more precisely where $df(x)/dx = 0$). The second derivative shows (or by visual examination of the curvature of the line) that as you move away from the critical point, to the left and the right the function is increasing. Since the rank of the curve is 1 and increasing, the signature is plus one or (σ = +1). The other parabolic curve of signature (1, −1) has a rank of one and a critical point for the same reasons as explained for the

first parabolic curve. In contrast, the second derivative test on this point is negative and hence a signature of −1 (or $\sigma = -1$).

When surveying the dome shapes (figures 1.4) with (2, +2) and (2, −2) signature points a number of topological properties become apparent with their surfaces. The dome shaped figures can essentially be defined as planes existing in R^2 and intrinsically mapped within two coordinates axis. The rank for either shape is simply two or $\omega = 2$. When determining the critical points for either shape, again the first derivative test denotes where the slopes are nonexistent or zero. For the (2, −2) critical point illustration, it is at the apex of the doom. If we imagine a *x*-axis horizontally crossing half of the doom through the critical point, essentially a line slicing the doom into two separate equal halves. The *y*-axis, which bisects the *x*-axis at ninety degrees gives the ability to examine the curvature of both curves. From the critical point, as you move away from the r_c , the curvature of both the *x* and *y* axis decrease. The *x*-axis has negative slope and y-axis has negative slope, overall both negative slopes contributes two negative curvatures or $\sigma = -2$. The same applies to the (2, +2) critical points, but the critical point in this case is at the bottom of the inverted doom, a bowl, and any two bisecting axis crossing the critical point have curvatures that are increasing as you move away from the r_c (or $\sigma = +2$).

When examining the (2, 0) critical phase portrait, it is essentially a saddle. The phase portrait is a mapping in R^2 and can be defined by a function of two variables. Like the previous illustrations this leads to a rank of two or ($\omega = 2$). The critical point for this illustration however exists at the center of the saddle where, of course, the slope is equal to zero at this infinitesimal point on the surface. The r_c is at a position where it is at the bottom of a curvature where the slope is zero with respect to the gradient lines moving away from the curvature as illustrated. We can arbitrarily label these gradient lines aligning along the y-axis. Comparatively, the gradient

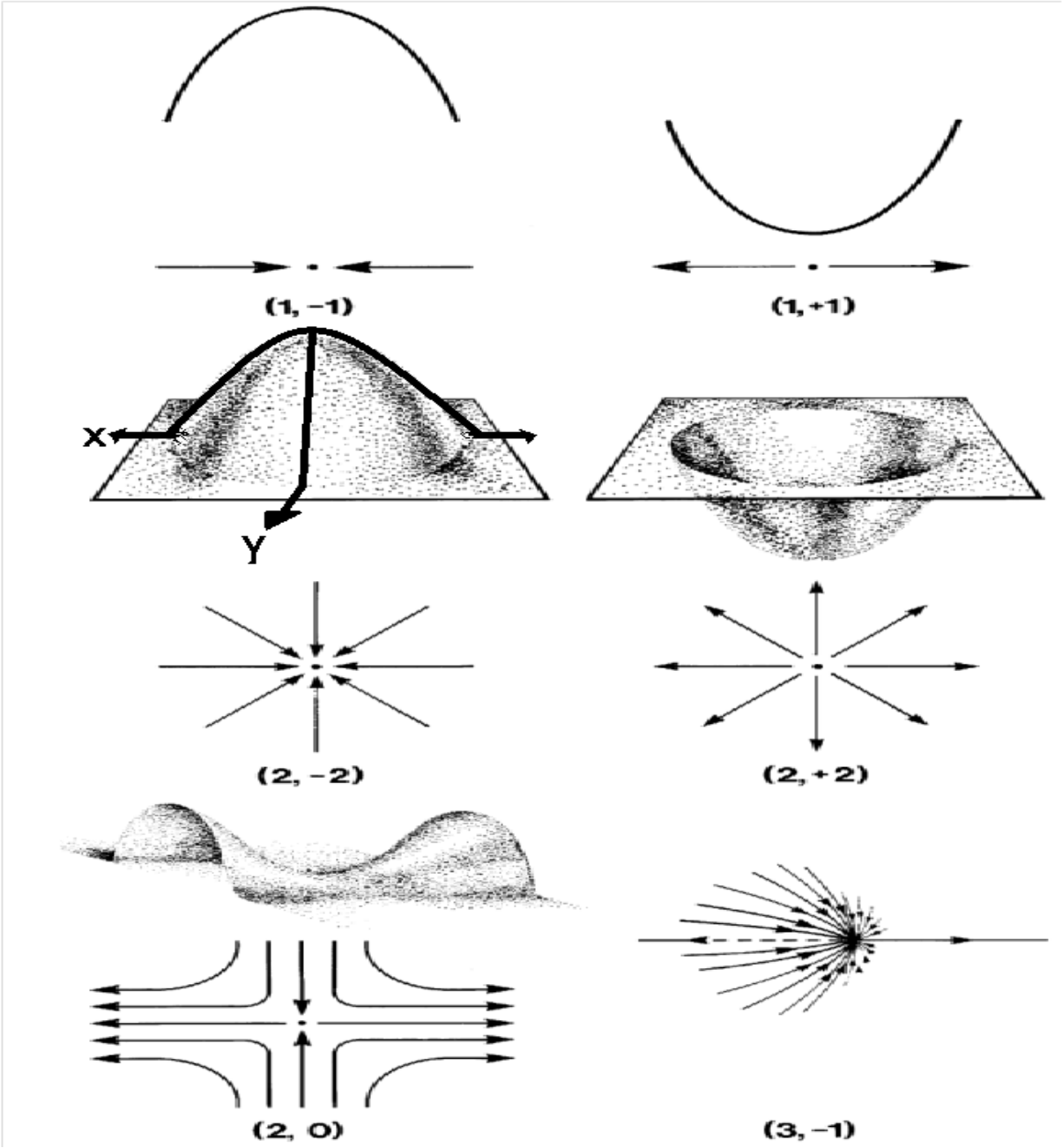

Figure 1.4 Top portion represents two parabolic curves that are one demensional with critical points at the apex of curve for (1, -1) c.p. and bottom of the curve for (1, +1) c.p. Both dome shaped figures consist of two dimensional planes (rank = 2) where the critical points exist at the top of the dome for the (2, -2) c.p. and and the bottom inverted dome for the (2, +2) c.p. The (2, 0) c.p. diagram is a two dimensional plane where the critical point exist at the critical corresponding to the line diagram. The (3, -1) c.p. line diagram represents a three dimensional line segments. Picture is taken from Bader's AIM: A Quantum Theory [141].

lines moving towards the critical point superimpose a secondary axis, in this case the x-axis, that represents the top of a curve. When identifying the signature of the critical point along the y-axis, the curvature is positive or ($\sigma_y = +1$). Identifying the curvature of the x-axis, however, is downward because the curvature is negative or ($\sigma_x = -1$). Since the rank of this critical point is two and we must add the total signatures of the curvatures denoted as $\sigma = \sigma_x + \sigma_y = -1 + 1 = 0$: thus a (2, 0) critical point is identified.

The phase portrait of the (3, −1) critical point, in brief, describes a point in R^3 where two principle axis of a surface are negative and the third principle axis of the surface is positive and as illustrated in figure 1.4 above is one of the four possible critical points in R^3. The (3, −1) critical points are referred to as 'bond critical points' and are associated with attractive interactions between atoms.

Expanding the application of critical points to the gradients of theoretical derived charge densities, we can readily identify the topological properties that are of interest in surveying the atomic properties within molecules and additional considerations of Bader's approach. The diborane molecule (B_2H_6) is an unusual molecule, in the sense, that it is an example of a molecule with hydrogen atoms that participates in a 3-center, 2-center bond. Surveying the two relief maps of the electron density of diborane for the critical points, where $\nabla \rho(\mathbf{r}_c) = 0$, one may visually inspect and characterize the types of critical points present. In both figures 5 and 6, the prominent boron atoms show the highest elevation. Figure 6 is the relief map that spans a plane through the terminal hydrogens and boron nuclei. The degree of elevation in the electron relief maps correspond to the total static concentration of electron density. The positions of each boron nuclei contain a maxima and have a (3, −3) signature since all three curvatures are negative at $\rho(\mathbf{r}_c)$. The signature at all nuclei are (3, −3) critical points including the two bridging and four

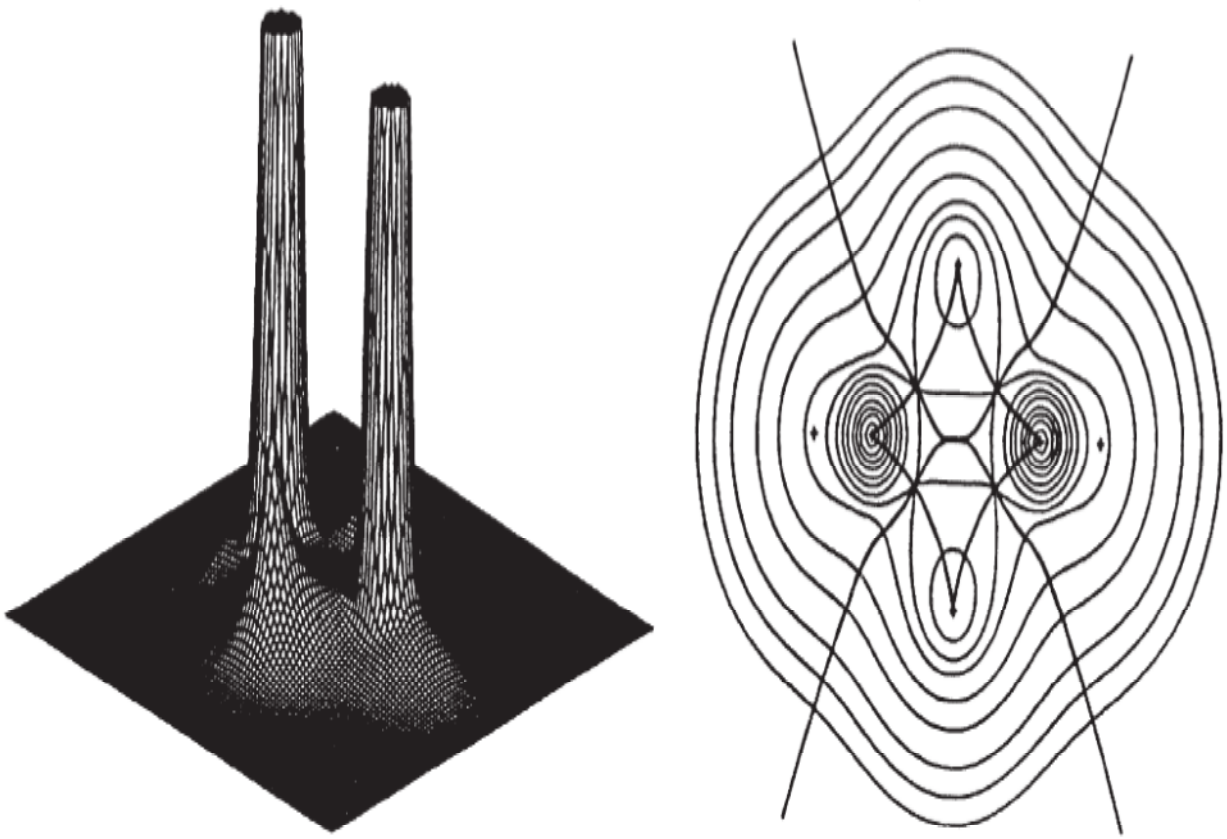

Figure 1.5 Electronic charge density plot of the diborane molecule through the plane of the bridging hydrogen atoms and corresponding contour plots. The degree of elevation corresponds to the degree of electron density where the two highest peaks represent the two boron atoms and the two smaller peaks with needle peaks are the bridging hydrogen peaks. Figure is taken from Bader's Atoms in Molecules: A Quantum Theory [141].

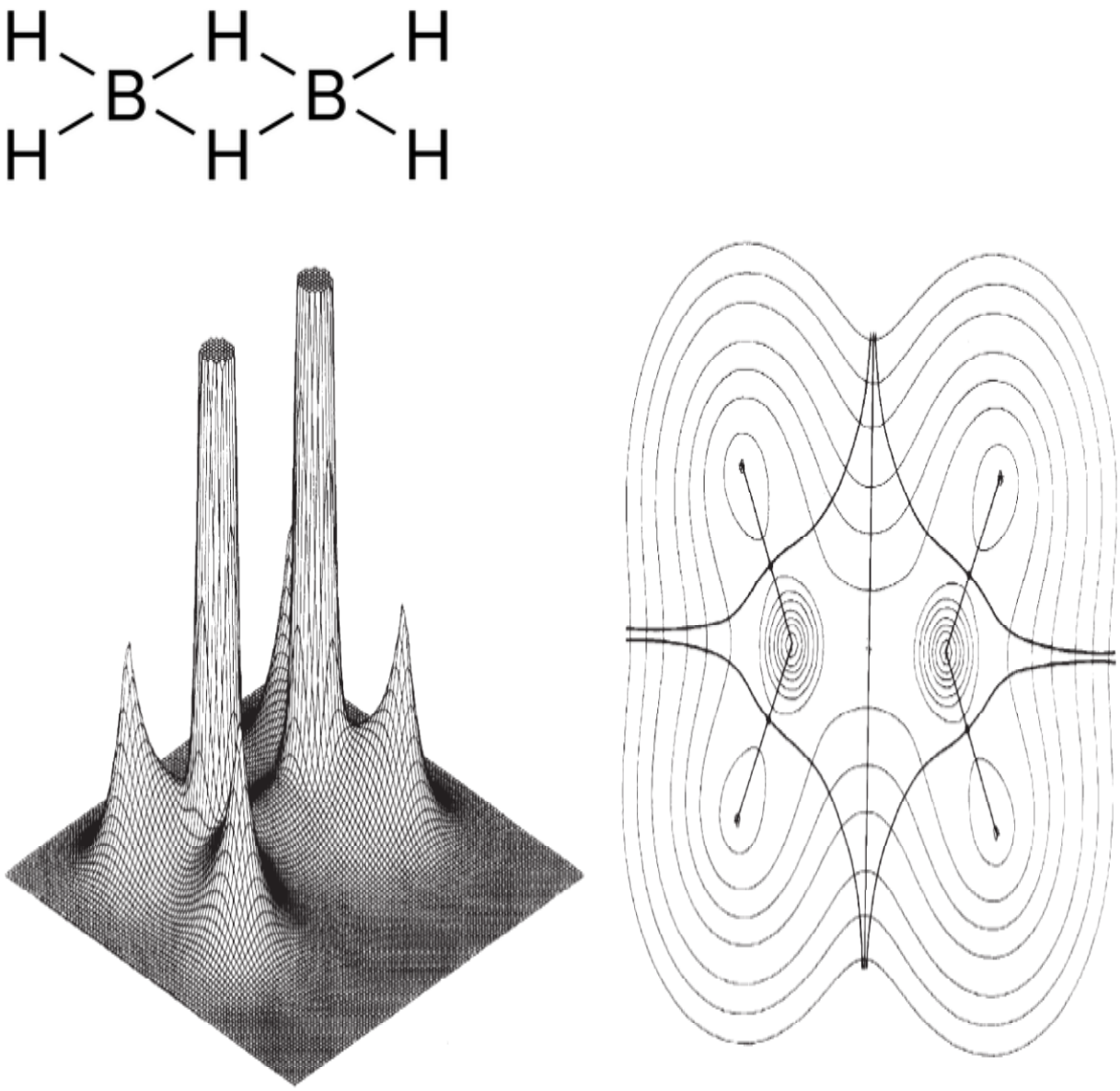

Figure 1.6 Display of the electronic charge density in three planes of the diborane molecule through the plane of boron atoms and the periphery hydrogen atoms. The degree of elevation correlates to the degree of electron density noting that the highest peaks are the two boron that have greater electron density than the hydrogen atoms. The picture on the right are the contour planes of the electron charge density. Diagrams are taken from Bader's Atoms in Molecule: A Quantum Theory [141].

terminal hydrogens. If a rotation axis is imposed between the inter nuclear bond length of the adjacent boron nuclei and the molecule rotated to a plane that spans both boron nuclei and the two bridging hydrogens as shown in figure 1.5, charge density peaks are clearly visible for the two bridging hydrogens containing (3, −3) signatures.

In figure 1.6, when examining the density that spans the terminal hydrogens, along the boron to hydrogen atom their exists saddle points along the bond paths. The curvature of the path along the ridge between the hydrogen and boron nuclei is positive and curvature perpendicular to the ridge is negative. In the context of solely the two dimensional relief map this constitutes a (2, 0) critical point. In figure 1.5, there exists a minimum between the two boron nuclei and both bridging hydrogens. Along the axis of both boron nuclei there is positive curvature. Along the axis of both bridging hydrogens there exists a positive curvature which corresponds to a (2, +2) critical point. To evaluate the third curvature on the two dimensional relief maps it's necessary to rotate the molecule or system of interest along one of the principles axis by 90° to assess the third axis (figure 1.6). The curvature of the third axis along the boron nuclei, if rotated by 90°, exhibits a negative curvature. Overall, the critical point existing at the midpoint between the boron nuclei, consequently, is a (3, +1) critical point. The critical points existing between the boron and terminal hydrogens, if examined between figures 5 and 6, leads to conclusion that these critical points have (3, −1) signature.

All four signature points of rank 3 have an identification that corresponds to conventional features of molecular structure. A (3, −1) signature has the property of classifying an internuclear axis between interacting pairs of nuclei, or from a chemical perspective it is representative of a bond. Critical points classified as (3, +1) exists in the central regions of bonded ring systems. A (3, +3) signature is representative of critical point existing within the

cavity of a cage system. A prime example can be seen within the center of the tertrahedrane molecule, C_4H_4 where there exists positive curvature emanating from all 3 coordinates from the critical point. As already mentioned, a (3, −3) signature is indicative of a nuclei and is always present at nuclear positions. It is often termed a *nuclear attractor*.

When applying the gradient operator to the charge density, a representation can be displayed based on the vector trajectories. The trajectories or gradient paths of the electron density may be understood by starting at some arbitrary initial point $\mathbf{r}_0$ defined by $\nabla\rho(\mathbf{r}_0)$ and then moving a small incremental distance $\Delta\mathbf{r}$, in the direction dictated by $\nabla\rho(\mathbf{r}_0)$ to a new position $\mathbf{r}_1$ and repeating the process continuously until the path terminates. Comprehensively this process projects gradient trajectory lines into a contour diagram of the charge density with the following properties:

1. The trajectories mapped by $\nabla\rho$ are perpendicular to planes of constant electron density.
2. For every point $\mathbf{r}$, the vector given by $\nabla\rho(\mathbf{r})$ is tangent to the gradient line at point $\mathbf{r}$.
3. For every critical point in ρ, a gradient trajectory originates and terminates where $\nabla\ \rho(\mathbf{r}_c)= 0$.
4. The gradient of the charge density projects a single path for $\mathbf{r}$, defining a trajectory that doesn't cross.

When surveying the contour maps of the diborane molecule, the gradient paths terminate at the (3, −3) nuclear critical points and follow paths that originate at either the bond critical points (3, −1) or the ring critical points (3, +3), or (for isolated molecules) at infinity. An assessment of the gradient vector fields of the charge distribution shows that all paths local to a (3, −3) critical point terminate at this point attractor, and further illustrates and reinforces why (3, −3) are referred to as nuclear attractors. Nuclei positions in the theory of AIM impose a strict topological criteria that any signature of $\sigma = -3$ in R^3 is of a nucleus. Any survey of a molecular

charge distribution based on this topological identification allows for the partitioning of individual atoms and its local charge within this context.

Along with nuclear attractors, the concept of what constitutes an atomic basin aids in defining the boundaries of an atom within molecules in relation to the charge density that is itself measurable property in real space. A (3, −1) bond critical point is both a gradient vector terminus and a point on a boundary that divides and defines the electron density associated with two neighboring atoms. The set of all trajectories terminating at a bond critical point form an inter-atomic surface that provides an unambiguous topological definition of atoms within a molecular scaffold. A vector **n** normal to the surface of the gradient density at r, **n**(r) is simply a tangential operator of the electron density. There arise conditions where **n**(r) doesn't change at infinitesimal points along any gradient paths that arise between two maxima or where **n**(r) = 0. If conditions exists where

$$\nabla\rho(\mathbf{r}) \bullet \mathbf{n}(r) = 0$$

this imposes a criteria for a set of coordinates where the vector normal to the surface of the gradient electron density will vanish. Comprehensively this operation outlines the boundaries of the atomic basin and is called the zero-flux surface. A crucial and natural property of the zero-flux surface is that no trajectories originating from a nuclei cross over it. This adds another postulate of what designates, topologically, atoms within molecules. When examining the relief maps for the diborane molecule, the (3, −3) critical points depict the boron and hydrogen nuclei and the (3, −1) signatures are the bonds between respective nuclei. The darkest lines surrounding the boron nuclei represent the zero-flux surface and are the boundaries of the boron nuclei where no trajectories cross from one basin to another.

With the application of the atomic basin and how it is defined by the zero-flux surface, along with the signatures of critical points that formalize chemical bonds, rings structures, and cages, an elementary but complete definition of how to characterize atoms within molecules has been established. Thus the major feature of the electronic structure of a molecule becomes its overall shape and properties which correlate to the electron density. The central theme in examining the electron density through the prism of the AIM theory is the overall topology of the system. One of the best features of AIM theory is how it establishes a consistent and systematic method of defining atoms within molecules with relative ease when compared to other quantum theories.

At the forefront of Bader's AIM theory is the systemization of partitioning atoms within complex molecular arrangements. On the other hand, the majority of molecular quantum theories rely on arbitrary or elaborate schemes to partition valance electrons. Concisely, a guiding principle in partitioning a continuous charge distribution should be based on a form of locality respective to atoms, formulated by Kurki-Suonio [136, 142-143], where charge is conserved. One of the main factors in evaluating the molecular electron distribution, of course, should be that the total number of electrons of the molecules should be equal to the total of the electrons of the individual atoms comprising the molecule or $E_t = \sum_i q_i$ where E_t is the total electrons within a molecule and q_i are the number of electrons for each individual atom within the molecule. In brief, the Kurki-Suonio formulation states that the *density at a point should be assigned to a center in the proximity of that point*. The valance or boundaries of the charge densities can be partitioned as either a *discrete boundary*, where the valance electrons of the density at each point are assigned to a specific atom, or a fuzzy boundry. In *fuzzy boundary*

partitioning, valance electrons comprising the density are allocated interpenetrating functions centered at each atom.

Many of the density functions employed in the analysis of molecular structure in theoretical chemistry and x-ray crystallography rely on fuzzy boundary conditions. The density functions of bordering atoms are continuous and overlap so overlaying regions interpenetrate, creating domains that are not intrinsically defined to one atom. Analysis of overlaying atomic regions is inherant to Mulliken and Lowdin population analysis, that constitute the most common methods used in evaluating partial charges based on LCAO molecular orbital theory.

A paramount contribution to the analysis of the charge density was introduced by Hirshfeld with stockholder partitioning analysis. The central premise of stockholder partitioning is defining a continuous sampling function $w_i(\mathbf{r})$ that allocates density to accompanying atoms within the system being evaluated. Likewise the sampling functions are founded on the spherical atom promolecule density which entail the summed average spherically ground-state atoms. The weight for any atom-*i* is evaluated as

$$\rho_{atom,i} = w_i(\boldsymbol{r})\rho_{total}(\boldsymbol{r})$$

where the density is defined as $\rho_{atom,i} = w_i(\boldsymbol{r})\Delta\rho(\boldsymbol{r}) + \rho_{spherical,i}(\boldsymbol{r})$. Both equations relatively delegate a partial fraction of the total charge density at any particular point that correlates to the "investment" in the total promolecule density at a point. Essentially the stockholder scheme allocates charge density to each atom's augmented fraction based on the unperturbed promolecule density that tends to result in charges and higher moments that are generally smaller than other partitioning methods.

Fragmentation solely defined by discrete boundaries has a number of merits in its evaluation of the molecular electron density, and conforms to the requirements of locality. A

number of studies by Kurki-Suonio examined spherical discrete boundaries of ions. Specifically, the chlorine ion was evaluated with an affixed spherical function within NH_4Cl molecules using electron densities obtained from powder diffraction data. A radius of best separation is characterized by the minimum radius of the chlorine ion. When examining the sphere of the eighteen electrons for the chlorine ion it was assessed the idealized sphere didn't account for the total charge, indicating an incomplete charge transfer from the cation to the anion. Kurki-Suonio and coworkers extended their research to an array of metal oxides and alkali halides which included MnO and NiO where charge transfer density was found to be reasonable. Using this approach, it was observed that charge neutrality was not maintained. A major contributing factor was the inability to assign space between spherical voids and in many instances where ionic spheres were present, overlapping occurred, accounting for error significantly. As mentioned, AIM theory has a more direct method of defining atomic properties within molecules that is not as susceptible to fuzzy boundaries or more computational intensive discrete boundaries.

Originally, Bader's AIM theory is centered around the charge density which in theoretical chemistry is itself the composite of a series of wavefunctions whether atomic or molecular in scope. The initial architecture envisioned for AIM was of electron densities constructed theoretically. Bader's theory was primitively constructed in the 70's and 80's when computational power, efficacy, and prowess were not major tenants, or a mainstream scientific venture in devising intricate complex wavefunctions to describe experiment. It was much easier to conduct experiments. Molecular quantum mechanics, in general, was a theory, in many instances, waiting for technology to mature so it could be appropriated to mainstream avenues of research. Even with today's present technology there is still a plethora of deficiencies in the theoretical frame work of molecular quantum mechanics that deal with calculations of how to

evaluate electron distribution within systems. The multitude of atomic and molecular theories that are currently researched is a testament of how these deficiencies can be greatly improved to agree with empirical measurements. Nevertheless, crystallographers and solid state physicist were one of the first to recognize a more efficient avenue of implementing AIM theory was not from a purely theoretical fabrication but one based on the empirical data ascertained from physical experiments.

Crystallography is by its very nature a rigorous study of the electron density itself and has proven as one the most accurate, authoritative, and veritable avenues in determining charge distributions. Since its inception, crystallographic x-ray analysis has naturally advanced in theory and application, and has taken center stage as the most concrete practice of molecular identification; geometric evaluation; and spatial orientation of atoms. High resolution x-ray crystallography development and research, in recent years, has had the capability to resolve structural properties with an accuracy of 0.001 Å using ($\lambda = 0.7107$ Å) an x-ray Molybdenum source. From the first NaCl crystals solved by x-ray diffraction, an assumption has been implicit that the atomic electron density is represented by the spherically averaged density of the isolated atom(s) in question. This spherical presumption, notably termed the *independent-atom model* (IAM), has had enormous success in solving simple repetitive inorganic structures such as minerals and/or lattices of heavier atoms where the valance shell is a minor contribution to the total charge density and is widely used for light atom structures where the valence shell is not minor contribution.

Naturally, use of the IAM warrants caution in cases where the valance shell is a major contributing factor to the total electron density, especially in cases of organic structures that are mainly comprised of atoms that contain electrons in second and third row *p*-orbitals. Positional

and thermal parameters of C, O, N, and H atoms may be susceptible to errors associated with the use of the IAM. In the context of x-ray structure analysis, the x-rays predominantly scatter from the electron density. The greatest abundance of electron density is found generally within a spherical region of an atom and, as long as the core electrons contribute more to the total density than the valance electrons, this assumption holds to a degree. When hydrogen forms a covalent bond with C, O, or N, the sigma bond accounts for most of the hydrogen atom's electron density which is displaced inwards into the bond. When assessing the atomic position of the hydrogen nuclei via a least-squares refinement based on a spherical IAM hydrogen scattering factor, the atom position will be biased towards the centroid of the density along the bond. This incorrectly positions the hydrogen atoms leading to shortened hydrogen bond lengths. Neutron diffraction data on sucrose molecules has shown errors in bond lengths derived from x-ray data of 0.13 (1) Å in C–H and 0.18 (3) Å in O–H bond lengths.

Another factor that the IAM assumes is that atoms in a crystal lattice are neutral. Atoms embedded in crystals naturally posses variable electronegativities which may lead to ions, molecular dipole moments, and higher electrostatic moments, which can influence the X-ray crystallographic data. The dipoles existent within molecules are due to two large contributing factors: the nonspherical electronic alignment of the atomic densities and, to a greater degree, the charge transfer stemming from the electronegativities of the atoms within the structure. Theoretical calculations based on population analysis of extended basis-set self consistent field wave functions of the HF molecule give hydrogen a net charge q of +0.4 electron units (e) and for CH_4 the hydrogens respectively have a value of +0.12 e [136].

Deviations from the IAM of this magnitude are easily observable with accurate x-ray diffraction data. Molecular dipoles may often be accounted for simply by the preferential

population of nonspherical features of the valance electrons. For instance, oxygen atoms in many cases have double-filled nonbonding lone-pair orbitals that are evident in C−O−C and H−O−H and R_1−(C=O)R_2 (where R_1 is any alkyl group and R_2 is a H or secondary alkyl group). It has been shown with neutron scattering studies of oxalic acid, that using the IAM for x-ray refinement the oxygen atoms tend to be systematically displaced by 0.008 (2) Å in the direction reflecting the greatest lone pair density.

Aspherical shifts are evident in other atoms, including the nitrogen atoms in tetracyanoethylene, which show a shift of 0.008 (1) in the −CN group (ref). Other examples of large asphericity shifts include tetracyanoethylene oxide along the oxygen atom with a magnitude of error of 0.013(4) Å. In sulfamic acid, H_3NSO_3 a double shift results in errors of 0.0022 (6) Å and 0.0015 (4) Å in the positions of the two sp^2 oxygen orbitals bonded to sulfur. Not only does the use of spherical scattering factors in X-ray analysis lead to incorrect bond lengths but also incorrect bond angles, and thus to errors in molecular geometry.

A procedure that crystallographers have employed to avoid asphericity shifts is the use of high-angle data in combination with a high-order refinement. X-rays scattering from valance electrons occurs largely at low scattering angles. Scattering of X-rays at high-angles (or high-order) is largely due to the core electrons within atoms. By collecting and refining high-order data, atomic positional and thermal parameters are obtained that are free of bias due to valance electron scattering.

Alternatively, determination of structural parameters with an aspherical model, as opposed to the IAM, yields accurate structural parameters and in addition the spatial arrangements of the valence electron distribution. The aspherical model implemented in the calculations of atomic form factors has advanced greatly in the past 30 years in parallel with the

advancement of diffractometers and efficiency in computing ability. Philip Coppens and collaborators [149-204] have greatly contributed to the aspherical formalism, which has been extended and adopted by the International Union Of Crystallography (IUCr) to become a more mainstream tool in molecular evaluation. The aspherical model will be discussed shortly, however, a brief analysis of basic x-ray physics and theory must first be discussed to elucidate the benefits of the aspherical model in dealing with the research presented.

One of the most central calculations in x-ray crystallography is the determination of the electron density ρ(r) within a crystal lattice. The mathematical expression for ρ(r) can be given in a number of ways depending on how the crystal lattice is defined. The electron density can be represented by the classical Fourier series expression:

$$\rho_{crystal}(\mathbf{r}) = \sum_{H} F_H e^{-2\pi i \boldsymbol{H}\cdot\boldsymbol{r}} \times V^{-1}$$

where $\rho(\mathbf{r})$ is the periodic electron density, F_H is the structure factor, 1/V represents the volume of the unit cell, **H** is the scattering vector, **r** is the position vector defined in terms of the (x, y, z) fractional coordinates, and the term $e^{-2\pi i \mathbf{H}\bullet\mathbf{r}}$ includes the sine and cosine terms of the Fourier series. The Fourier series coefficients, F_H, can be obtained by experiment.

The x-ray structure factors can also be calculated by expressing the unit cell density distribution as a the summation of the individual atomic densities where each atomic density is centered at the nuclear position $\mathbf{r}_j$

$$\rho_{unit\ cell}(\mathbf{r}) = \sum \rho_j(\mathbf{r})^* \, \delta(\mathbf{r} - \mathbf{r}_j)$$

which defines the unit cell density as the summation of the convolution of each respective atom *j* and the delta step function centered at the nuclear position. Applying the Fourier transform to leads to the following equation

$$F(\mathbf{H}) = \hat{F}[\rho_{unit\ cell}(\mathbf{r})] = \sum f_j\ (\mathbf{H}) e^{2\pi i \mathbf{H}\cdot\mathbf{r}_j}$$

where the structure factors, $F(\mathbf{H})$, are defined as the sums of the individual atomic scattering factors $f_j(\mathbf{H})$ which are the Fourier transforms of the atomic density of atom-*j*. In determining the crystal structure, it is the atomic densities that are averaged to be spherical symmetric, and can also be defined in arbitrary spherical polar coordinates of (r, θ, □) where $\rho_j(r)$ is the radial dependence of the theoretical ground state of atom-*j* [136].

The Fourier transform of the radial density function $\rho_j(\mathbf{r})$ then can be expressed as

$$f_j(S) = \int_{atom} \rho_j e^{2\pi i \mathbf{S}\cdot\mathbf{r}} d\mathbf{r} = \int_{\upsilon=0}^{\pi} \int_{\phi=0}^{2\pi} \int_{r=0}^{\infty} \rho_j(r) e^{2\pi i S r cos\upsilon} r^2 sin\,\upsilon dr d\theta d\phi$$

evaluating the integral with respect to θ and □ variables leads to the following integral in terms of r

$$f_j(S) = \int_0^{\infty} 4\pi r^2\, \rho_j(r) \frac{sin2\pi Sr}{2\pi Sr} dr \equiv \int_0^{\infty} 4\pi\, r^2 \rho_j(\mathrm{r}) j_o dr \equiv \langle\, j_o \rangle$$

j_o is the zero-order spherical Bessel function and $4\pi r^2\rho_j(r)$ is the probability that the electron is found with a radius defined on the intervals from r to $r + dr$. The preceding equation is known as the Fourier-Bessel transform of the atomic density [136].

One interesting characteristic of atomic form factors is the inverse relationship between the normalized value of the form factor and the radial distribution of the atom. The inverse relationship is not just a mathematical artifact but is observed routinely in x-ray diffraction experiments. When examining the scattering factors in isoelectronic ions of Na^+ and F^-, the inverse relationship becomes evident. The sodium ion with its slightly smaller radius (116 pm) has a expanded form factor when compared to the larger radius of fluorine (119 pm) which has a contracted form.

While the spherical form factors as included in the IAM have been widely used for routine structural analysis, a better description of the valance electrons is warranted for a more accurate and precise determination of atomic and molecular structures, and electron distributions. In the research presented here, both the low angle and high angle data are fit with a model that includes parameters which describes the aspherical features of the atomic density, termed the aspherical multipole refinement model.

The aspherical model is systematically structured around the κ-formalism that allows for charge transfer associated with expansion or contraction of atoms. The κ-formalism seperates the scattering due to valance electrons from that of the filled inner or core shells. The division of scattering allows for the modification of the valance shell radial dependence and total valance population. In constructing the κ-formalism, two charge density parameters must be introduced: the valance shell population parameter P_v and a parameter that allows for the expansion and contraction of the valance shell, κ. Concurrent introduction of κ and P_v is necessary because a change in the electron count affects the electron-electron repulsions which leads to modulation of the radial dependence on the electron distribution.

The κ-formalism for the atomic density can be succinctly described with the following equation

$$\rho_{atom} = \rho_{core} + \rho'_{valence}(\kappa r) = \rho_{core} + P_v \kappa^3 \rho_{valence}(\kappa\, r)$$

where the ρ_{atom} is the total atomic density; ρ_{core} is the core electron density and the $\rho'_{valance}(\kappa r)$ term is a spherical monopole function that represents the valance electron density, which may be deformed by the chemical environment of the atom. The κ parameter scales the radial variable *r*. If the κ value refines to a value greater than 1, the same density is obtained at a smaller radial value and the valance shell is thus contracted. Reciprocally, a kappa value that is less than one

corresponds to a valance shell that is expanded. The κ^3 term keeps the radial function normalized as κ is varied. Another consequence of using this model is that the core electrons are not perturbed to any measurable amount, which is supported by both theoretical and experimental studies.

The κ-formalism can be expanded to explicitly include the aspherical distortions of the atomic density

$$\rho_{atom} = P_c\rho_{core}(r) + P_v\kappa^3\rho_{valence}(\kappa r) + \sum_{l=0}^{l_{max}} \kappa'^3 R_l(\kappa' r) \sum_{m=0}^{l} P_{lm\pm} d_{lm\pm}(\theta, \phi)$$

where the first term now includes a fixed population parameter for the core electrons. The second term includes a κ parameter, population parameter, and radial valance parameter for the monopoles. The last term, as stated, is the valance deformation density that includes a radial function, R_l(r), along with a second radial scaling parameter κ', angular (θ, □) terms, and deformation population parameters, $P_{l,m}$. The angular terms d_{lm}(θ, □) consist of the spherical harmonics that are defined similarly to the H atom solutions of the three dimensional Schrödinger equation, but are specifically evaluated as density functions to represent distortions of the electron density [136].

The real spherical harmonics are linear combinations of the complex spherical harmonics Y_{lm} which includes a normalization factor and can be expressed as

$$Y_{lm}(\theta, \phi) = (-1)^m \left[\frac{(2l+1)}{4\pi}\frac{(l-|m|!)}{(l+|m|)!}\right]^{1/2} P_l^{|m|}\cos(\theta) e^{im\phi}$$

where m is on an interval of $-l \leq m \leq l$ and $P_l^{|m|}$ is the associated Legendre functions defined as

$$P_l^m(x) = (1-x^2)^{\frac{m}{2}} \left(\frac{d}{dx}\right)^{l+m} \frac{1}{2^l l!}(x^2-1)^l$$

The spherical harmonics are given by the relations: $y_{lm} = Y_{lm}$. There are symmetry properties that take special consideration with the spherical harmonic functions that aid in describing the atomic electronic density . When m = 0 both are Y_{l0} and y_{l0} are equal and real functions. When $l = 0$, m is also zero and the function is spherical. Values of l that are even integers are symmetric through an inversion element at the atomic center, and when l is odd, the functions are antisymmetric. These symmetries are not only important in conveying molecular geometries but are essentially in modeling the electron density of crystalline structures [136].

In theoretical calculations, wavefunctions are usually constructed from spherical harmonic functions in real form, y_{lm}, and normalization involves integration over the squares, y_{lm}^2. On the contrary, when the spherical harmonics represent a charge distribution, a different normalization constant is required because the charge is defined by the first power of the function. These density functions are denoted as d_{lmp} and are normalized as:

$$\int |d_{lmp}| d\Omega = 2 \quad when\ l > 0 \qquad \& \qquad \int |d_{lmp}| d\Omega = 1 \qquad when\ l = 0$$

Thus, a normalization of one for d_{00} implies that a population parameter of one will corresspond to a total charge density of one electron. When $l \neq 0$, for a nonspherical function, d_{lm} represents a shift of electron density corresponding to one electron between regions of opposite sign. For instance, when ($l = 1$), a dipole, where both the positive and negative regions integrate to equal but opposite numbers of electrons. In such cases, the normalization parameters dictates that the population parameters equals the number of electrons shifted from the negative lobe region to the positive lobe region. The spherical harmonic functions representing density are referred to as multipoles, centered at the nuclear positions, since the functions themselves are components of the charge distribution of $\rho(\mathbf{r})$. Specifically, when the values of l range from $0 \rightarrow 4$ the

multipoles are termed the monopole ($l = 0$); dipoles ($l = 1$); quadrapoles ($l = 2$); octapoles ($l = 3$); and hexadecapoles ($l = 4$).

The choice of radial functions is an critical component not only in describing the core electrons but the valance electrons as well, especially in cases where the expansion-contraction κ-parameter is utilized. When constructing the deformation functions for the charge density, consideration must be taken into account regarding how electron density arises from the atom-centered formalism in the field of bonding regions.

The radial functions used for the monopole are calculated from Hartree-Fock atomic radial wavefunctions. Separately, the radial functions of the spherical harmonic terms are *Slater-type* radial functions described by the following mathematical form

$$R_l = \frac{a_l^{n(l)+3}}{(n(l)+2)!} r^{n(l)} e^{-a_l r}$$

which is normalized and defines the radial dependence of each multipole function, based on the values of a_l and n_l selected. The deformation density functions have their own kappa parameters: κ', to describe the expansion-contraction parameters of the deformation density. The κ' parameters, are in a general not identical to the κ-parameter of the spherical terms in numerical terms. Coppens has evaluated the radial dependence of the multipole deformation density and found that it is interdependent with the products of the atomic orbitals in the quantum-mechanical electron density equation described by

$$\rho(\mathbf{r}) = \sum_u \sum_v P_{uv} \phi_u(\mathbf{r}) \phi_v(\mathbf{r})$$

where $P_{u\,v}$ is the population matrix element and $\square_u(\mathbf{r})\ \square_v(\mathbf{r})$ are the product functions arising from LCAO wavefunctions χ_i given by

$$\chi_i = \sum_u C_{iu}\phi_u$$

and equated with the electron density $\rho(\mathbf{r}) = \sum_i n_i \chi_i^2$ where the ϕ_u are the atomic basis functions. When considering the products of *ss*, *pp*, and *sp* orbitals, the rules of multiplication yield densities that are the same as the spherical harmonic functions corresponding to the monopolar, dipolar, and quadrapolar functions. In the same fashion, the octupoles and hexadecapoles can be interpreted as the products of the 2*p*3*d* and 3*d*3*d* orbitals respectively. However it should be noted that radial functions of 3d orbitals do represent some discrepancies, and the deformation density multipole equations represent solely bonding density centered on atoms [136].

An additional and crucial factor when considering a high order refinement deals with the effects of thermal vibrations on the intensities of diffracted beams. In general, when the temperature variable is added to the atomic form factors

$$F(h,k,l) = \sum_j f_j e^{-B\left(\frac{sin\theta}{\lambda}\right)^2} e^{2\pi i[hx+ky+lz]}$$

it becomes an essential equation in understanding the correlation between temperature and the intensity of x-ray diffraction beams.

Heat manifests itself within the atoms of a crystal as vibrational modes with a corresponding amplitude multiplied by a force constant. This is a classical approach of describing thermal movement. Since the laws of quantum mechanics forbid a temperature of zero Kelvin, and the Heisenberg Uncertainty principle requires a zero point motion, atomic thermal motion will always have an effect when considering scattering from a crystalline architecture.

Taking into account the time scales of both the X-ray scattering and the periodic vibrational motion of atoms gives an appreciable scaling of the information present when accounting for scattering from atoms in the solid state. The interaction of an X-ray photon scattering from an electron within a lattice is a fleeting process with a duration of only 10^{-18} seconds. The cycle of one period of vibrational motion of an atom is on the order of 10^{-13} seconds. Hence scattering and atomic motion have a temporal difference of five orders of magnitude. The photon-matter interaction of X-ray scattering can be described as a sampling of instantaneous orientations of the atoms in a crystalline lattice. Stewart and Feil [205] have even shown that, to a very good approximation, the averaged scattering averaged from instantaneous states agrees with the scattering of a time-averaged distribution of scattered matter. Based on these principles, structure factors based on elastic scattering can be derived from the thermally averaged electron density $\langle \rho(\mathbf{r}) \rangle$

$$F(\mathbf{H}) = \int_{unit\ cell} \langle \rho(\mathbf{r}) \rangle e^{2\pi i \mathbf{H}\cdot\mathbf{r}} d\mathbf{r}$$

which can be naturally interpreted as the Fourier transform of the averaged electron density.

The intensity of diffraction is directly dependent on the magnitude of the thermal vibrations since the size of the average atomic electron distributions is a direct function of the displacement amplitudes associated with thermal motion. The higher the temperature, the larger the displacements and the more spread out the electron probability, leading to weaker diffraction intensities. This decrease in the intensity of the X-ray scattering illustrates the inverse relationship between the real space of the thermally averaged electron density and the reciprocal space distribution of the intensities. Thus, a more diffuse atomic electron cloud leads to a more compact intensity distribution, and hence lower intensities at a given scattering angle.

Conversely, a more compact electron density, leads to a more extended intensity distribution, and hence higher intensities on the detector at the same scattering angle.

When defining the thermally averaged electron density $\langle\rho(\mathbf{r})\rangle$, a standard approach that simplifies the calculation is the *Born-Oppenheimer approximation*. The mass of the electrons are considerable lighter than the nuclei and the velocities of the electrons are a great deal larger in magnitude compared to that of the nuclei. The Born-Oppenheirmer approximation allows one to separate the total atomic wavefunction $\mathbf{\Psi}_{Total}(N, \mathrm{e}_n)$ into the products of wavefunctions based on the nuclear coordinates and electron coordinates for a n-electron system: $\mathbf{\Psi}_{Total}(N, \mathrm{e}_n) = \Psi(N)\Psi(\mathrm{e}_n)$. This allows the electronic energy and the spatial distribution of the electrons to be determined as a function of the instantaneous nuclear coordinates. The thermally averaged electron density can be further understood as the weighted average of the electron density for each individual nuclear configuration that occurs along a vibration path. The weights, are determined by the nuclear probability distribution function; $P(\mathbf{u}_1, \mathbf{u}_2, ..., \mathbf{u}_\mathrm{N})$, where $\mathbf{u}_\mathrm{i}$ are vectors specifying the nuclear positions [136].

For an electron density defined as $\rho(\mathbf{r}, \mathbf{u}_1, \mathbf{u}_2, ..., \mathbf{u}_\mathrm{N})$ where $\mathbf{r}$ is total spatial electronic configuration and $\mathbf{u}_1 \rightarrow \mathbf{u}_\mathrm{N}$ are the nuclear orientations, the time-averaged electron density is given by

$$\langle\rho(\mathbf{r})\rangle = \int \rho(\mathbf{r}, \mathbf{u}_1, \dots, \mathbf{u}_N) P(\mathbf{r}, \mathbf{u}_1, \dots, \mathbf{u}_N) d\mathbf{u}_1 \dots d\mathbf{u}_N$$

A more useful definition of the thermal averaged density can be obtained if the electrons can be assigned to specific nuclei(with an orientation vector defined as $\mathbf{r} - \mathbf{u}$), in this case, a rigid spatial construction of the density is obtained, defined as

$$\langle\rho_{rigid\ group}(\boldsymbol{r})\rangle = \int \rho_{static}(\mathbf{r} - \mathbf{u}) P(\mathbf{u}) d\mathbf{u} = \rho_{static}(\mathbf{r} - \mathbf{u}) \otimes P(\mathbf{u})$$

When considering such a rigid state, a theoretical construction can be assigned to atoms or a tightly constrained groups of atoms where the atoms can be defined as

$$\langle \rho_{atom}(\mathbf{r}) \rangle = \rho_{atom,static}(\mathbf{r}) \otimes P(\mathbf{u})$$

which states that the thermally averaged density of an atom can be seen as the convolution of the static atom density with the probability distribution [136].

If the Fourier transform is applied to $\langle \rho_{atom}(\mathbf{r}) \rangle$, the right hand side of equation is the Fourier transforms of the convolution of two functions. Applying the Fourier-convolution theorem yields the following equation

$$\langle f(\mathbf{S}) \rangle = \hat{F} \langle \rho_{atom}(\mathbf{r}) \rangle = f(\mathbf{S}) T(\mathbf{S})$$

where f(**S**); the atomic scattering factor is the Fourier transform of the individual atomic electron density distribution. The temperature factor, *T*(**S**), is the Fourier transform of the probability function *P*(**U**): $\hat{\mathcal{F}}[P(\mathbf{U})] = T(\mathbf{S})$. This particular derivation expresses an explicit path to deriving the temperature factor. The temperature factor itself can be understood as a function describing a rigid vibrating atom [136].

Further insight into the probability distribution can be ascertained with classical and statistical mechanics. A novel approach is to assume that the probability distribution corresponds to that of a series of harmonic oscillators averaged over all populated energy levels. The distribution is a collection of Gaussian function centered at the equilibrium positions of the harmonic oscillators.

For an isotropic potential moving in three-dimensions, the probability distribution equation can be expressed as

$$P(u) = (2\pi \langle u^2 \rangle)^{-3/2} e^{(-u^2/2\langle u^2 \rangle)}$$

$\langle u^2 \rangle$ is the mean-square displacement parameter amplitude. The probability distribution now gives an exact method for calculating the temperature factor by the Fourier transform:

$$T(\boldsymbol{S}) = \hat{F}[P(u)] = (2\pi\langle u^2 \rangle)^{3/2} \int e^{-u^2/\langle u^2 \rangle} e^{2\pi i \mathbf{S}\cdot\mathbf{r}} dr$$

Careful evaluation of the corresponding temperature factor yields the following mathematical expression for the temperature factor,

$$T(\boldsymbol{S}) = e^{-2\pi^2 S^2 \langle u^2 \rangle}$$

or the more familiar equivalent expression used in X-ray crystallography,

$$T(\boldsymbol{S}) = \exp\{-B(sin^2\theta/\lambda^2)\}$$

where $B = 8\pi^2\langle u^2 \rangle$. On simple examination, the temperature factor is now experessed in the form of a Gaussian function with inversely related mean-square deviations. An inverse relationship exists based on the Fourier transform, so that a diffuse thermal probability gives a compact thermal scattering function in scattering space, just as a diffuse atomic electron density gives a compact atomic scattering factor [136].

In cases where an anisotropic temperature factor $T(\boldsymbol{H})$ is evaluated, the following description summarizes the key components of the equation

$$T(\boldsymbol{H}) = e^{-2\pi^2(\mathbf{HUH}^T)}$$

where $\mathbf{H} = [h, k, l]$ is the row vector and $\mathbf{H}^T$ is column vector or the transpose of the $\mathbf{H}$ matrix and the exponent terms are expressed as

$$\mathbf{HUH}^T = [h \quad k \quad l] \begin{bmatrix} U_{11} & U_{12} & U_{13} \\ U_{21} & U_{22} & U_{23} \\ U_{31} & U_{32} & U_{33} \end{bmatrix} \begin{bmatrix} h \\ k \\ l \end{bmatrix}$$

Expansion of $\mathbf{HUT}^T$ yields the following equation for the temperature factor of an atom undergoing anisotropic harmonic motion,

$$T(H) = e^{-2\pi^2(U_{11}a^{*2}h^2 + U_{12}2a^*b^*hk\ldots)}$$

The elements of the matrix U characterize an atom centered probability distribution that may be described in terms of the principle components defined as $\mathbf{U}_{ii}$. This description is the basis of how ORTEP (Oak Ridge Thermal Ellipsoid Plot) thermal ellipsoid plots are calculated. ORTEP plots are a useful component of x-ray crystallographic analysis because they display not only the spatial arrangement of the atoms, but also the size and orientation of the anisotropic mean square amplitudes of thermal displacements. The temperature factors described are harmonic, but and can be further attenuated by refinement of anharmonic temperature factors.

Focusing on the relation between the scattered intensity and the temperature factor, it becomes evident the temperature of the crystal during an X-ray scattering measurement is a crucial parameter to consider in the experiment. Lowering the crystal temperature results in lower temperature factors and thus larger scattering factors. Lower temperatures can be achieved by a constant cryostream of an inert cold gas such as nitrogen at a temperature of 150K to 100K directed on the crystal itself. When data is collected at a lower temperature, it is possible to collect a larger number of accurate structure factors at higher scattering angles. Inclusion of high angle data in the least-square refinement leads to better nuclear positions, thermal parameters, and a more precise electron mapping with higher resolution.

It should be noted that careful consideration must be warranted when conducting low temperature x-ray scattering on solids. In many cases, if the crystalline solid has solvates within its unit cell, a change in temperature my cause cracking of the specimen due to a difference in thermal expansion coefficients. In some cases phase changes may occur within the entire crystal giving an entirely different unit cell and/or space group or twinned crystal.

In conjugation with high angle scattering, a lower temperature allows for better determination of atomic thermal displacement parameters. This allows for better deconvolution

of the static electron density from the temperature factors which yields a better model. Separation of the convolution of the static atomic scattering factor and the dynamic temperature factor is also necessary to obtain the static electron density distribution.

Once refined, the thermal parameters can be visualized using ORTEP plots to ensure that the refined parameters appear reasonable. Another method to validate the refined temperatures factors is to apply the Hirshfield test. The Hirshfield test, or rigid bond test, compares the root moon square amplitudes of vibration of bonded atoms along the bond vector direction. Since the atomic motion of internal bond stretching modes is insignificant compared to the amplitudes of the external rigid body molecular motion, agreement between the rms amplitudes indicates a reasonable set of thermal parameters and a successful deconvolution.

Augmenting the aspherical model with the improved thermal motion model not only allows for detailed and accurate modeling of the thermally averaged electron density, but allows for more plasticity in building a more precise model of the static density. In a multipole refinement, like in most crystallographic studies, the major edifice of data analysis is the least squares refinement. It is only natural to consider a least squares refinement because in multipole refinements the ratio of data to parameters is greatly over determined. In the refinement process, the sum of the differences between the observed F_o and calculated structure factors F_c is minimized by setting the derivative of the sum of the differences between observed and calculated equal to 0

$$0 = \Sigma w_i[|F_o| - k|F_c|]\frac{\partial|kF_c|}{\partial x_j}$$

where the absolute values for F_o and F_c are considered in the their evaluation and k is a scale factor. The model itself can be analyzed by calculating the residual or R-factor where

$$R = \frac{\Sigma\left||F_o| - |F_c|\right|}{\Sigma|F_o|}$$

Compared to the IAM, the aspherical scattering model yields major improvements in the R values.

There exist a number of metrics that allow one visually and numerically to ascertain how well a multipole refinement compares to experiment. The major method of testing charge density models is based on Fourier summation of the differences between structure factors from experiment and those from the model to produce a residual difference density. The residual density, $\Delta\rho(\mathbf{r})$, is the difference between the total electron $\rho(\mathbf{r})$ and a reference density, or in our case a calculated density $\rho_{calc}(\mathbf{r})$, that can be summarized as

$$\Delta\rho(\boldsymbol{r}) = \rho_{obs}(\boldsymbol{r}) - \rho_{calc}(\boldsymbol{r})$$

More specifically, the residual density $\Delta\rho(\mathbf{r})$ is obtained by Fourier summation of the difference between the observed and calculated structure factors, or $\Delta\mathbf{F} = \mathbf{F}_{obs}(\mathbf{H})/k - \mathbf{F}_{cal}(\mathbf{H})$, where $\mathbf{F}_{obs}$ is the observed structure factor and $\mathbf{F}_{cal}$ is the calculated structure factor based on the multipole model and k is the scale factor,

$$\Delta\rho(\boldsymbol{r}) = \Sigma_H \Delta\boldsymbol{F} e^{-2\pi\boldsymbol{H}\cdot\boldsymbol{r}} \cdot V^{-1}$$

Thus, the residual density is the Fourier transform of the $\Delta\mathbf{F}$. As the name implies, the residual density reveals any artifacts left over when fitting the density given by the experimental data and the density of the multipole model. The residual density in many ways reveals how well your experimental data agrees with the refined multipole model. A flatter residual density correlates to a better model agreement. The residual density not only visual depicts the difference between experiment and the model, but aids in identifying adjustments which can be made to improve the model. It should be noted that the X-ray data include experimental errors, which will result in

random fluctuations in the residual density. Thus-there is a limit to which improvements in the model will reduce the features of the residual density [136].

Other methods for evaluating the validity of the model are the extent to which the structural parameters obtained reproduce those from the refinement of high-order X-ray data and neutron diffraction data. Neutron diffraction refinements especially have provided structural results that are invaluable in improving X-ray scattering models.

Another tool in evaluating the model is the examination of the deformation density. The deformation density can be defined as the difference between the total electron density of the multipole model and a calculated density as a reference. The reference density model is calculated from unbiased positional and thermal parameters. Like the residual density, the deformation density may be obtained via the Fourier transform. In this case $\mathbf{F}_{calc}$ corresponds to a defined reference state. There exist a number of reference densities but in the study presented here and in much of the literature, the promolecule density is used. The promolecule reference model is the superposition of neutral spherical ground-state atoms, representing independent atoms prior to interatomic bonding. The difference density obtained in this case is between the multipole model and promolecule densities, and is formally termed the multipole model deformation density, given by

$$\Delta\rho(\boldsymbol{r})_{\text{deformation}} = \rho(\boldsymbol{r})_{multipole} - \rho(\boldsymbol{r})_{pro}$$

where $\Delta\rho(\mathbf{r})_{\text{deformation}}$ is the deformation density; $\rho(\mathbf{r})_{\text{multipole}}$ is the multipole model density based on the multipole scattering factors; and $\rho_{pro}(\mathbf{r})$ is the promolecule density (the IAM) [136].

If the deformation density is calculated by direct evaluation of the density functions rather than by a Fourier series, and the thermal distribution functions are omitted, then the resulting density is termed a static multipole model deformation density. In general, the main

feature the deformation density characterizes is the redistribution of density due to chemical bonding. The deformation density is therefore expected to represent major features of the covalent bonding like geometric orientation, density accumulation, hybridization, and multipole bond character. Careful consideration, however, must be given before concluding that a positive deformation density is indicative of covalent bonding, and that the absence of the deformation density is the result of the absence of chemical bonding or covalent contributions. Analysis by Savariault and Lehmann [206] of the density of the O–O bond in hydrogen peroxide shows a negative deformation density because each spherical oxygen atom of the promolecule removes 6/4 of an electron from the density in the bonding region. Studies dealing with *ab initio* calculations have also given good agreement with deformation densities.

An example that illustrates the main tenants of a multipole refinement in conjugation with analysis using Bader's AIM theory can now be discussed. In a recent paper by Stevens; et. al. [144] on the experimental and theoretical electron density distribution of α,α-trehalose dihydrate (figure 1.8), the majority of methods used in this dissertation were also employed. The impetus to study the electron distribution of α,α-trehalose dihydrate is related to understanding the cyroprotective, antidessicant properties, preservation of biomolecules, and various technical anomalies given by ^{13}C NMR spectra that give inaccurate indications of intramolecular structural group symmetry. Trehalose (α-D-glucopyranosyl-(1-1)-α-D-glucopyranose) anomalies arise from CP/MAS (cross polarization, magic angle spinning) NMR spectra giving two distinctive peaks for the two glycosidic linkage torsion angles □ (O5–C1–O1–C1') and □′ (O5'–C1'–O1–C1') dihydrate and anydrous forms, respectively, giving two distinct resolved peaks for C1 and C1'. While CP/MAS NMR is an invaluable tool in molecular elucidation, crystallographic studies have proven that □ ≈ □′ are almost identical. Molecular models have

been researched and also have also provided conflicting results as well suggesting a trehalose molecular confirmation without the exo-anomeric effect existing as an orientation present in the gas-phase form.

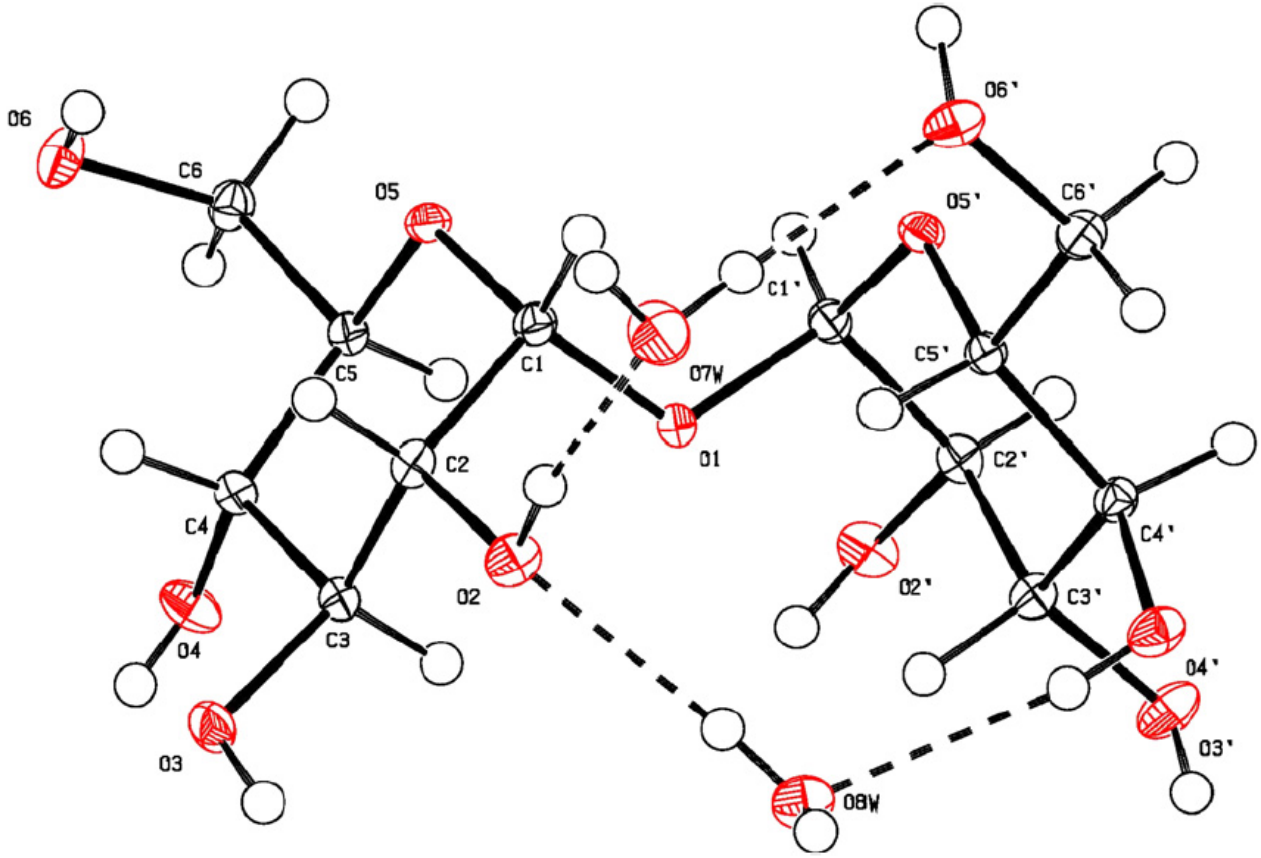

Figure 1.7 ORTEP representation of the molecular structure of α,α-trehalose dihydrate showing 50% thermal ellipsoids at 100K. Hydrogen atoms are drawn as small spheres with arbitrary radii. Two water molecules form extensive hydrogen bonding networks (dotted black lines) with each α,α-trehalose molecule. ORTEP figure taken from Carbohydrate Research, **2010,** *345(10)* [144].

The ability to perform a multipole model refinement allowed for not only experimental determination of the molecular charge density, but also provided new insight into hydrogen bonding that wasn't previously recognized.

Scattering factors of both core and valance spherical densities were calculated based on Hartree-Fock atomic wavefunctions, and scattering factors for aspherical density contributions comprised of an expansion of Slater-type radial functions and harmonic angular functions were included. Specifically, the aspherical density was expanded up to the hexadecapole level ($l = 4$) and two kappa values (κ & κ') were used as expansion/contraction parameters. The atomic and electronic parameters utilized in this research are extensive and entail not only the three positional parameters and six anisotropic thermal parameters for each atom, but also the multipole model parameters that include up to 27 additional parameters to describe the electron distribution of each atom. Constraints are usually imposed in such models on chemically equivalent atoms but in the case of trehalose none were imposed. Nonetheless mirror symmetry was imposed on specified regions that merited such considerations like the O atom plane and certain C and H atom planes. Other constraints included fixing X-H bond lengths since positional parameters are highly correlated with the dipole density functions directed along the covalent bonds for H atoms.

An ORTEP representation is shown in figure 1.8 of the asymmetric unit of α,α-trehalose dihydrate. The thermal ellipsoids correlate to the 50% probability vibrational volume of each atom at 100 K, and can be visually interpreted as the average distance of displacement of the atom from its average position. Higher temperatures for the X-ray crystallographic experiment will correspond to larger ellipsoids and of course, the reverse is true. The hydrogens in figure 1.8 are not labeled and appear as spheres since isotropic thermal parameters were used.

The deformation density for C1-O5-C5 and C'1-O5'-C5' is shown in figure 1.9 where the contours are plotted at 0.1 e A^{-3} intervals, and the solid blue lines represent positive contours and the dotted red lines represent negative contours. It is important to note that the deformation and residual map figures represent slices of the electron density of the molecule and aren't complete representations of localized regions. Of interest is the increase of lone-pair electron concentrations. Interestingly, these detailed electron maps also agree with theoretical calculations of the electron density for systems with a similar bonding environment with respect to how the molecular orbitals should be oriented in cases with hybridized orbitals. For instance, when examining the O5 oxygen, two sp^3 orbitals are apparent and participate in covalent bonds to the neighboring C1 and C5 atoms. The remaining two sp^3 orbitals on the O atoms accommodate lone pair electrons and appear in the deformation density as maxima which lie above and below the peak next to the oxygen atoms in figure 1.9 which with the expected tetrahedral geometry of sp^3-hybridized O atoms with two covalent bonds.

Correspondingly, the residual maps for C1-O5-C5 and C'1-O5'-C5' are shown in figure 1.9 and are almost devoid of any recognizable atomic or molecular electronic features. As stated, a lack of contours in the residual mappings indicate a multipole model density that greatly agrees with the experimental density. Factors that would cause concern in the residual maps are large negative or positive contours in regions corresponding to covalent bonding or localized atomic density. Throughout the refinement process, the residual maps are a critical tool in assessing where locally the multipole model needs adjustment. If pronounced and recognizable areas of density are present in specific area, it is representative of a particular region that needs adjustment.

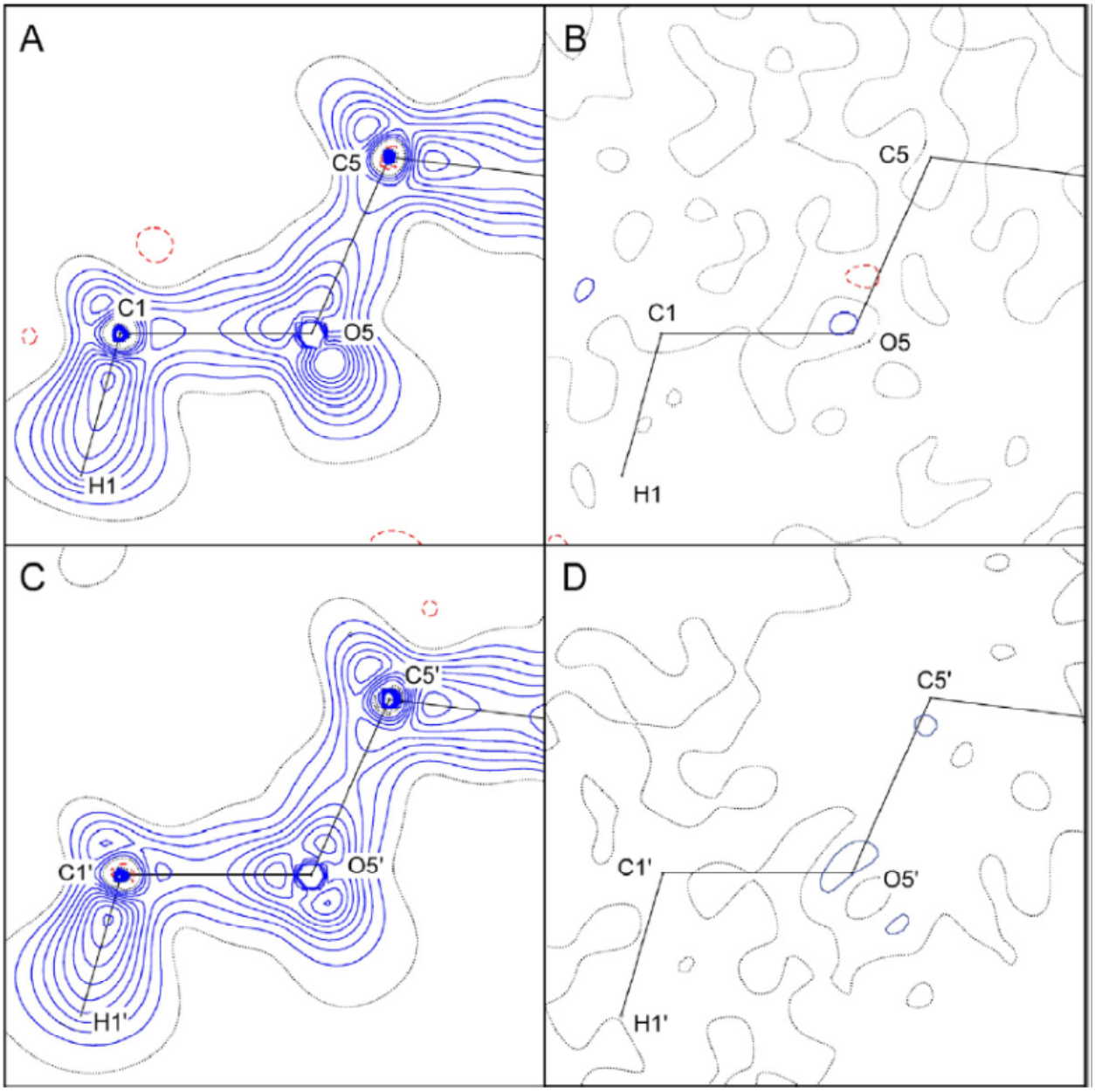

Figure 1.8 Experimental static deformation density maps (a, c) and residual maps (b, d) in the endocyclic C-O-C planes. Contours are plotted at 0.1e $Å^{-3}$ intervals with positive contours represented by solid (blue) lines, negative contours by dashed (red) lines, and the zero contour by dotted (black) lines. Figures are taken from Carbohydrate Research, **2010,** *345(10)* [144]

Analysis of trehalose using Bader's AIM theory also provided additional information especially in the case of non-covalent interactions, predominately including weak hydrogen bonding interactions that were not recognized before. All hydrogen bonds that had been identified from previous studies were confirmed. Weak hydrogen bonding was observed, namely with C-H··· O interactions, based on interatomic distances. When examining the topological maps of the C-H··· O interactions, BCP (bond critical points) where located and verified as hydrogen bonds. The BCPs were also located in densities calculated from theoretical wavefunctions.

Gradient trajectories of the experimental multipole model density were calculated in the region between the two water molecules and two adjacent trehalose molecules, and are shown on figure 10. The alcohol groups act each as a hydrogen donor on trehalose, as do the hydrogen atoms on both water molecules as well. The oxygen atoms of each alcohol group also accept one OH··· O hydrogen bond. In addition, the oxygen atom present in water, O7, accepts one O-H··· O hydrogen bond, while the second water molecule with the O8 atom accepts two 2 O-H··· O hydrogen bonds. The gradient trajectory maps shown in figure 1.10 display the zero flux surfaces, atomic basins, and bond paths.

Comparison of the BCP properties of both covalent and hydrogen bonds observed in trehalose dihydrate based on the x-ray electron density distribution measurements were generally in good agreement with theoretical DFT calculations of the same quantities where small molecule fragments were included to mimic the crystalline environment in the calculations.

The following dissertation is focused on gossypol derivatives that exhibit varied complex electronic structure that is well suited for both crystallographic and charge density studies. Specifically, seven crystallographic gossypol amine derivatives were investigated and one amine

derivatives was the subject of a charge density analysis. Previous structural work on dimethoxy gossypol was extended to include a charge study as well. As stated, gossypol derivatives show varied chemistry properties resulting from complex electronic interactions, and are thus prime candidates for the research presented.

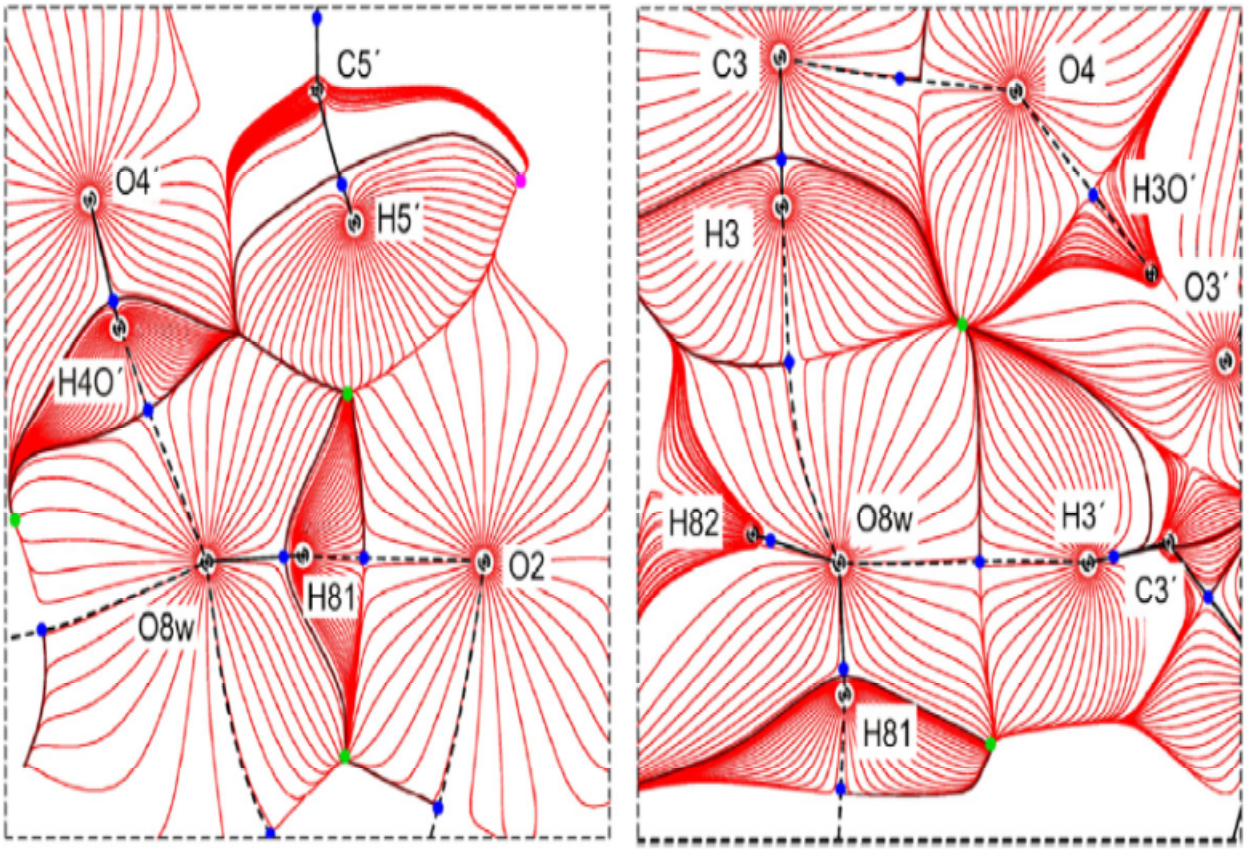

Figure 1.9 Gradient trajectory plots of the experimental density distribution near the O(8w) water molecule. Gradient trajectories (red lines) originate at atomic centers and terminate at bond critical points (blue circles), ring critical points (green circles), or cage critical points (red circles. Bond paths corresponds to covalent bonds are indicated by solid (black) lines, and bond paths corresponding to hydrogen bonds are indicated by dashed (black lines. Zero flux surfaces, which define the boundaries of atomic basins, are also indicated by solid (black) lines. On the left are the gradient trajectories corresponding to the atoms involved in the O4'-H(O4')... O8w and O2... H81-O8w hydrogen bonds. On the right are the gradient trajectories corresponding to the C3'-H3... O8w and C3-H3... O8w hydrogen bonds. Figures are taken from Carbohydrate Research, **2010,** *345(10)* [144].

Methods & Materials

Crystals of di(propylamino) gossypol ($C_{38}H_{44}N_2O_6$), di(3-phenylpropylamino) gossypol ($C_{48}H_{52}N_2O_6$), di(t-butylamino) gossypol($C_{38}H_{48}N_2O_6$), di(3-hydroxypropylamino) gossypol ($C_{36}H_{44}N_2O_8$), and di(methoxy) gossypol ($C_{32}H_{34}O_8$) were obtained by adding the respective compounds to various solvents in 2mL HPLC vials until saturated and then heating in a thermal block at a temperature between 90-100 C° from 1-5 minutes. Additional material was then added to the heated solution to induce a super saturated state and then placed in dark storage at room temperature to cool. Petroleum ether was added in small increments to further induce crystallization for some cases. Di(propylamino) gossypol crystals were grown in a 100% ethanol solution and a few drops of petroleum ether to further induce saturation and crystal of $0.40 \times 0.25 \times 0.20$ mm^3 size was obtained. A secondary di(propylamino) gossypol solvated crystal with dimensions $0.40 \times 0.20 \times 0.15$ mm^3 was retrieved from an isopropanol solution. Two crystals for di(3-phenylpropylamino) gossypol with the dimensions of $0.50\times 0.40 \times 0.30$ mm^3 and $0.60 \times 0.40 \times 0.20$ mm^3 were attained from propanol and used for low and room temperature data collection respectfully. Two di(t-butyl amino) gossypol crystals were obtained with dimensions of $0.30 \times 0.25 \times 0.20$ mm^3 and $0.50 \times 0.20 \times 0.20$ mm^3, both from a saturated solution of cyclohexanone. A large number of crystals were obtained for di(t-butyl amino) gossypol, specifically by over saturating 100 mL of cyclohexanone in an Erlenmeyer flask with di(t-butylamino) gossypol and then vacuum filtering to remove excess material not in solution. The solution was then divided into an array of individual 2 mL HPLC tubes. A large crystal of di(3-hydroxypropylamino) gossypol of dimensions of $0.45 \times 0.45 \times 0.20$ mm^3 was isolated from an acetone solution. In some cases, crystal formation was not observed in the first few days of

incubation. In the case for aminopropyl gossypol, crystal growth did not occur for several months.

Each of the crystals was then mounted on a Bruker APEX II 4K Kappa CCD four-circle diffractometer. Di(propylamino) gossypol, di(3-phenyl propylamino) gossypol, di(methoxy) gossypol and two di(t-butylamino) gossypol crystals were cooled to 120(2) K by a cold N_2 gas stream generated with an Oxford cryosystems 700 low temperature device during the diffraction process. Additionally, a di(3-phenyl propylamino) gossypol crystal was examined at room temperature (293 K). The incident X-ray beam was generated from a standard focus molybdenum X-ray target tube with a graphite monochromator. A collimator measuring 0.6mm was employed to provide suitable illumination that was uniform within ± 5% throughout the crystal sample volumes.

A series of X-ray intensities were measured in various orientations using ω and scans of 0.50˚ increments through a complete range of 360˚ at a distance of 6.00 cm from the crystal to detector. A total of 36 scans were collected for MG (di*M*ethoxy *G*ossypol): 6 scans at 5 seconds per frame with the detector at 2θ = 15°; 8 scans at 10 seconds per frame with the detector at 2θ = 27°; 8 scans at 20 seconds per frame with the detector at 2θ = 50°; 7 scans at 30 seconds per frame with the detector at 2θ = 78°; and 7 scans at 60 seconds per frame with the detector at 2θ = 89°. For PAG-**S1** (**solvated**), the solvated **S1** crystal was measured with a total of 14 scans: 7 scans consisted of 30 seconds per frame with the detector at 2θ = −37.00˚. A total of 6 scans were taken for PPAG [di(3-*P*henyl*P*ropyl*A*mino) *G*ossypol]. The ordered polymorphic PPAG-**P1** crystal was measured with a total of 6 scans at 30 seconds per frame with the detector positioned at 2θ = −28.00˚. The other polymorph of the PPAG molecule in the disordered state, PPAG-**P2**, was measured using a total of 3 scans: two scans at 10 seconds per frame with a 2θ =

−28.00˚; and 1 set of scans at 10 seconds per frame with 2θ = 28.00˚. Two crystals of TBAG [di(*T*-*B*utyl*A*mino) *G*ossypol] which were solvated with cyclohexanone were examined: one containing disordered solvent, TBAG-**S2,** and the with no disorder of the solvent, TBAG-**S1**. The solution set for **S1** required a total of 7 scans that were all performed all at 60 seconds per frame and 2θ = −37.00˚. The data set for the second solvate of, TBAG-**S2**, with disorder, consisted of a total collection of 7 scans. All seven scans were at 60 seconds per frame with 2θ = −47.00˚. The HPAG-**S1** [di(3-*H*ydroxyl*P*ropyl*A*mino) *G*ossypol] solvate required a total of 11 scans: a series of 7 scans at 60 seconds per frame at 2θ = −37.00˚ and 4 scans at longer exposure times of 90 seconds per frame at 2θ = −57.00˚. The PAG unsolvated crystal was measured using a total of 37 scans: 7 scans with 30 seconds per frame at 2θ = −37.00˚; 1 scan at 60 seconds per frame at 2θ = −87.00˚; 1 scan at 30 seconds per frame duration at 2θ = 5.00˚; 7 scans at 60 seconds per frame at an angle 2θ = −87.00˚; 7 scans at 30 seconds per frame at 2θ = 40.00˚; 7 scans at 60 seconds per frame at angle 2θ = 80.00˚; 1 scan at 30 seconds per frame at 2θ = 50.00˚; and 6 scans at 60 seconds at 2θ = 50.00˚.

The number of scans, exposure time to X-rays, and the complete duration of collection of data was dependent on whether a charge density study was being performed on the crystal specimen. Crystal specimens that were selected for charge density studies included di(methoxy) gossypol and di(propylamino) gossypol. These required longer exposure times and more scans to increase resolution and redundancy. Data for all other crystals was collected with fewer scans requiring a shorter amount of time. The orientation of the nitrogen stream was coaxial approximately to the ω scan axis, and for most scans, the χ angle remained fixed at 54.74˚. As a result the crystal mount remained approximately at a constant angle with respect to the nitrogen cold stream throughout the scans.

The raw diffraction peak intensities collected on the detector were integrated with the Bruker software program SAINT and empirical absorption corrections were applied with the SADABS program, both part of the Bruker APEX II software suite [208]. The minimum to the maximum transmission factors, as well as other vital data on the data collection are included in the crystal data tables for each compound. All the crystal structures were analyzed, solved, and refined based on the spherical atom model with SHELXTL [209]. PLATON was also implemented for further analysis [210]. All the structures were solved by direct methods and were refined by least squares fitting of F^2 over all unique reflections. Additionally, all non-hydrogen atoms were modeled with anisotropic temperature factors. Hydrogen atoms, for most cases, were found in difference maps and were refined isotropically. Where disorder was present in either the aliphatic amine side chains [di(propylamino) gossypol] or solvate [hexanone with di(t-butylamino) gossypol], hydrogen atoms were modeled and placed in calculated positions to improve molecular geometries. To improve the thermal motion parameters of disordered atoms, DELU and SIMU restraints were applied.

The atom labels for both the gossypol amine derivatives and guest molecules were selected to agree with numbering schemes from previous research studies and past publications. Except for MG, all other cases presented here contain no internal symmetry. When present, the internal symmetry usually consists of a 2-fold rotation axis passing through the midpoint of the internaphyl bridging bond between the two major ring structures. This can result in a varying numbering scheme. The carbon atoms composing the two naphthalene rings are labeled C1 → C10 and C11 → C20. The periphery carbon atoms of the first naphthalene ring are numbered C21 → C25 (C21 the lone methyl group; C22-C24 the isopropyl group; and C25 the aldehyde group). The secondary naphthalene periphery carbon atoms are labeled C26 → C30 (C26 the

lone methyl group; C27-C29 the isopropyl group; and C30 the aldehyde group). The oxygen atoms, usually consisting of alcohol and aldehyde groups are labeled O1 → O4 on the first naphthalene structure. Oxygen atoms decorating the second naphthalene ring are identified as O5 → O8. In the case for MG, the methoxy carbon atoms are labeled C31 on the primary ring and C32 on the secondary ring. In previous studies and in the literature, disorder is often observed in the isopropyl groups but in this investigation no disordered states were present that affect the numbering order. For the amine derivatives that form Schiff bases with the aldehyde groups at C22 and C27, the carbon count continues from the primary naphthalene ring at C31 → C(31 + *n*) where *n* is the carbon count of the amine side chain and continues to the secondary naphthalene ring on the second amine side chain. The nitrogen located on the primary naphthalene structure is numbered N1, followed by N2 located on the second Schiff base on the adjacent naphthalene ring. Any other atoms such as oxygen continue on the numbering order from the highest numbers for any specific atom group already mentioned starting from the first ring and continuing on the second ring system. The numbering scheme finally continues to the respective solvates for each crystal structure.

There are several discrepancies, however, with how the oxygen atoms are labeled on the amine derivatives and their respective solvates. Two differing numbering schemes are present where the oxygen atoms of both di(aminopropyl) gossypol are the same and all other amine derivatives follow a secondary numbering of oxygen. These two varying numbering schemes are due to the aldehyde oxygen atoms counted as O2 and O6 being substituted with nitrogen atoms. The PAG-**S1** and PAG oxygen numbering begins with the innermost hydroxyl oxygen as O1 and all other oxygen atoms pertaining to the OH groups in increasing order giving the first naphthalene ring the O1 → O3 atoms and the secondary ring system O4 → O6 atoms. The

numbering scheme for all other amine derivatives follow the same unsubstituted oxygen atom numbering even through the aldehyde oxygen atoms (O2 and O6) are not present. The PAG-**S1** unit cell contains two acetone units where each carbonyl oxygen atoms are labeled O8 and O9. The HPAG-**S1** structure contains two peripheral alcohol groups located on the substituted amino alkyl chains labeled O2 and O6. The HPAG-**S1** unit cells solvates, acetone and 1/2 water molecules are oxygen atoms are labeled O50 and O60, respectively.

Multipole Refinement

Charge density studies were conducted for both di(methoxy) gossypol and di(propylamine) gossypol. The experimental electron distribution for the charge density was obtained from the crystallographic diffraction data by refinement with the Hansen-Coppens multipole deformation model as coded in the XD2006 computer program. In this model, the total density for each atom is fit by a spherical core and valance electron density calculated from Hartree-Fock atomic wavefunctions and an additional aspherical density contribution consisting of an expansion of Slater-type radial functions and spherical harmonic angular functions where the density for each atom is defined as

$$\rho_{atom}(\boldsymbol{r}) = \rho_{core}(\boldsymbol{r}) + P_{valence}\kappa^3\rho_{valence}(\kappa\boldsymbol{r}) + \Sigma_l\kappa'^3 R_l(\kappa'\boldsymbol{r})\Sigma_m P_{l,m}Y_{l,m}(\theta,\phi)$$

where the spherical core density component, $\rho_{\text{core}}(\mathbf{r})$, is fixed, while the valance density component, $\rho_{\text{valance}}(\mathbf{r})$, may be adjusted by the refinement of the valence population parameter, P_{valance}, and the expansion/contraction parameter: κ. Components representing aspherical density contributions are obtained by refinement of the multipole population parameter, $P_{l,m}$ for each individual density deformation function in the spherical harmonic expansion up to the

hexadecapolar ($l = 4$) level, and by further adjustment by a second expansion/contraction parameter: κ'. Refinement of the parameters for the electron configuration of each atom entails three positional parameters; six anisotropic thermal displacement factors for each atom; the multipole model introduces an additional 27 parameters for the electronic distribution giving a total of 36 parameters for each atom.

Despite the high degree of parameterization defined with the multipole refinement process, the number of variables may be reduced in its implementation with restraints. For instance, chemically equivalent atoms may be constrained to have the same density. Naturally, the validity of such constraints must be tested by examining the quality of the fit to the x-ray data.

In general, the positional parameters for hydrogen atoms are highly correlated with the dipole density deformation directed along the covalent bonds, and concurrent refinement cannot reliably determine both parameters. In like manner, the hydrogen atomic temperature factors are correlated with both the monopoles and quadrapoles deformation parameters. The model used for multipole refinement of the hydrogen atoms included isotropic thermal parameters fixed at the experimental values obtained from the spherical atom refinement, and hydrogen positions fixed at positions calculated by extending along the X-H bond direction to a distance corresponding to average X-H bond distances obtained from neutron diffraction experiments. With both the hydrogen positional and thermal parameters constrained, only the valance monopoles and the single monopole and quadrapole deformation parameters aimed along the major covalent bond axis are refined. Following each cycle of refinement, the hydrogen atom positions are reoriented to maintain the specified bond lengths.

A total of nine sets of κ and κ' values are designated for di(methoxy) gossypol: one set for the oxygen atoms in the aldehyde groups, one set for the oxygens in the alcohol groups, one set for the oxygen atom in the methoxy groups, one set for the carbon atoms, and one set for the hydrogens atoms bonded to carbon, and one set for the hydrogens bonded to oxygen. For PAG, a total of seven sets of κ and κ' values are designated: one set for the oxygen atoms in the hydroxyl groups, one set for the oxide oxygen atoms, one set for the carbon atoms, one set for the nitrogen atoms, one set for the hydrogen atoms bonded to carbon, one set for the hydrogen atoms bonded to oxygen, and one set for the hydrogen atoms bonded to nitrogen. Moreover the small extinction coefficient from the spherical atom refinement is also included as a fixed value in the more complex multipole refinement.

To further test the validility of the deformation density models used in the multipole refinement process, and the successful completion of the deconvolution of the electronic density and thermal motion, electronic residual density maps are tested locally and globally throughout the refinement process. As stated, the residual density maps relate the difference between the observed density and the density calculated on the basis of the multipole model calculated by Fourier summation

$$\Delta\rho_{residual} = \rho_{obs} - \rho_{model} = (1/V)\Sigma_{hkl}[|F_{obs}| - |F_{model}|]e^{2\pi i(hx+ky+lz)}$$

In general, where significant features corresponding to considerable electron density were observed in the residual density, site symmetry constraints on the deformation and/or chemical constraints parameters were relaxed and the refinement process continued until no areas remained with significant density features that are greater than three times the estimated standard deviation in the residual density (estimated $\sigma(\Delta\rho) = 0.051$ e A^{-3}).

Further validity of the multipole refinement entails conformation of the deformation density via the rigid bond test [207]. Anisotropic thermal atomic displacement parameters that have been successfully deconvoluted from the molecular electron density organization should exhibit equal mean square amplitudes of vibration along the bond direction for covalently bonded pairs of atoms.

A static deformation density plot was calculated by taking the difference between the sum of the atomic densities given by $\rho_{\text{multipole model}} = \Sigma\rho_{\text{atom}}$, and the sum of the isolated, neutral atomic densities, $\rho_{\text{IAM}} = \Sigma\rho_{\text{spherical atom}}$, the independent atom model (IAM),

$$\Delta\rho_{deformation\ density} = \rho_{multipole\ model} - \rho_{IAM}$$

Topological properties and analysis of the electron density organization based on Bader's AIM theory were calculated with the XDPROP and TOPXD modules of XD2006. The estimated standard deviations in the general properties are rigorously calculated based on the uncertainties of the multipole population parameters obtained by the least squares refinement of the X-ray data.

Results

Crystallographic Results

The structures of all eight gossypol derivatives determined were in the aldehyde tautomeric form which is the only form observed in gossypol and other gossypol derivative crystal structures to date. Four of the crystal structures did include solvent in the unit cell. These were di(methoxy)gossypol (MG), di(propylamino)gossypol (PAG), and two polymorphs of di(3-phenylpropylamino)gossypol (PPAG) labeled PPAG-**P1** and PPAG-**P2** with structure determinations at 120K and 293K, respectively. For **P2,** the room temperature crystalline state was disordered with the amino phenylpropyl side chains occupying two orientations. Solvates were present in only the amino derivatives consisting of di(propylamino)gossypol (PAG-**S1**) solvated with acetone (1:2) ratio of host/guest ratio; two structure solutions for di(t-butylamino) gossypol (TBAG), both at 120K solvated with cyclohexanone (1:1), where one structure solution contained disordered conditions (TBAG-**S2**) within the cyclohexanone unit and the non disordered state labeled TBAG-**S1**; and di(3-hyroxypropylamino) gossypol (HPAG-**S1**) solvated with both acetone and 1/2 water molecules (1:2:0.5) ratio respectively. Seven of the eight crystal structures were determined in monoclinic crystal systems and the disordered TBAG-**S2** in a triclinic system. The space group classification for the solvates: PAG-**S1**, TBAG-**S1** (ordered), and HPAG-**S1** was $P2_1/n$; and for TBAG-**S2** (disordered) space group $P\bar{1}$. The non solvated derivatives were found to crystallize in a variety of space groups including both di(3-phenylpropylamino)gossypol (PPAG-**P1** and PPAG-**P2**) in $P2_1/c$; MG in C2/c; and di(propylamino)gossypol (PAG) in the *P*-1 space group.

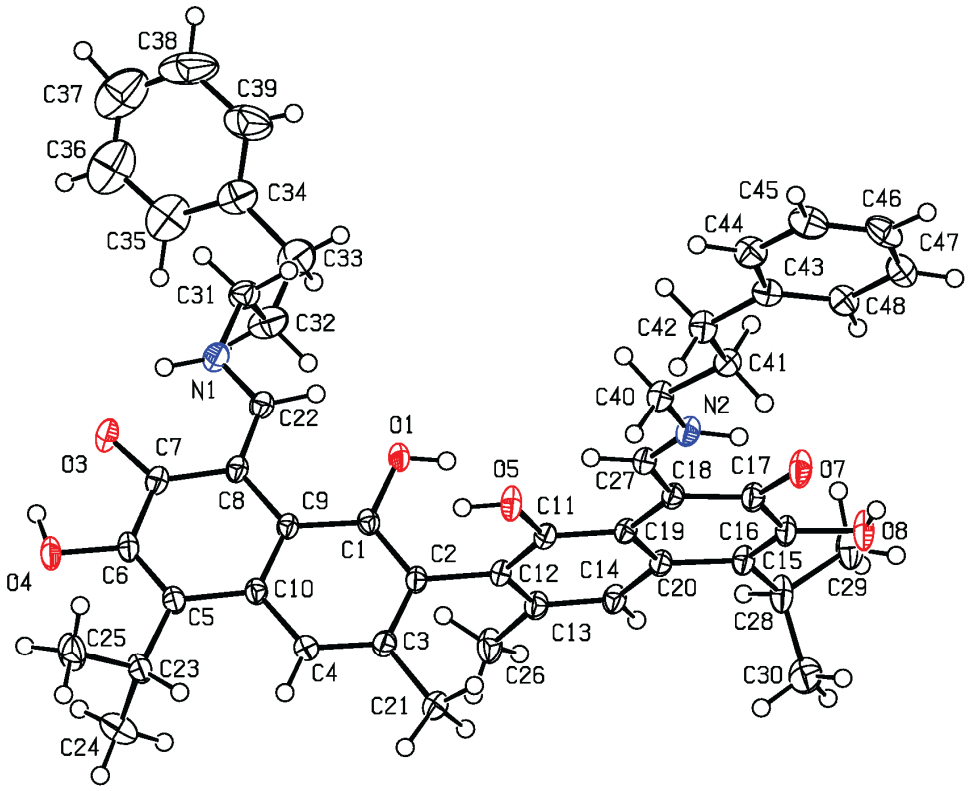

Figure 3.1 Di(3-phenylpropyl)gossypol crystal structure collect at 120K.

Empirical formula	$C_{48}\ H_{52}\ N_2\ O_6$	
Formula weight	752.92	
Temperature	120(2) K	
Wavelength	0.71073 Å	
Crystal system, Space group	Monoclinic, $P2_1/c$	
Unit cell dimensions	a = 11.9559(9) Å	α= 90.0°
	b = 29.079(2) Å	β= 94.207(1)°
	c = 11.6918(9) Å	γ = 90.0°
Volume, Z	4053.9(5) $Å^3$, 4	
Density (calculated)	1.234 Mg/m^3	
Crystal size	0.50 x 0.40 x 0.30 mm^3	
2 Theta range for data collection	4.42 to 54.96°.	
Reflections collected	58753	
Independent reflections	9192	
Parameters / Restraints	705 / 73	
Final R indices [I > 2σ]	R_1 = 0.0453, wR_2 = 0.1214	

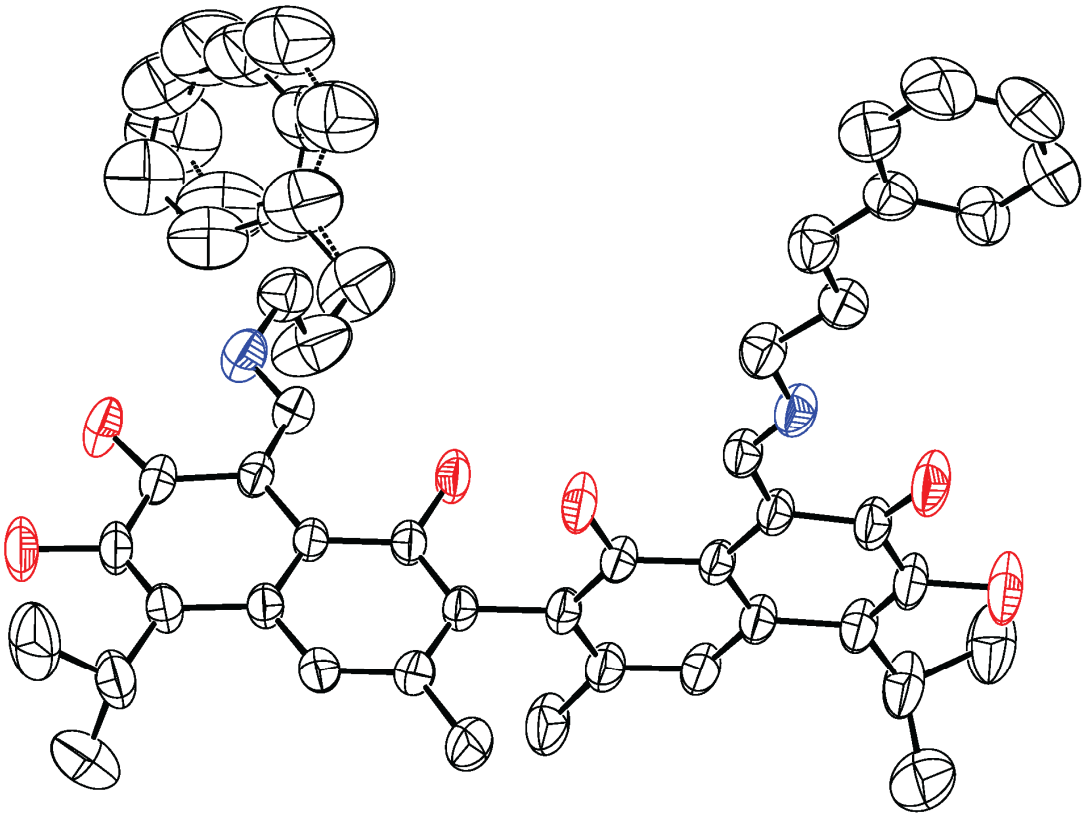

Figure 3.2 Di(3-phenylpropylamino)gossypol at 293 Kelvin with disorder on the phenyl ring.

Empirical formula	$C_{48}\ H_{52}\ N_2\ O_6$	
Formula weight	752.92	
Temperature	293(2) K	
Wavelength	0.71073 Å	
Crystal system, Space group	Monoclinic, $P2_1/c$	
Unit cell dimensions	a = 12.0729(9) Å	α= 90.0°
	b = 29.176(2) Å	β= 94.207(1)°
	c = 11.8511(9) Å	γ = 90.0°
Volume, Z	4162.0(5) $Å^3$, 4	
Density (calculated)	1.202 Mg/m^3	
Crystal size	0.60 x 0.40 x 0.20 mm^3	
2 Theta range for data collection	2.20 to 27.00°.	
Reflections collected	58753	
Independent reflections	9074	
Parameters / Restraints	705 / 73	
Final R indices [I > 2σ]	R_1 = 0.0535, wR_2 = 0.1672	

ORTEP diagrams of the asymmetric units of both di(3-phenylpropylamino) gossypols: **P1**(low temperature) and **P2**(room temperature) are plotted in figure 3.1 & figure 3.2, and illustrate the atomic numbering scheme and the thermal ellipsoids corresponding to the atomic displacement parameters observed at both 120K and 293K. Clearly the **P2** structure collected at higher temperature corresponds to higher thermal displacement parameters, as expected. Although the thermal displacement parameters are expected to be directly proportional to the absolute temperature, the average ratio of the equivalent isotropic displacement factors, (for example, the oxygen and carbon atoms on di(3-phenylpropylamino) gossypol) at 293K divided by the equivalent parameters of the corresponding atoms of the same compound at 120K is only (1.8), which is less than the expected 2.4:1 ratio of temperatures. This discrepancy maybe attributed to the effects of zero point motion of the lowest quantum vibrational states at very low temperature.

The molecular structures of all seven gossypol amine derivatives and MG at both low and room temperatures didn't reveal any substantially different forms when compared to previous reported structure determinations of derivatized chains. In all low temperature cases, especially with the **P1** and **P2** equivalent structures, the atomic thermal displacement parameters are smaller, and atoms are slightly shifted. The standard deviations are lower in the structural parameters reflecting the significantly higher resolution of the data collected for PAG (unsolvated) and MG structures, which is also the case for the charge density studies which require large amounts of high-resolution, redundant data.

Crystals with disorder present in the amino propyl phenyl rings of PPAG-**P2** came from the same series of crystallization experiments as the ordered PPAG-**P1** structure. Both **P1** and **P2** were X-ray diffraction experiments conducted at 120K in essentially comparable

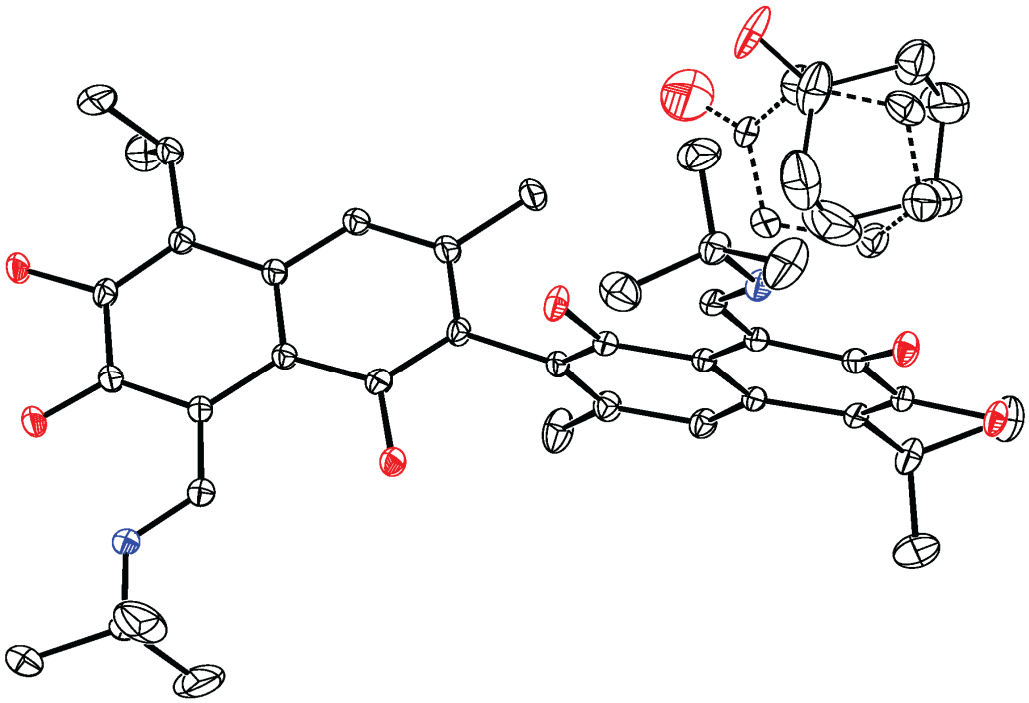

Figure 3.3 Di(T-Butylamino)gossypol at 120K with disorder in hexanone solvate.

Empirical formula	$C_{38}\,H_{48}\,N_2\,O_6 \cdot C_6\,H_{10}\,O$	
Formula weight	726.92	
Temperature	120(2) K	
Wavelength	0.71073 Å	
Crystal system, Space group	Triclinic, P-1	
Unit cell dimensions	a = 11.895(2) Å	α= 93.8°
	b = 11.899(2) Å	β= 106.203(3)°
	c = 14.627(3) Å	γ = 94.9°
Volume, Z	1971.5(5) $Å^3$, 4	
Density (calculated)	1.224 Mg/m^3	
Crystal size	0.50 x 0.20 x 0.20 mm^3	
2 Theta range for data collection	1.70 to 27.50°.	
Reflections collected	82829	
Independent reflections	9065	
Parameters / Restraints	538 / 0	
Final R indices [I > 2σ]	R_1 = 0.0514, wR_2 = 0.1560	

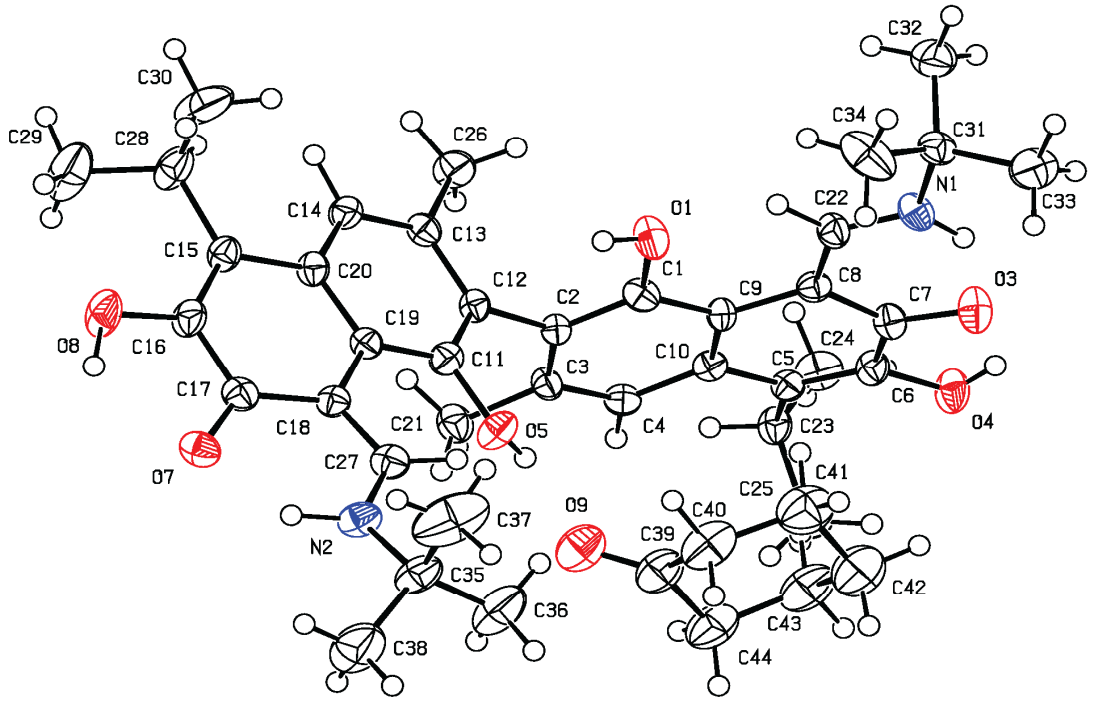

Figure 3.4 Di(t-butylamino)gossyol ORTEP collection at 120K.

Empirical formula	$C_{38}H_{48}N_2O_6 \cdot C_6H_{10}O$	
Formula weight	726.92	
Temperature	120(2) K	
Wavelength	0.71073 Å	
Crystal system, Space group	Monoclinic, $P2_1/n$	
Unit cell dimensions	a = 17.644(3) Å	α= 90.0°
	b = 12.334(2) Å	β= 106.203(3)°
	c = 19.131(3) Å	γ = 90.0°
Volume, Z	3997.7(10) $Å^3$, 4	
Density (calculated)	1.208 Mg/m^3	
Crystal size	0.30 x 0.25 x 0.20 mm^3	
2 Theta range for data collection	3.98 to 52.96°.	
Reflections collected	74250	
Independent reflections	8225	
Parameters / Restraints	538 / 0	
Final R indices [I > 2σ]	R_1 = 0.0524, wR_2 = 0.0783	

experimental conditions. In a similar result, the TBAG-**S1** structure had no disorder while the TBAG-**S2** structure had two disordered orientated states for one of the cyclohexanone solvent molecules within the unit cell (fig. 3.3 & fig. 3.4). The HPAG-**S1** structure contained disorder in one of the amine propyl alcohol chains and disorder with the water solvent (fig. 3.5). Interestingly, both of the amino propyl chains were disordered in PAG-**S1** (fig. 3.6). The ORTEP for di(propylamine) gossypol did not show any disorder (fig 3.7).

The TBAG-**S1** structure contained one aliphatic ring in the "chair" form of cyclohexanone per TBAG molecule characterized by Cremer-Popel puckering parameters of Q = 0.535(4) A□ , θ = 172.8(4)˚, □ = 13.(3)˚ for C39 → C44 atoms. The TBAG-**S2** structure contained a cyclohexanone ring disordered in two different chair form orientations with the major component described by Cremer Popel puckering parameters of Q = 0.613(5) A□ , θ = 2.9(5)˚, □ = 45(11)˚ for the C39 → C44 atoms; and the minor component by Q = 0.531(5) A□ , θ = 11.9(5)˚, □ = 213(2)˚ for the C45 → C50 atoms.

The bridged naphthalene ring orientations on each of the molecules are situated generally perpendicular to each other with angles between best-fit ring planes ranging from 0.108Å to 0.048Å. Any atomic deviations from the ring planes are commonly small and similar to deviations observed in most gossypol crystallographic studies. When accounting for the root-mean-square average deviation for the atoms comprising of the naphthalene ring structures for the unsolvated gossypol amine derivatives and MG, larger variances where present than the solvated forms of the gossypol derivatives.

The isopropyl groups on the gossypol amine derivatives and MG have similar spatial orientations and an ORTEP diagram is shown in figure 3.8. While there are differences in the spatial displacement of the isopropyl groups for all seven gossypol crystal structures, in general,

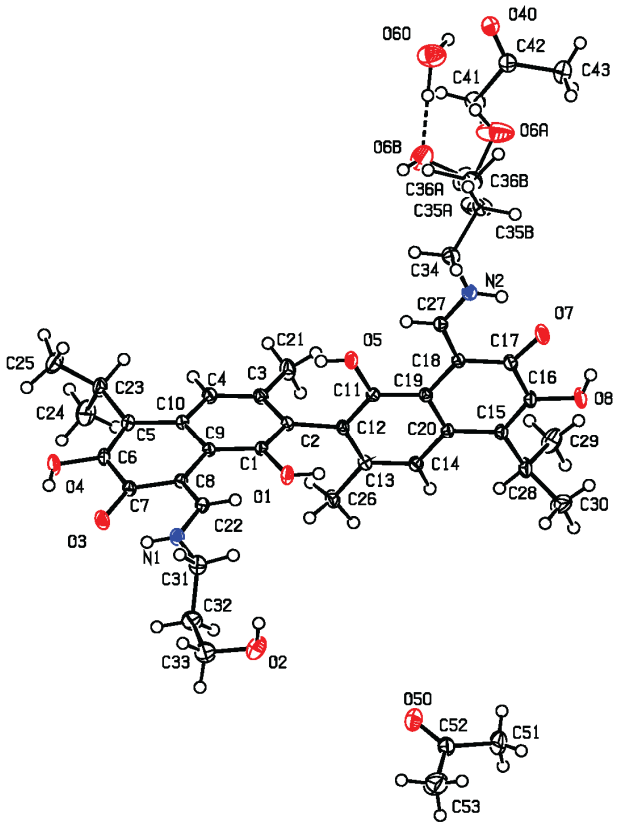

Figure 3.5 Di(3-hydroxypropylamino)gossypol ORTEP collected at 120(2)K.

Empirical formula	$C_{36}H_{44}N_2O_8 \cdot 2\,C_3H_6O \cdot 0.5\,H_2O$	
Formula weight	726.92	
Temperature	120(2) K	
Wavelength	0.71073 Å	
Crystal system, Space group	Monoclinic, $P2_1/n$	
Unit cell dimensions	a = 12.9950(4) Å	α= 90.0°
	b = 11.4724(3) Å	β= 95.953(1)°
	c = 26.6998(7) Å	γ = 90.0°
Volume, Z	3959.04(19) $Å^3$, 4	
Density (calculated)	1.272 Mg/m^3	
Crystal size	0.45 x 0.45 x 0.20 mm^3	
2 Theta range for data collection	4.70 to 55.00°.	
Reflections collected	42539	
Independent reflections	9072	
Parameters / Restraints	743 / 140	
Final R indices [I > 2σ]	R_1 = 0.0408, wR_2 = 0.1133	

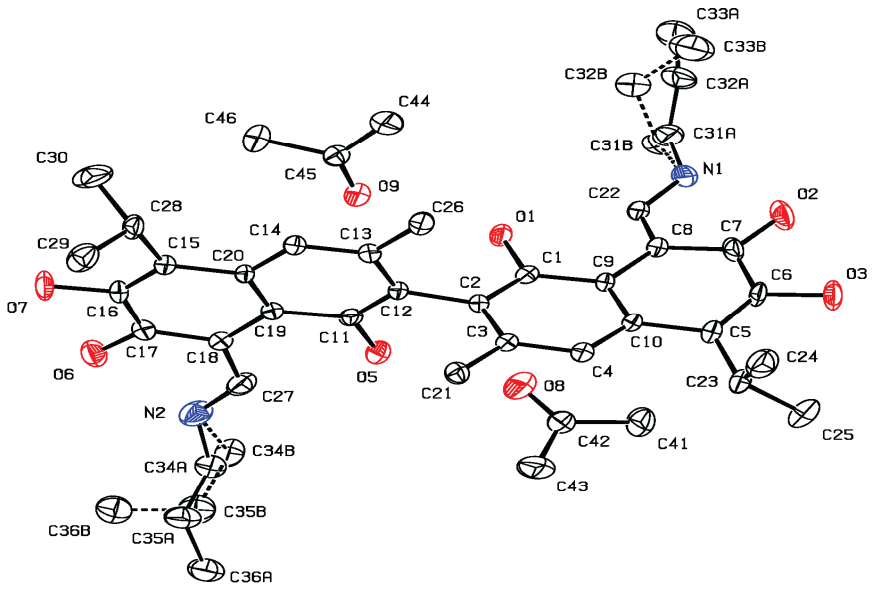

Figure 3.6 Di(propylamino)gossypol with the acetone solvate ORTEP collected at 120(2)K.

Empirical formula	$C_{38}\ H_{44}\ N_2\ O_6 \cdot 2\ C_3\ H_6\ O$	
Formula weight	716.89	
Temperature	120(2) K	
Wavelength	0.71073 Å	
Crystal system, Space group	Monoclinic, $P2_1/n$	
Unit cell dimensions	a = 12.7928(6) Å	α= 90.0°
	b = 11.4174(6) Å	β= 96.880(1)°
	c = 26.8570(13) Å	γ = 90.0°
Volume, Z	3894.5(3) $Å^3$, 4	
Density (calculated)	1.223 Mg/m^3	
Crystal size	0.40 x 0.20 x 0.15 mm^3	
2 Theta range for data collection	5.20 to 50.00°.	
Reflections collected	133138	
Independent reflections	6866	
Parameters / Restraints	558/ 168	
Final R indices [I > 2σ]	R_1 = 0.0649, wR_2 = 0.1467	

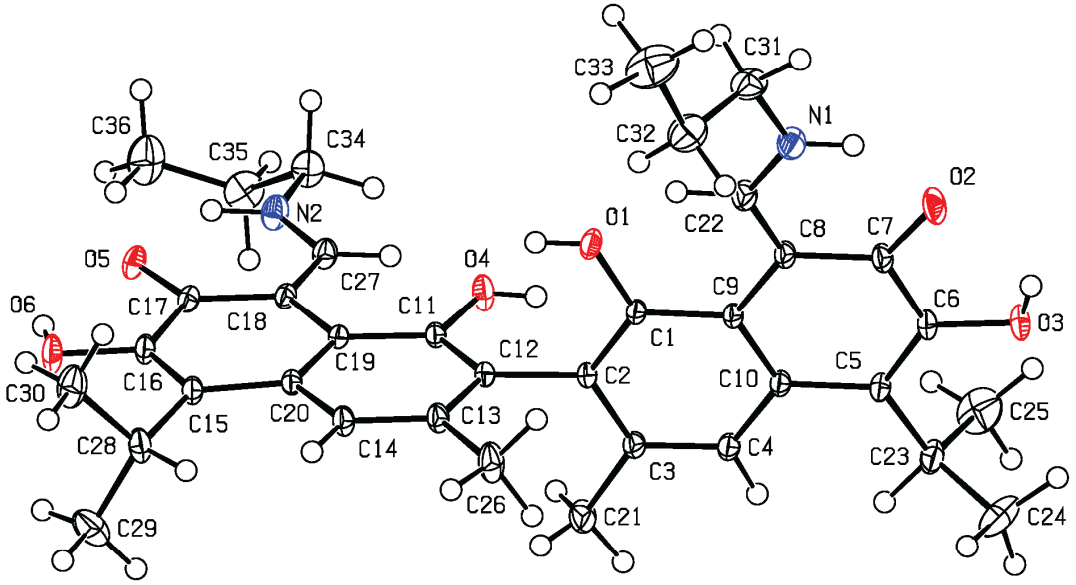

Figure 3.7 Di(propylamino)gossypol ORTEP collected at 120K.

Empirical formula	$C_{38}H_{44}N_2O_6$	
Formula weight	600.73	
Temperature	120(2) K	
Wavelength	0.71073 Å	
Crystal system, Space group	Monoclinic, $P2_1/n$	
Unit cell dimensions	a = 12.7928(6) Å	α= 90.0°
	b = 11.4174(6) Å	β= 96.880(1)°
	c = 26.8570(13) Å	γ = 90.0°
Volume, Z	1600.1(3) $Å^3$, 4	
Density (calculated)	1.247 Mg/m^3	
Crystal size	0.40 x 0.20 x 0.15 mm^3	
2 Theta range for data collection	2.00 to 45.40°.	
Reflections collected	207306	
Independent reflections	26663	
Parameters / Restraints	2663 / 573	
Final R indices [I > 2σ]	R_1 = 0.0548, wR_2 = 0.1810	

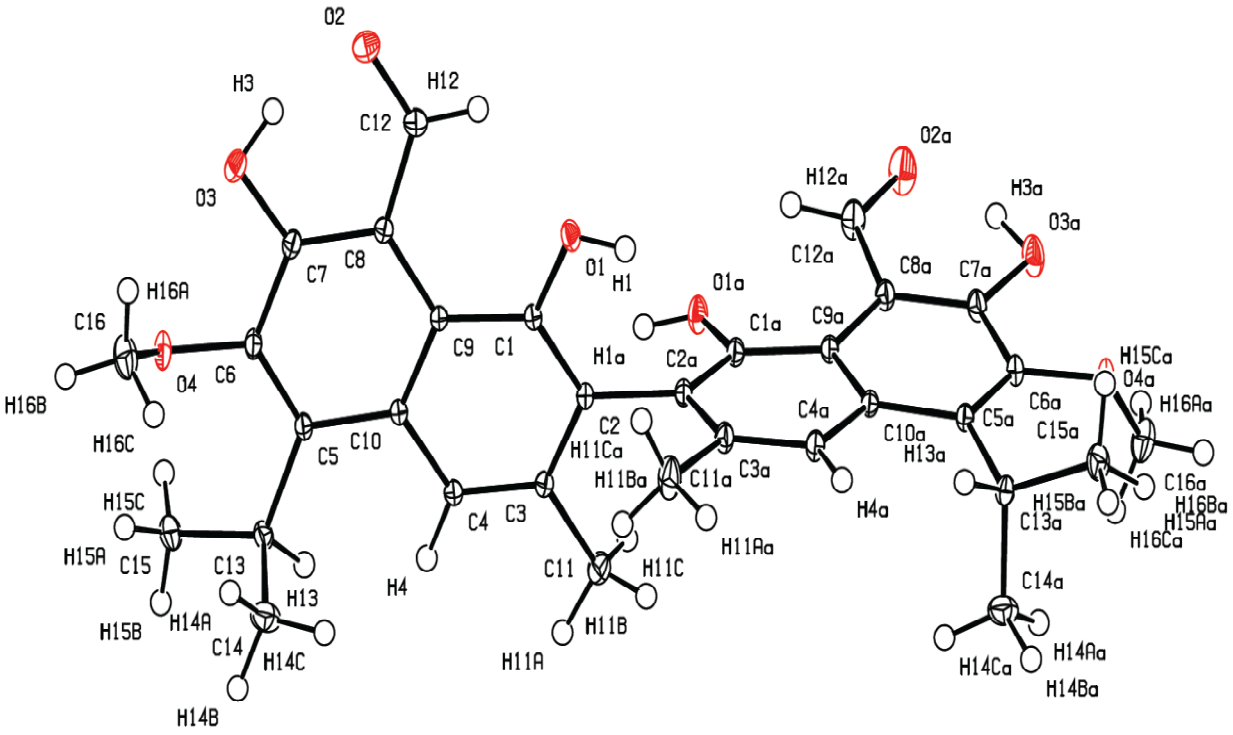

Figure 3.8 Di(methoxy)gossypol ORTEP collect at 120K.

Empirical formula	$C_{32}\ H_{34}\ O_8$	
Formula weight	546.59	
Temperature	100(2) K	
Wavelength	0.71073 Å	
Crystal system, space group	Monoclinic, C2/c	
Unit cell dimensions	a = 10.0196(2) Å	α = 90°
	b = 15.2937(3) Å	β = 96.604(2)°
	c = 17.6606(4) Å	γ = 90°
Volume / Z	2688.3(1) $Å^3$ / 4	
Density (calculated)	1.351 Mg/m^3	
Absorption coefficient	0.097 mm^{-1}	
Crystal size	0.40 x 0.45 x 0.50 mm^3	
$(\sin\theta/\lambda)_{max}$	1.18 $Å^{-1}$	
Reflections collected	99141	
Independent reflections (all data)	16099 [$R_{(int)}$ = 0.0256]	
Redundancy	6.16	
Completeness to $(\sin\theta/\lambda)_{max}$	87.3 %	
Absorption correction	Empirical (t_{min} = 0.953, t_{max} = 0.962)	

they extend outward and away from the central naphthalene structures. Generally, the naphthalene C5 carbon atom extends to the C23 carbon atom on the isopropyl group forming a covalent bond within the plane of the ring. The peripheral methyl groups position themselves all in a similar spatial arrangement where they are directed outward and anyway from the center of the molecules, which also is typically observed in gossypol crystal structures. The isopropyl groups do exhibit crowding of certain hydrogen atoms. The orientation of the H23 atom from the isopropyl group comes in close contact with the H4 atom of the naphthalene ring, limiting the angular orientation with respect to the naphthalene plane. The isopropyl group's sigma bond between the C15 atom and C28 atom, however, allows for rotation of the isopropyl group that alleviates unfavorable steric interactions. Previous crystallographic studies by Dowd and Stevens have included many examples where the isopropyl groups exhibit disorder where usually two orientations exist for these akyl groups. It is interesting to note that all of the structures reported here, no disorder was present in the isopropyl groups.

The structure of MG contains two methoxy groups located at the O4 and O8 oxygen atoms that aren't present in any of the amine gossypol derivatives. In crystallographic studies from recent research [8, 140], the methoxy groups are rotated away from the naphthalene ring plane by ~ 100-120˚, and, in this study, a similar orientation is confirmed for the MG molecule. In gossypol crystal structures, the unsubstituted hydroxyl groups usually remain in the naphthalene ring plane because of the possibility of forming intramolecular hydrogen bonds.

Hydrogen Bonding

The gossypol amine derivatives, like many other gossypol derivatives, generally form an extensive network of both intermolecular and intramolecular hydrogen bonds. All the amine derivatives contain intramolecular hydrogen bonds between the O3 oxygen atom and the N1-H atoms and between the N2-H atoms and the O7 atom. Furthermore, C22-H participates in weak hydrogen bonding to the O1 oxygen atom, and C27-H in a weak hydrogen bond to the O5 oxygen atom as well. MG forms similar intramolecular hydrogen bonds but does not have the nitrogen substituted at both the C22 and C27 carbon positions that form the aldehyde groups in gossypol and gossypol derivatives. Specifically, MG exhibits intramolecular hydrogen bonding between the O3-H hydroxyl group and the O2 carbonyl oxygen atom, and between the O7-H hydroxyl hydrogen atom and the O6 carbonyl oxygen atom. The C22-H and C27-H bonds do exhibit intramolecular hydrogen bonding to both the O1-H and the O5-H alcohol groups, respectively. In previous studies by the Dowd research group [134-135] and in the literature, instances of intermolecular hydrogen bonding involving the O3-H and O7-H hydroxyl hydrogen atoms are seldom seen. The strong intramolecular hydrogen bonding present within these functional groups seems to suggest that these intramolecular interactions are very strong. Intermolecular hydrogen bonding is also present in all the amine derivatives between the O4-H alcohol group and the O3 oxygen atoms and O8-H hydroxyl and O7 oxygen atom where both the hydrogen bonds lie in the naphthalene plane.

Intermolecular hydrogen bonds are often formed involving the O1-H and O5-H alcohol groups, and are less constrained than the hydrogen bonding that is present in the rest of the alcohol groups. In the TBAG-**S1** solid structure, the O5-H alcohol forms a intermolecular

hydrogen bond with the O9 oxygen atom located on the cyclohexanone solvate. The O1-H hydroxyl group of the ordered TPAG forms an intermolecular hydrogen bond with the O7 oxygen atom on an adjacent TPAG molecule. One of the peripheral carboxyl groups on an amino tert-butyl chain, C34-H forms an additional intermolecular hydrogen bond with the O7 oxygen atom located on a second TPAG molecule. An intermolecular hydrogen bond with a third HPAG molecule is formed between the O8-H hydroxyl group and an adjacent O5 oxygen atom.

While the TBAG-**S2** structure is comprised of di(t-butylamino)gossypol and the cyclohexanone solvate, as is the TBAG-**S1** structure, there are differences in the orientations of the hydrogen bonding. Intermolecular hydrogen bonding occurs between the O1-H group and the O7 oxygen atom. The O8-H alcohol group hydrogen bonds to an O5 atom on a second TBAG molecule. One of the methyl groups on the t-butyl group, C34-H hydrogen bonds to the O7 oxygen atom on a third TBAG molecule. Hydrogen bonding also occurs between the O5-H group and the O9 oxygen located on the cyclohexanone solvate.

Within the PAG-**S1** structure, both O1-H and O5-H are hydrogen bond donors to the O9 and O8 oxygen atoms, respectively, located on the acetone solvates. It is not surprising that both alcohol groups hydrogen bond to a relatively small polarized solvent like acetone that is easily accommodated in small pockets of crystalline solids. The O8 oxygen located on one of the solvent molecules accepts a second hydrogen bond from the C(34A)-H(34D) group on the PAG molecule. The **S1** structure contains intermolecular hydrogen bonding with two other PAG molecules within the crystalline state. The N1-H1 group hydrogen bonds with the O7 oxygen atom of an adjacent PAG molecule, and the O3-H alcohol group hydrogen bonds to the O6

oxygen atom. A second PAG molecules forms a hydrogen bond involving the O7-H(7O) group donating to the O2 oxygen atom.

With the PPAG-**P1** (ordered state) each di(3-phenylpropylamino)gossypol molecule forms hydrogen bonds with four other PPAG molecules. The O1-H group forms a intermolecular hydrogen bond with an O7 oxygen atom. Two hydrogen bonds are formed with a second PPAG molecule via the O5-H group forming an intermolecular hydrogen bond with an O3 oxygen atom, and the O4-H group donating a hydrogen bonding to the oxygen atom of an O5-H alcohol group. Intermolecular hydrogen bonding between alcohol groups also occurs with the O8-H hydroxyl group donating to the oxygen atom of the O1-H hydroxyl group of a third molecule. The amino phenyl ring participates in intramolecular hydrogen bonding between the C48-H group and the O4-H alcohol group on a fourth molecule. Similar intermolecular hydrogen bond networks are also seen in the **P2** structure. The major differences that exist in the disordered **P2** structures when compared to the **P1** structure are the lengths of the hydrogen bonds.

The HPAG-**S1** structure exhibits the greatest number of combined intra and intermolecular hydrogen bonding. The O1-H hydroxyl group forms a hydrogen bond to the O40 oxygen atom of the keto-group located on one of the acetone solvent molecules. Analogously, the O5-H hydroxyl group forms a hydrogen bond to the O50 oxygen atom of the second acetone molecule of the unit cell. The O2-H alcohol group located on the amine R-group, forms an intermolecular hydrogen bond to the O40 oxygen atom located on the first acetone molecule. On careful inspection, the O6-H hydroxyl group on the second amine chain donates a variable hydrogen bond depending on which disordered state the amino side chain is in: the major component(A) occupancy or the minor component(B) occupancy. In the major component (A),

the O6-H hydroxyl atoms hydrogen bonds to the O60 oxygen atom on the water molecule. The O6-H alcohol group, in the minor component, also donates an intermolecular hydrogen bond to the O2 oxygen atom located on the adjacent HPAG molecule. The di(3-hydroxypropylamino) gossypol crystalline structure also exhibits intermolecular hydrogen bond donation between O60-H of a water molecule and the O40 oxygen atom located on the acetone solvate. The HPAG molecule forms hydrogen bonds with three other HPAG molecules via the following bonds: O4-H donating to an O7 oxygen atom; O6B-H donating to an O2 oxygen atom; and O8-H donating to the O3 oxygen atom.

Di(propylamino)gossypol, like many of the amine gossypol derivatives, forms intermolecular hydrogen bonds with three other di(propylamino)gossypol molecules in the crystalline state. On one naphthalene ring, both alcohol groups, O1-H and O3-H donate hydrogen bonds to the O5 and O2 oxygen atoms respectively, on two differing PAG molecules. A third molecule is hydrogen bonded via the C26-H methyl group donating to the O3 alcohol group. The O4-H alcohol group, interestingly, doesn't participate in any hydrogen bonding.

Electron density distribution and topological analysis

A contour plot of the static model deformation density of both di(propylamino) gossypol and dimethoxy gossypol are shown in figures 3.9 and 3.10. As expected, the deformation density maps of MG and PAG display an increase in electron density in all the covalent bonds relative to neutral, non-interacting spherical atoms. Further accumulation of electron density is observed near oxygen atoms comprising the alcohol and ketone groups in MG and PAG

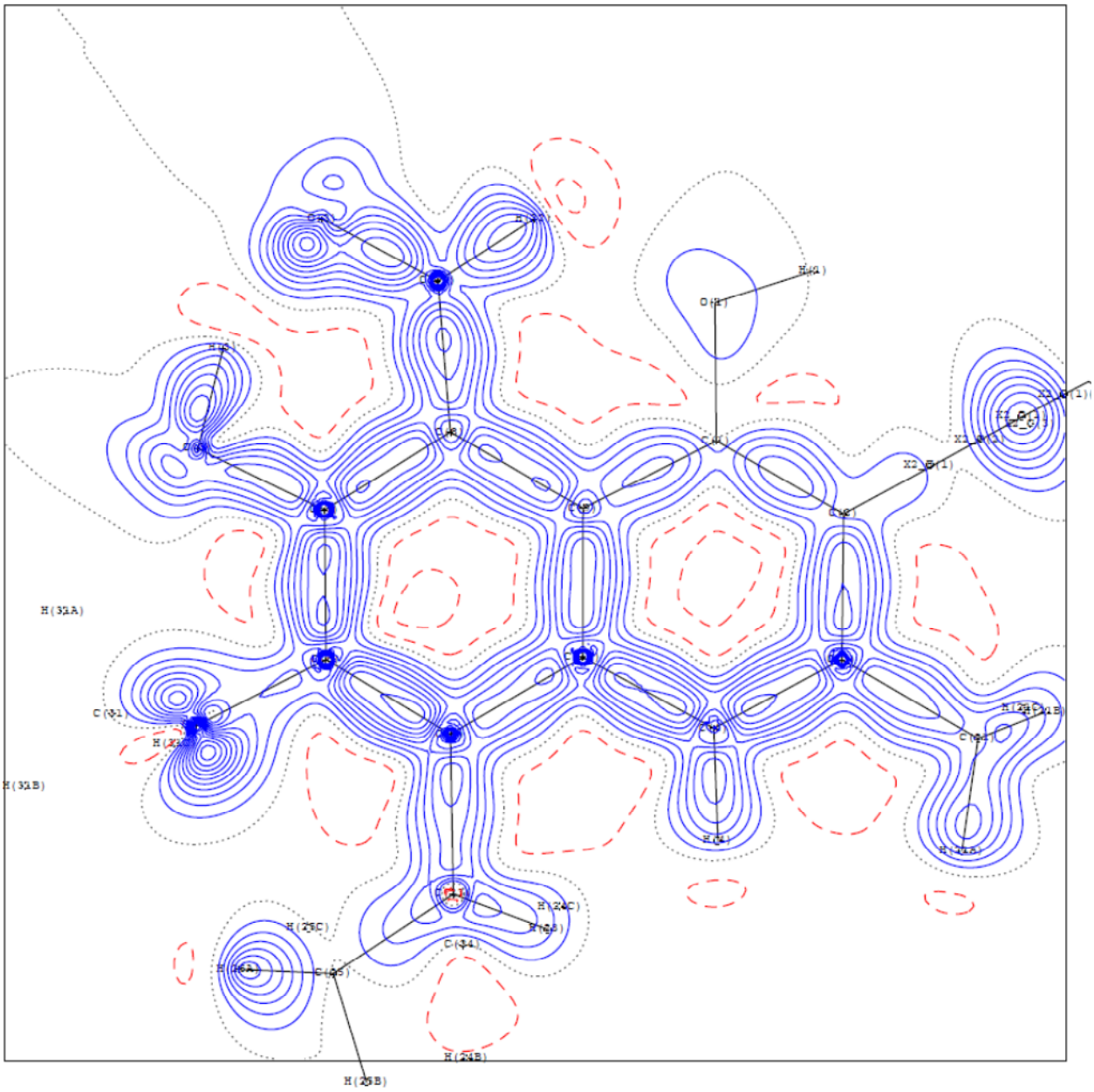

Figure 3.9 Experimental static deformation density map of one half of di(methoxy)gossypol (MG) in the naphthalene plane. Contours are plotted at 0.1 e $Å^{-3}$ intervals with positive contours represented by solid (blue) lines, negative countours by dashed (red) lines, and the zero contour by dotted (black) lines.

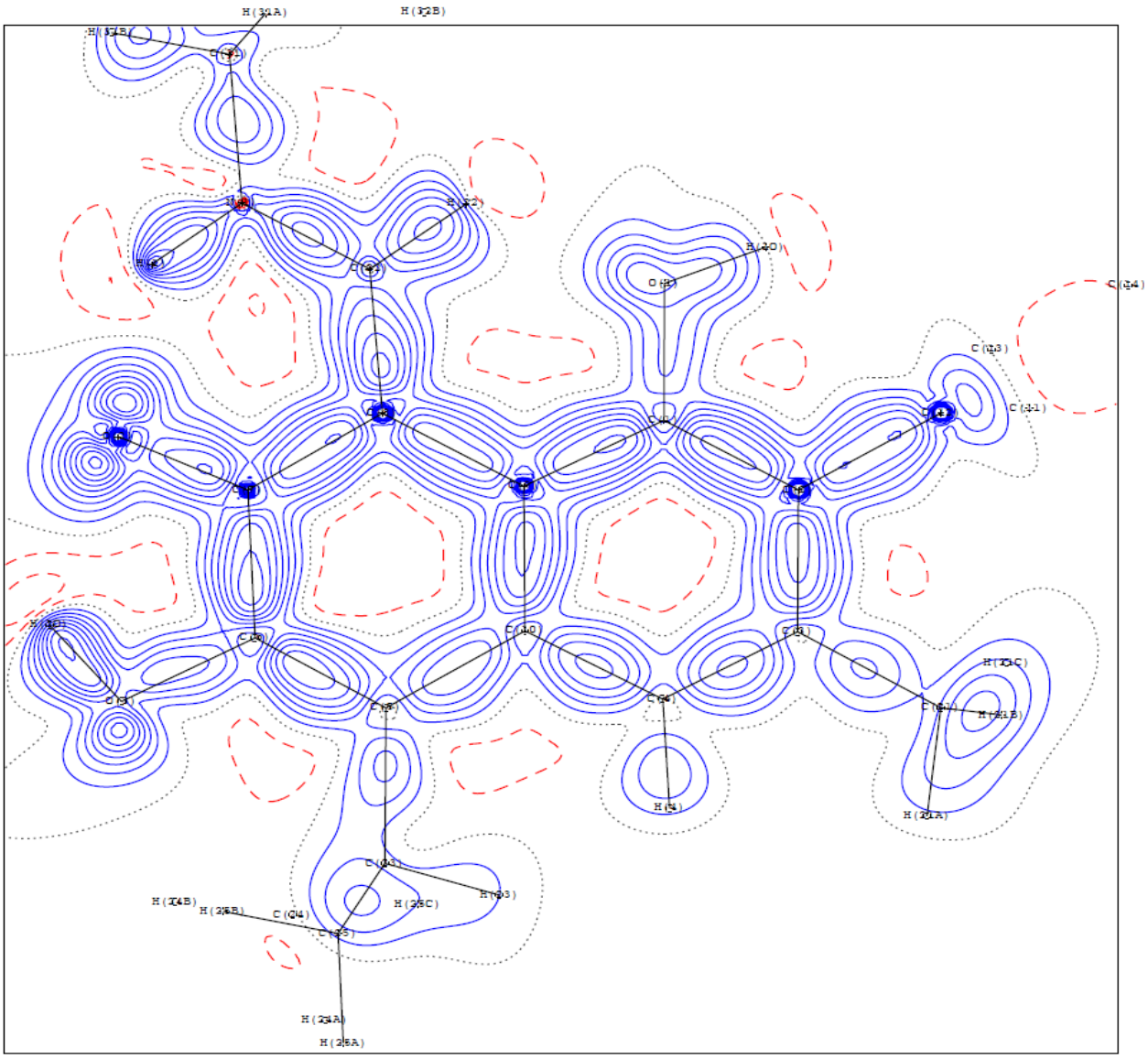

Figure 3.10 Experimental static deformation density map of one half of di(propylamino) gossypol within the naphthalene plane. Contours are plotted at 0.1 e $Å^{-3}$ intervals with positive contours represented by solid (blue) lines, negative countours by dashed (red) lines, and the zero contour by dotted (black) lines.

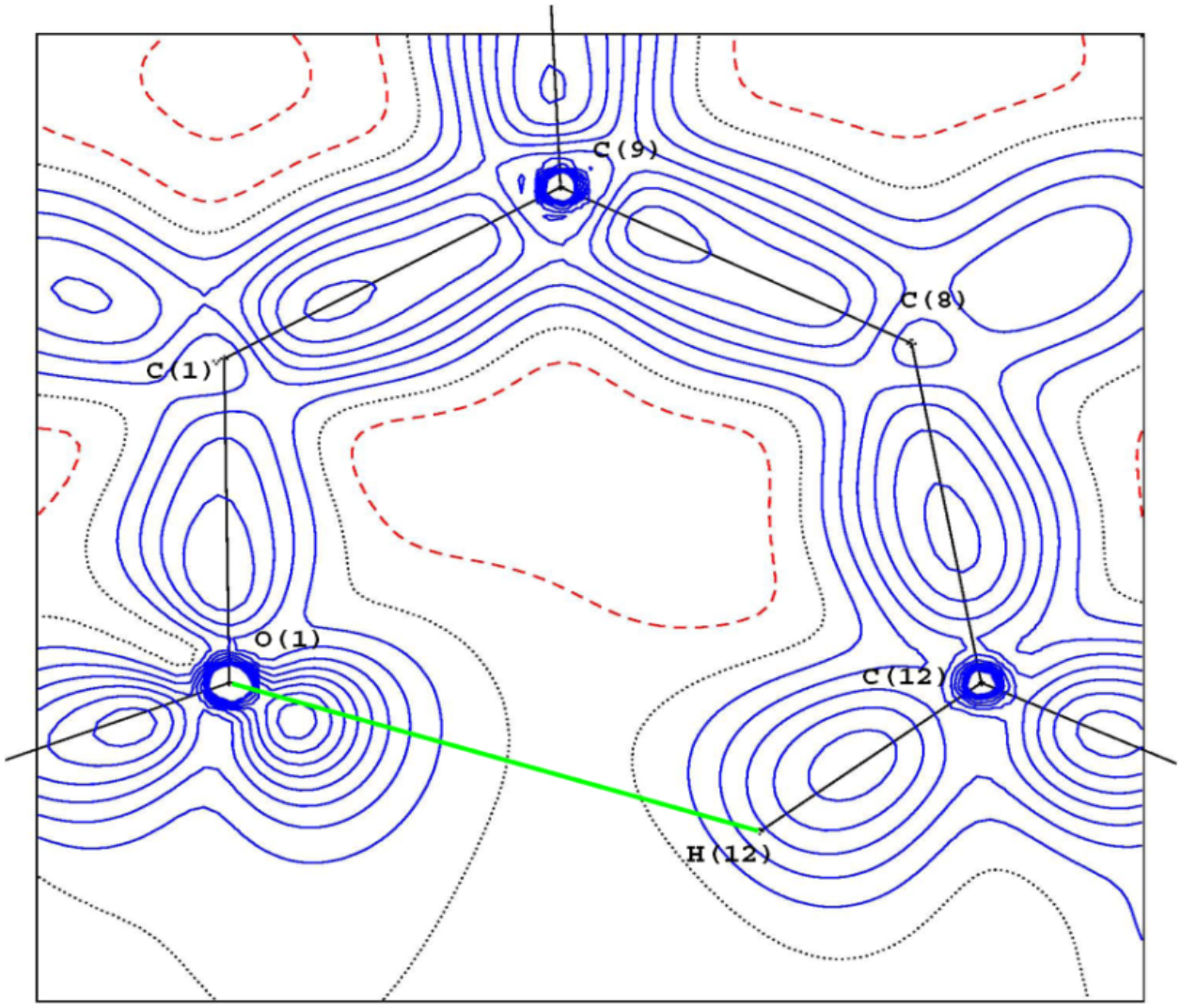

Figure 3.11 Plot of the static multipole model density of 6,6'-dimethoxygossypol in the plane of the C(22)-H(22) . . . O(1) intramolecular hydrogen bond. Contours are plotted at 0.10 e $Å^{-3}$ intervals, with negative contours dashed (red), positive contours solid (blue), and the zero contour dotted (black).

associated with lone pair electrons. Specifically, additional electron density is observed in the bridging oxygens of the methoxy groups in MG, and in PAG the anionic oxygen atoms display excess electron density, not only due to lone pairs, but also because of the accumulation of additional negative charge.

Interestingly, the static deformation density reveals details in the electron distribution of the intramolecular hydrogen bonds in MG and PAG. For example, the static deformation density of C22-H22 donating a hydrogen bond to the O1 oxygen atom is shown in fig. 3.11. A second intramolecular hydrogen bond is shown in MG is shown in figure 3.12 where hydrogen bond donation occurs from O3-H3 to the O2 atom located on the aldehyde group at the C8 ring position. In PAG, the static deformation density can also be viewed in the intramolecular hydrogen bond as well. In figures figure 3.13 and figure 3.14 are mappings of the intramolecular hydrogen bonding between the lone O3 oxygen atom and the O3-H3 bond.

When comparing the charge densities of the central naphthalene rings of PAG and MG only small differences are observed (numerical values given in Tables 1 and 2). Similar electron density trends are observed in the corresponding carbon-carbon bonds of the naphthalene rings of MG and PAG. For instance, the C5-C6 bond exhibits the largest deformation density of the ring bonds in both MG and PAG. Neither the amine alkyl group in PAG nor the additional methylation in MG appear to alter the ring structure sufficiently to yield major differences in the electronic conjugation of the aromatic rings such that large differences in the deformation density are observed. The greatest differences in density between corresponding bonds in MG and PAG are present in the carbon-hydrogen bonds at the C24, C25, C29, and C30 positions.

In both PAG and MG, BCPs are observed in both the theoretical and experimental densities for all O-H hydrogen bonds; C-C covalent bonds; C-O; and C-H bonds, and have

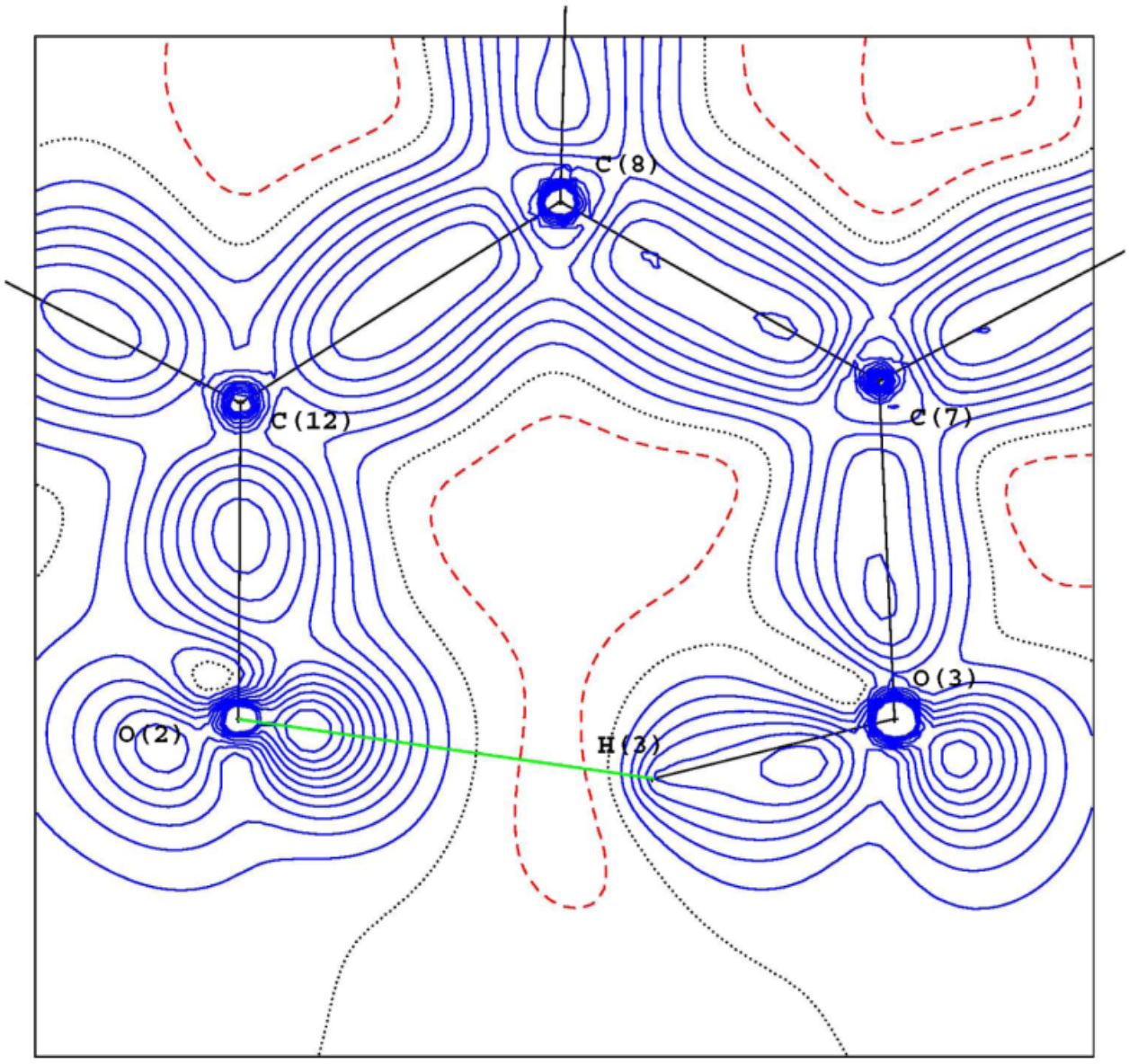

Figure 3.12 Plot of the static multipole model density of 6,6'-dimethoxygossypol in the plane of the O(3)-H(3) . . . O(2) intramolecular hydrogen bond. Contours are plotted at 0.10 e $Å^{-3}$ intervals, with negative contours dashed (red), positive contours solid (blue), and the zero contour dotted (black).

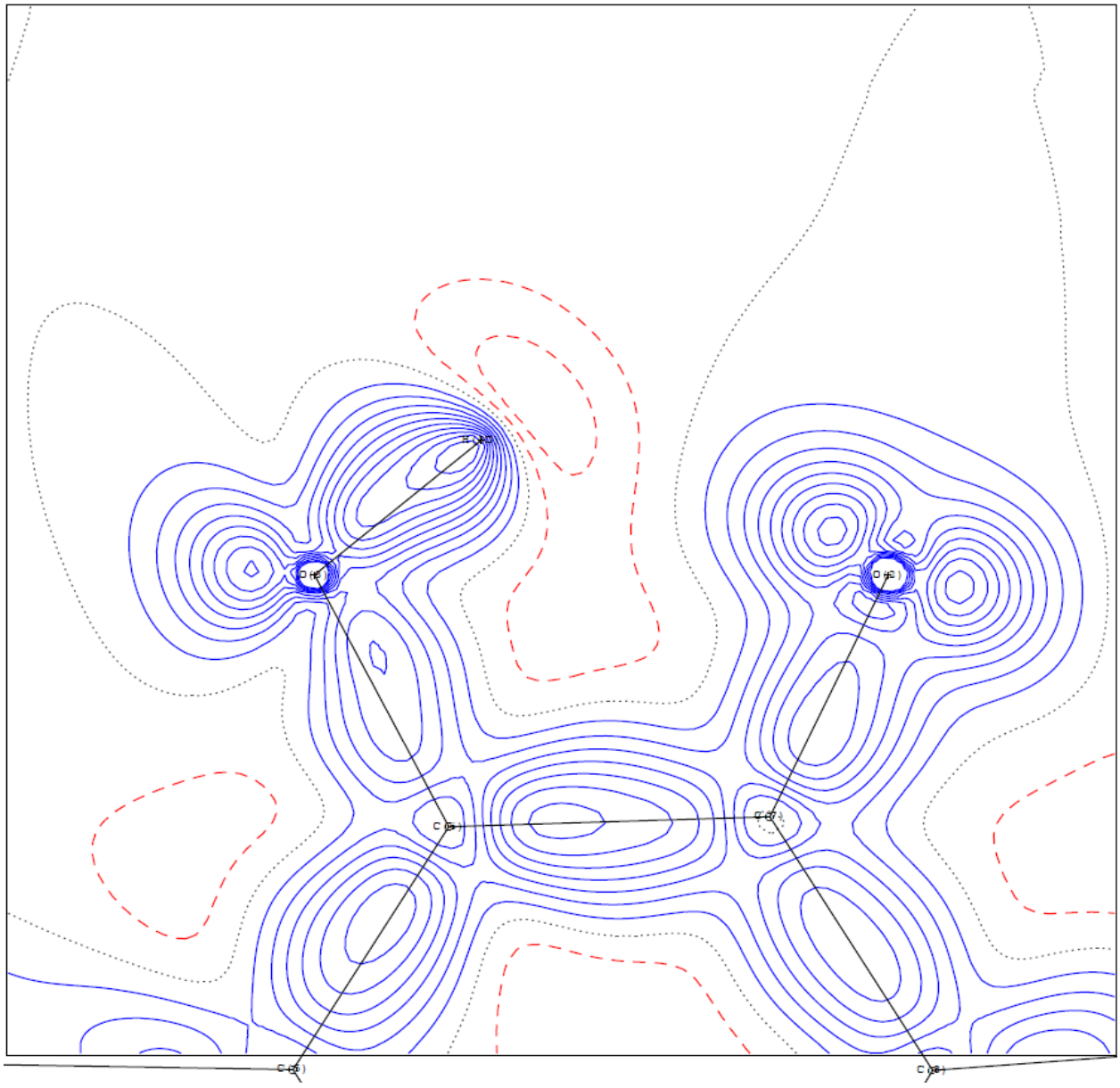

Figure 3.13 Plot of the static multipole model density of di(propylamino)gossypol in the plane of the O(3)-H(3)0 . . . O(2) intramolecular hydrogen bond. Contours are plotted at 0.10 e $Å^{-3}$ intervals, with negative contours dashed (red), positive contours solid (blue), and the zero contour dotted (black).

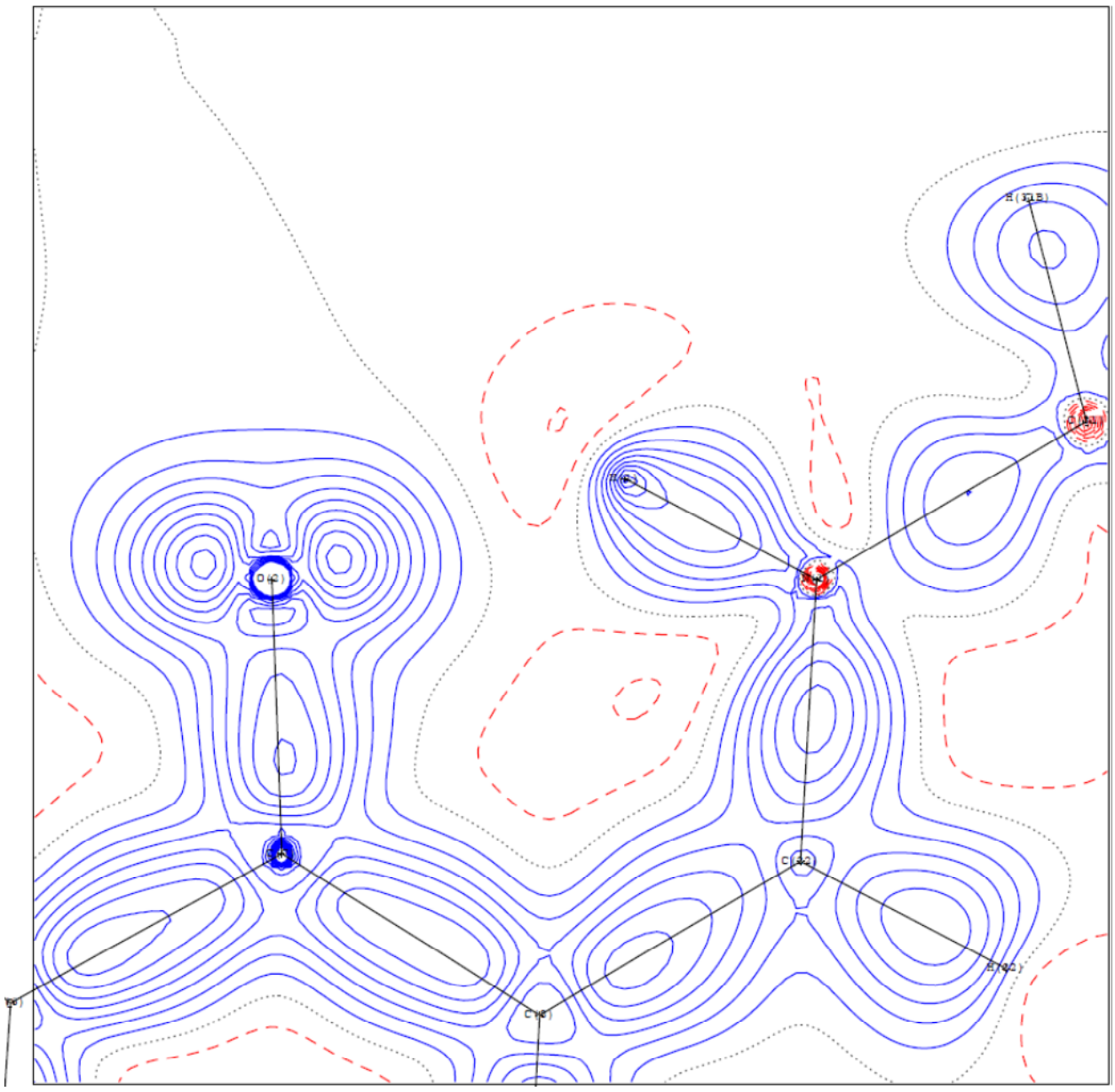

Figure 3.14 Plot of the static multipole model density of di(propylamino)gossypol in the plane of the N(1)-H(1) . . . O(2) intramolecular hydrogen bond. Contours are plotted at 0.10 e $Å^{-3}$ intervals, with negative contours dashed (red), positive contours solid (blue), and the zero contour dotted.

experimental densities that are consistent with the literature. The Laplacians and ellipticities for PAG and DMG are listed in table X and conform to reasonable expectations.

Atomic charges and volumes

In Bader's AIM theory, the total electron density encompassing a molecule is partitioned into individual atom densities by finding the surfaces between neighboring atoms defined by gradient trajectories which terminate at the BCPs. These particular surfaces, as well as the exterior surface of 0.001 e/a.u. (0.00675 $e\text{Å}^{-3}$), generate quite irregular shapes that nevertheless logically and consistently define individual atomic volumes. This systemization of defining individual atomic density within molecules naturally allows for the determination of atomic charge contained in each atomic basin. However the volumes encountered within the zero-flux surface give atypical shapes that can be particular difficult to integrate, and the volume and charges calculated have not been shown to be useful in general empirical force fields.

Electrostatic Potential

Another analysis that can be done with charge density studies entails the electrostatic potential of a molecule which is the potential that a unit positive charge would experience at any point surrounding a molecule due to the electron density distribution and distribution of nuclear charges within the molecule. Consequently, the electrostatic potential expresses features predictive of chemical reactivity because regions of negative potential are expected to be sites of protonation and nucleophilic attack. Conversely, regions of positive potential may be indicative

of electrophilic regions. The electrostatic potential of both di(methoxy) gossypol and di(propylamino) gossypol have been calculated from the experimental electron density distribution by the method of Su and Coppens [145] as implemented in XD2006 (fig 3.15 & fig. 3.16). The electrostatic potential are plotted on the isoelectron-density surface at $\rho(r) = 0.50$ e $Å^{-3}$ and coded with a color corresponding to the value of the potential using the program MOL-ISO [146]. As anticipated, strong negative potentials are observed around highly electronegative atoms like oxygen atoms, and positive regions are observed near all hydrogen atoms.

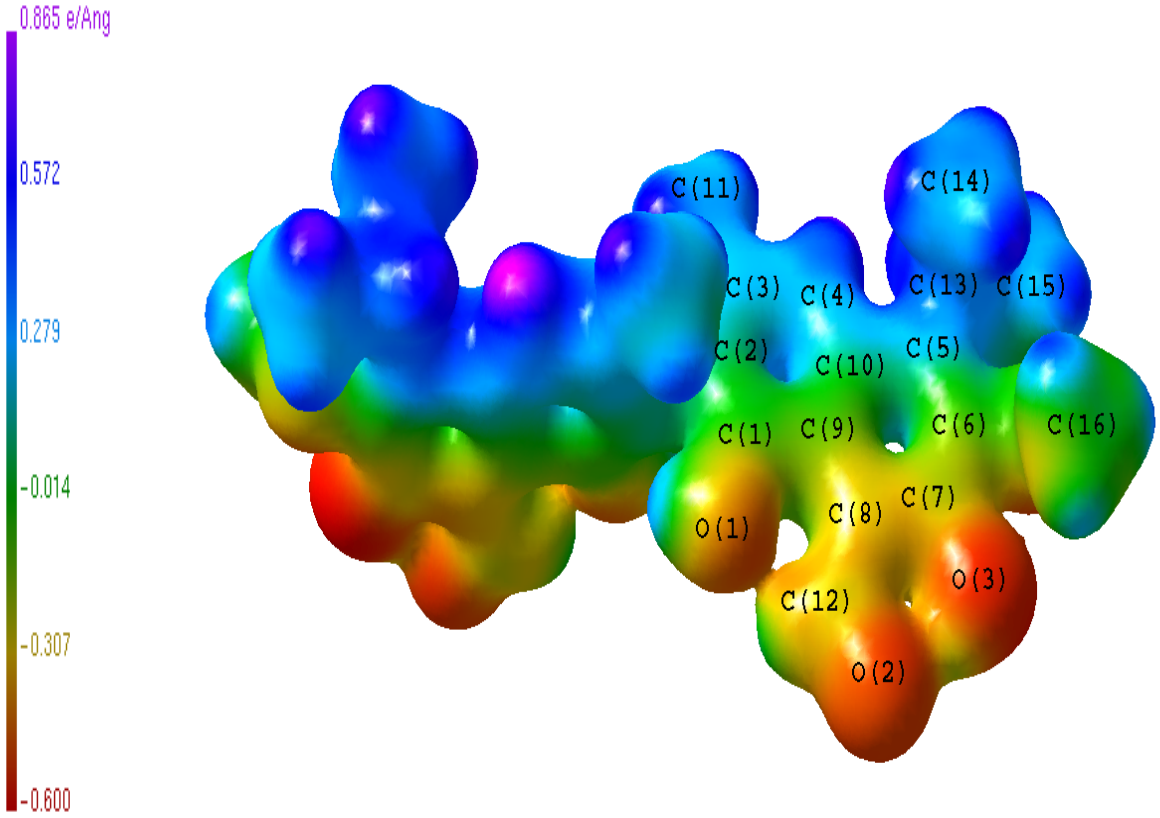

Figure 3.15 Experimental electrostatic potential of 6,6'-dimethoxygossypol plotted on the molecular surface. The value of the potential is color coded using the scale shown on the left.

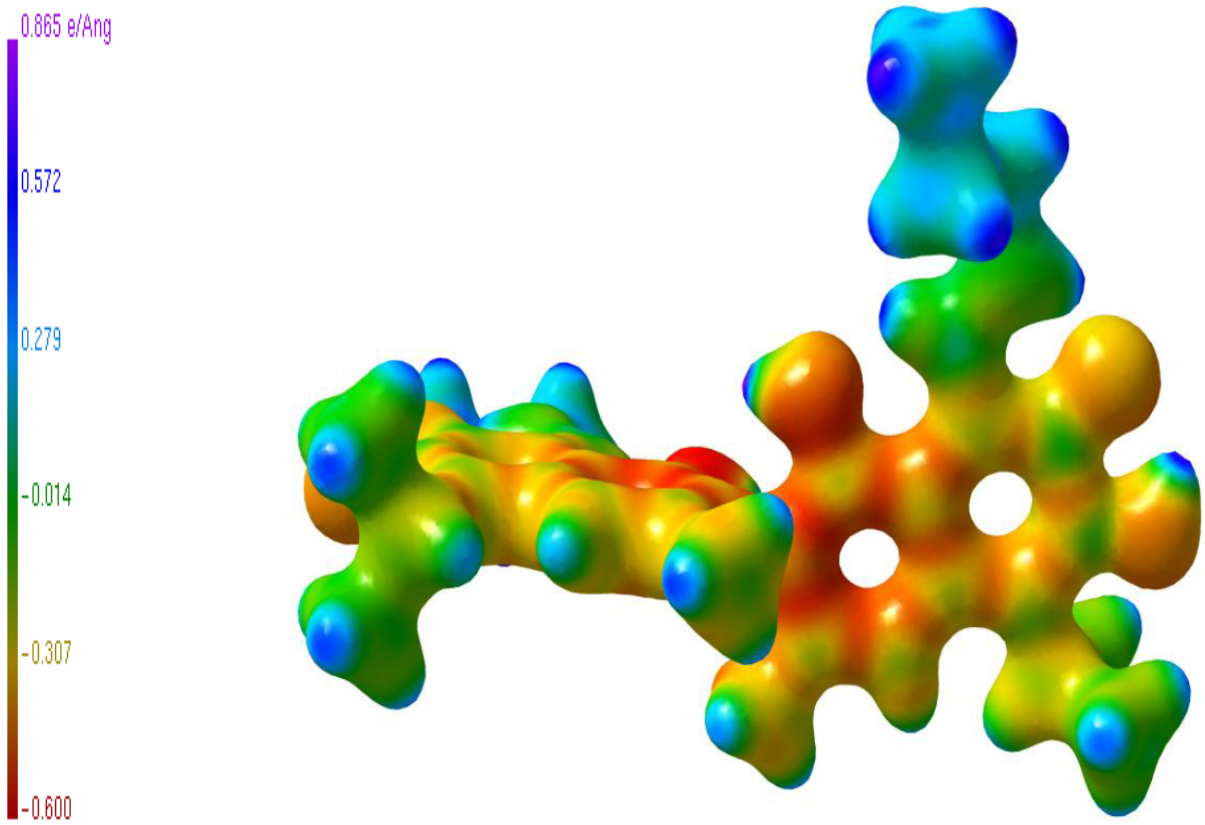

Figure 3.16 Experimental electrostatic potential of di(propylamino)gossypol plotted on the molecular surface. The value of the potential is color coded using the scale shown on the left.

		Table 1		
Dimethylgossypol Bond Critical Points				
	DMG	DMG	DMG	DMG
	$\rho(r_b)(eA^{-3})$	$\nabla\rho(r_b)(eÅ^{-5})$	ε	λ_3
C(1)-C(2)	2.274(1)	-19.52(3)	0.34	12.91
C(1)-C(9)	1.994(1)	-13.94(3)	0.26	13.31
C(2)-C(3)	2.091(1)	-15.56(2)	0.23	13.29
C(3)-C(4)	2.232(1)	-19.07(3)	0.20	12.51
C(4)-C(10)	2.144(1)	-17.48(3)	0.26	13.06
C(5)-C(6)	2.342(1)	-21.48(3)	0.32	12.43
C(5)-C(10)	1.902(1)	-12.41(3)	0.14	13.34
C(6)-C(7)	2.102(1)	-16.23(3)	0.27	13.25
C(7)-C(8)	2.146(1)	-16.15(3)	0.22	13.26
C(8)-C(9)	2.006(1)	-12.97(2)	0.27	13.93
C(9)-C(10)	2.100(1)	-16.44(2)	0.18	13.24
C(1)-O(1)	2.167(1)	-16.59(5)	0.17	17.18
C(2)-C(2')	1.670(1)	-8.17(3)	0.02	13.54
C(3)-C(21)	1.839(1)	-13.77(2)	0.12	11.72
C(5)-C(23)	1.676(1)	-10.79(2)	0.14	12.05
C(6)-O(4)	2.010(1)	-10.50(5)	0.08	18.92
C(7)-O(3)	2.407(2)	-20.44(5)	0.24	12.12
C(8)-C(22)	2.053(1)	-16.50(3)	0.18	11.63
C(22)-O(2)	2.837(3)	-18.67(9)	0.09	28.54
C(23)-C(24)	1.666(1)	-10.73(2)	0.03	11.17
C(23)-C(25)	1.607(1)	-8.80(2)	0.02	11.46
C(31)-O(4)	1.889(1)	-11.90(3)	0.09	17.25
O(1)-H(1)	2.136(1)	-41.27(8)	0.03	29.81
O(3)-H(3)	2.134(1)	-37.87(9)	0.05	32.15
C(4)-H(4)	1.839(1)	-20.246(5)	0.08	15.52
C(21)-H(21A)	1.952(1)	-19.90(3)	0.13	13.69
C(21)-H(21B)	1.939(1)	-19.52(3)	0.10	13.75
C(21)-H(21C)	1.947(1)	-19.63(3)	0.11	13.74
C(23)-H(23)	1.964(1)	-20.61(4)	0.10	13.48
C(24)-H(24A)	1.969(1)	-21.02(3)	0.02	13.16
C(24)-H(24B)	1.978(1)	-20.99(3)	0.02	13.18
C(24)-H(24C)	1.971(1)	-20.94(3)	0.02	13.19
C(25)-H(25A)	1.960(1)	-20.30(3)	0.07	13.52
C(25)-H(25B)	1.952(1)	-20.11(3)	0.06	13.55
C(25)-H(25C)	1.960(1)	-20.38(3)	0.07	13.47
C(31)-H(31A)	1.968(1)	-20.10(3)	0.16	13.64
C(31)-H(31B)	1.955(1)	-19.72(1)	0.16	13.77
C(31)-H(31C)	1.955(1)	-19.85(3)	0.17	13.67
Table Continued				

O(1)-H(1) . . . O(4)	0.106(3)	2.32(2)	0.03	3.37
O(3)-H(3) . . . O(2)	0.434(8)	5.64(2)	0.08	12.12
C(4)-H(4) . . . O(2)	0.039(2)	0.98(1)	0.27	1.34
C(22)-H(22) . . . O(1)	0.143(4)	2.68(3)	0.41	4.14
C(25)-H(25C) . . . O(1)	0.033(1)	0.70(1)	1.27	0.94
C(31)-H(31A) . . . O(3)	0.068(1)	1.56(1)	0.14	2.14

Table 2			Di(propylamino)gossypol			
Bond		$\rho(r_b)$ (eA^{-3})		$\nabla \rho(r_b)$ ($eÅ^{-5}$)		ε
O1-C1		2.187(1)		-14.45(8)		0.17
O1-H10		2.606(2)		-56.78(1)		0.1
O2-C7		2.696(2)		-27.47(1)		0.01
O3-C6		2.265(1)		-19.79(1)		0.06
O3-H30		2.271(1)		-50.59(9)		0.07
O4-C11		2.214(1)		-14.93(1)		0.04
O4-H4O		2.851(3)		-46.76(9)		0.03
O5-C17		2.653(2)		-26.33(1)		0.01
O6-C16		2.250(1)		-19.09(1)		0.06
O6-H60		2.656(2)		-49.67(1)		0.07
N1-C22		2.472(2)		-26.45(1)		0.1
N1-C31		1.863(1)		-12.09(1)		0.07
N1-H1		2.161(1)		-25.90(3)		0.06
N2-C27		2.486(1)		-26.61(1)		0.09
N2-C34		1.864(1)		-12.24(1)		0.06
N2-H2		2.160(1)		-25.86(1)		0.06
C1-C2		2.222(1)		-17.83(1)		0.26
C1-C9		2.123(1)		-16.32(1)		0.17
C2-C3		2.144(1)		-15.66(1)		0.17
C2-C12		1.856(1)		-11.52(1)		0.02
C3-C4		2.318(1)		-20.00(1)		0.14
C3-C21		1.837(1)		-13.84(1)		0.08
C4-C10		2.177(1)		-18.34(1)		0.18
C4-H4		1.953(1)		-22.77(1)		0.12
C5-C6		2.324(1)		-20.37(1)		0.21
C5-C10		1.969(1)		-13.34(1)		0.13
C5-C23		1.608(1)		-8.00(1)		0.18
C6-C7		2.089(1)		-16.25(1)		0.24
C7-C8		2.103(1)		-16.95(1)		0.16
C8-C9		1.975(1)		-13.32(1)		0.19
C8-C22		2.071(1)		-15.09(1)		0.15
C9-C10		2.066(1)		-15.63(1)		0.18
C11-C12		2.240(1)		-18.23(1)		0.26
C11-C19		2.128(1)		-16.41(1)		0.17
C12-C13		2.151(1)		-15.79(1)		0.17
C13-C14		2.321(2)		-20.14(1)		0.14
C13-C26		1.836(1)		-13.80(1)		0.08
C14-C20		2.172(1)		-18.18(1)		0.18
C14-H14		1.956(1)		-22.86(1)		0.12
C15-C16		2.328(2)		-20.42(1)		0.21
C15-C20		1.984(1)		-13.64(1)		0.13
C15-C28		1.611(1)		-6.97(1)		0.19
C16-C17		2.113(1)		-16.75(1)		0.24
C17-C18		2.113(1)		-17.16(1)		0.15
C18-C19		1.982(1)		-13.47(1)		0.19
C18-C27		2.047(1)	Table Continued	-14.57(1)		0.14

C19-C20		2.051(1)		-15.32(1)		0.18
C21-H21C		1.718(1)		-16.99(1)		0.15
C21-H21B		1.727(1)		-16.92(1)		0.15
C21-H21A		1.729(1)		-17.14(1)		0.17
C22-H22		1.854(1)		-23.74(1)		0.05
C23-C24		1.687(1)		-10.32(1)		0.07
C23-C25		1.718(1)		-10.81(1)		0.07
C23-H23		1.630(1)		-10.76(1)		0.11
C24-H24C		1.778(1)		-19.58(1)		0.09
C24-H24B		1.774(1)		-19.63(1)		0.09
C24-H24A		1.778(1)		-19.59(1)		0.09
C25-H25C		1.775(1)		-19.62(1)		0.09
C25-H25B		1.773(1)		-19.60(1)		0.1
C25-H25A		1.787(1)		-19.73(1)		0.09
C26-H26C		1.688(1)		-15.97(1)		0.19
C26-H26B		1.703(1)		-16.32(1)		0.18
C26-H26A		1.699(1)		-16.10(1)		0.18
C27-H27		1.851(1)		-23.68(1)		0.05
C28-C29		1.695(1)		-10.90(1)		0.07
C28-C30		1.634(1)		-9.46(1)		0.12
C28-H28		1.591(1)		-10.07(1)		0.08
C29-H29C		1.784(1)		-19.70(1)		0.09
C29-H29B		1.773(1)		-19.52(1)		0.09
C29-H29A		1.780(1)		-19.67(1)		0.09
C30-H30C		1.779(1)		-19.55(1)		0.09
C30-H30B		1.778(1)		-19.69(1)		0.09
C30-H30A		1.783(1)		-19.70(1)		0.1
C31-C32		1.729(1)		-13.48(1)		0.09
C31-H31B		1.674(1)		-15.57(1)		0.15
C31-H31A		1.674(1)		-15.80(1)		0.15
C32-C33		1.606(1)		-11.31(1)		0.08
C32-H32B		1.688(1)		-15.89(1)		0.14
C32-H32A		1.690(1)		-15.84(1)		0.14
C33-H33C		1.771(1)		-19.45(1)		0.07
C33-H33B		1.783(1)		-19.81(1)		0.06
C33-H33A		1.771(1)		-19.78(1)		0.06
C34-C35		1.720(1)		-13.26(1)		0.09
C34-H34B		1.679(1)		-15.73(1)		0.15
C34-H34A		1.684(1)		-15.90(1)		0.15
C35-C36		1.618(1)		-11.71(1)		0.08
C35-H35B		1.696(1)		-15.89(1)		0.14
C35-H35A		1.692(1)		-15.88(1)		0.14
C36-H36C		1.760(1)		-19.38(1)		0.07
C36-H36B		1.778(1)		-19.61(1)		0.07
C36-H36A		1.779(1)		-19.80(1)		0.06

Discussion

The number of solvates that gossypol can form is extensive, which includes organic molecules, such as esters, alcohols, nitriles, carboxylic acids, nitro compounds, ketones, ethers, and a multitude of simple and complex aromatic compounds [30]. Gossypol also forms solvates with compounds that are chlorinated or brominated. Despite gossypol's ability to form an array of solvates, its chemical and crystalline structure does limit the possibilities of guest molecules. Gossypol's central molecular framework consist of two planer naphthalene rings that are interconnected by a bridged bond that allows for each ring to be oriented with an interplaner angle of approximately 70-110°. The constrained and limited rotational range of gossypol's naphthalene planes restricts its ability to achieve optimal packing. Gossypol's alcohol and aldehyde groups, on the other hand, provide numerous hydrogen bond donor and acceptor groups that provide for an assortment of possibilities in intermolecular hydrogen bonding. The geometric orientations of the hydrogen bonds, to a certain degree, are flexible and further add to the possible crystalline states that gossypol has the potential to accommodate. Moreover, gossypol's polar functional groups residing on approximately one half of each naphthalene ring and aliphatic groups which reside on the other half of the rings create hydrophilic and hydrophobic domains on the molecule itself. In many instances, the assembly of these hydrophobic and hydrophilic regions creates a unique way neighboring gossypol molecules position themselves creating channels and/or cavities of alternating degrees of hydrophobicity or hydrophilicity. The above-mentioned features provide the basis for understanding how gossypol molecules can accommodate various categories of guest molecules based on charge, topology, and size. As a consequence, gossypol has the ability to make a diverse arrangement of packing

motifs in the crystalline solid state. The number of possible polymorphic and inclusion complexes appears to be only limited by the amount of time and energy one is willing to invest in growing crystals. The McCrone statement holds steadfast for gossypol that "the number of forms known for a given compound is proportional to the time and energy spent in research on that compound."[147]

MG contains two methyl groups in place of the hydrogen atoms at the 6 and 6' hydroxyl positions. Methylation decreases the number of alcohol groups that are able to contribute to intramolecular and intermolecular bonding. Since the methoxy groups orient themselves out of the extended naphthalene plane, it allows for the possibility that adjacent MG molecules may pack in a more compact geometry without solvent. For that reason, one would assume that the packing of MG molecules would be more restrictive and diminish its ability to form diverse packing motifs when compared to gossypol crystals. Furthermore, these restrictions would decrease the number of solvates that MG could accommodate into its crystal lattice. Literature reports and our data supports the idea that MG is limited in its ability to form solvates, since no solvates are formed with pentan-2-one, diethyl ether, chloroform, and acetone under the same experimental conditions that gossypol readily forms solvates. Despite the methoxy groups that differentiate MG from gossypol, MG still retains a majority of the bonding characteristics of gossypol including the presence of hydrophobic and hydrophilic groups existing on the opposing planes of the naphthalene rings, the perpendicular orientation of the naphthalene rings, the planer geometry of the naphthalene rings, and the presence of aldehyde groups. The preservation of these key features in MG, infers that it should still have the capacity to form some solvates, and the observation that MG has formed solvates with cyclohexanone, water, and acetic acid confirm

this assumption. While the Dowd research group has been able to confirm a variety of solvates and inclusion complexes with MG, in this particular study, MG was not solvated.

One interesting observation of MG crystalline solids by Dowd and Stevens is that MG clathrates tend to promote some arrangement of disorder. In previous published research, four MG crystal structures were reported where two of the structures were polymorphs of MG with no disorder. As well as having no disorder, one of the MG polymorphs contained internal symmetry where the symmetry element was located at the center bond between the naphthalene rings. The two solvated forms of MG presented in the study contained disorder not only in the isopropyl group but disorder in one of the solvent molecules as well.

All the amine derivatives presented in this research substitute the oxygen atoms located on both aldehyde groups with nitrogen atoms. While this substitution eliminates the highly electronegative oxygen from accepting hydrogen bonding, the nitrogen atom is bonded to a hydrogen allowing it to act as a hydrogen bond donor. All of the gossypol amine derivatives (G-NHR_1: G is the parent gossypol molecule) amine alkyl R_1 groups are aliphatic or aromatic with no electronegative functional groups with the exception of the HPAG-**S1** structure. Like MG, all the amine derivatives have adjacent alcohol functional groups that are stripped of hydrogen atoms leaving C-O^- oxygen anions at these particular positions. As a result, the hydrogen bonding donor potential at these oxygen positions is replaced with a strong hydrogen bonding acceptor potential due to the formal anionic oxygen atoms. In all the gossypol amine derivatives presented, the anionic oxygen atoms on each naphthalene ring are all hydrogen bond acceptors. The anionic oxygen atoms in many instances accept more than one hydrogen bond. The $O3^-$ atoms in the HPAG-**S1** molecule, functioning as a strong nucleophile, accepts 3 hydrogen bonds: one from the neighboring NH bond; one from the adjacent O4H hydroxyl group; and one from

the O8H alcohol group of an adjacent HPAG-**S1** molecule. Despite the limited geometry of the orientation of the anionic oxygen atoms on the naphthalene ring, and naturally the shortened length of the C-O^- bond when compared to the C-OH bond, the anionic oxygen atom still participates with both inter and intramolecular hydrogen bonding that is indicative of the strength of its nucleophilicity.

As observed in the previous research by Dowd and Stevens on gossypol, gossypol derivatives, and MG, disorder is present in many crystallographic studies, even in cases where diffraction data is collected at low temperature [8, 134-135]. Specifically, the isopropyl groups often exhibit disorder on one or both rings. It is interesting to note that no disorder is present in the isopropyl groups on any of the seven amine gossypol derivatives presented. If this trend continues to be observed in future studies on amine derivatives, it may be reasonable to conclude that substituting the aldehyde groups with amine alkyl group may be responsible for the diminished disorder. When comparing disorder on the substituted amino alkyl chains between various gossypol derivatives, not only is disorder present in some cases, but is absent in systems that are very similar. The PPAG-**P1** and PPAG-**P2** structures come from the same series of experimental procedures and have similar unit cell volumes and dimensions; similar intra and inter molecular bond orientations; and unit cell symmetry operations. One of the major factors that may have contributed to the disorder present with the **P2** system is that the data collection was at room temperature. Within both PAG structure solutions, disorder is only present within the PAG-**S1** structure. Both the PAG-**S1** and PAG diffraction data were collected at low temperatures and incorporated acetone and ethanol molecules, respectively, while only the PAG-**S1** was solvated. The major differences between both structures in each PAG experiment are the solvent molecules. The PAG structure is not solvated and contains no disorder. In the PAG-**S1**

study, interestingly the solvated acetone contributes through only one of the disordered states by accepting a hydrogen bond via a C34A-H34D bond. The crystals recovered for TBAG-**S1** and TBAG-**S2** came from the same series of coupled experiments and both diffraction and experimental conditions were identical in the data collection. Despite the similarities, and low R_1 values in both cases ($R_1 \leq 5.2\%$), TBAG-**S2** contained a disordered cyclohexanone solvate that was not present in TBAG-**S1**. When performing a number of the crystallographic studies presented here, in many instances, crystal specimens were not suitable for a number of reasons ranging from poor crystal diffraction, cracking due to abrupt changes in temperature, or parasitic crystal growth on the parent crystal which required retrieval of another specimen from the mother liquor. In each case for this study, when a second or third crystal was isolated from the same vial(s), virtually the identical diffraction data was collected that naturally gave identical structure solutions. Ascertaining any contributing factors that may have caused the disorder with TBAG-**S2** becomes more difficult to comprehend because minute differences are commonly more difficult to evaluate. When examining the differences within the unit cells, hydrogen bonding networks, and other considerations, it becomes likely that the TBAG-**S2** structures differences were due to slightly different conditions when the initial seed crystals formed. Specifically, when considering the intermolecular bonding of TBAG-**S2**, the O5-H50 bond doesn't participate in hydrogen bonding. In TBAG-**S1**, the O5-H50 bond donates a hydrogen bond to the O9 oxygen atom located on cyclohexanone, which may contribute to stabilization of the orientation of the solvent molecule. Previous research from Stevens and Dowd establishes that gossypol and gossypol derivatives are likely to utilize all possible hydrogen bonding in stabilizing dimer and solvent interactions [8].

It's not unanticipitated that among the amine derivatives, HPAG-**S1** has the greatest number of hydrogen bonds per molecule within the unit cell. As stated previously, it is the only derivative studied that contains an alcohol functional group on the substituted amine alkyl chains. Naturally this gives HPAG-**S1** the ability to donate and accept more hydrogen bonds than all other gossypol amine derivatives presented, including gossypol, when also considering the hydrogen bonding of the N1H and N2H bonds. The hydrogen bonding networks present in HPAG-**S1** not only include host-host interactions; and host-solvate interactions (acetone:water); but also uniquely include solvate-solvate (acetone: 0.5 water) hydrogen bonding. The solvate interactions occurs between H62 of the water molecule donating a hydrogen bond to the O40 oxygen atom located on the neighboring acetone molecule. Upon further inspection, the water molecule only interacts with HPAG's alcohol group located on one of the disordered states of the extended amine chain. Two interactions exists that stabilize HPAG's solvation with water. The O6A oxygen atom accepts a hydrogen bond from the O6O-H61 bond and the O6A-H6A alcohol donates a hydrogen bond to the O6O oxygen atom on water. In view of water's limited orientation with only two disordered state it is not out of the realm of possibility that the presence of water is likely to cause the disorder present in the 3-aminoproponal side chain starting at the C27 atom. The ordered 3-aminopropanol side chain starting at C31 atom is stabilized by the O2-H2 alcohol group donating a hydrogen bond to the O40 oxygen atom located on an acetone solvate. The ordered 3-aminoproponal chain doesn't interact with water, but only with acetone. Neither acetone molecule hydrogen bonds with either the C35A-C36A-O6A orientation or the C35B-C36B-O6B orientation, but acetone does hydrogen bond to the C34 atom, common to both orientations via C34-H34B donating a hydrogen bond to the O50 oxygen atom on acetone. Rigid stabilization of the C34 atom may act as a molecular joint that allows for

either the A or B orientation of 3-aminopropanol disorder. The presence of water in the HPAG-**S1** solution was an unexpected surprise since the HPAG material was recrystallized from ≥ 99.5% acetone solution. Water contamination was not expected since it was not observed in other recrystallizations from saturated solutions of acetone. A possible explanation for the presence of water is that when the saturated solutions are being prepared in the HPLC vials, they are heated momentarily and the vial tops are reopened to add more material to super saturate the solution. In previous research with MG, a ratio of host to water solvate of (1:1) was observed in crystals recrystallized from an anhydrous chloroform solution.

Charge Density and Topological Analysis

When examining features of the electron density at the BCPs for MG, a number of interesting features become apparent about the electron bond distribution. The C-C bonds that exist within the naphthalene rings have a higher density than the C-C bonds that are not within the conjugated rings. For example, the C5-C23, C23-C24, and C23-C25 contain BCP densities are all lower than any of the C1→C10 bonds. Resonance within the naphthalene naturally leads to higher bond density at the C-C* bonds than C-C bonds that do not have π character. However, the exception is the C8-C22 BCP that contains the highest C-C density (2.053 e $Å^{-3}$) of any bond that isn't in the ring system. The C22 atom forms a double bond with the O2 atom which allows resonance forms to contribute π-electron character to the C8-C22 bond. Initially, it could be expected that the internaphthayl bond at C2-C2' would have a lower BCP density due to steric effects from the functional groups on both rings. The C2-C2' BCP density (1.670 e $Å^{-3}$) is similar to the density of all other non resonating carbon-carbon bonds, and also confirms the

expectation that no resonance occurs within the bond. The C-H bond densities are very similar at the positions of the C21→C25, C23, and C31 carbon atoms, with an average BCP density of (1.959 e $Å^{-3}$). In contrast, the C4-H4 BCP (1.839 e $Å^{-3}$) is somewhat lower probably due to the electron with drawing character of the aromatic rings.

When evaluating the O-H bonds at the O1 and O3 oxygen positions, there exist BCP densities that vary by only a 0.002 e $Å^{-3}$ difference. This small deviation should be expected at these BCPs, considering that both alcohol groups are attached at equivalent C_n-OH carbon atoms. Of all the atoms bonded to oxygen, the C22-O2 bond should have the highest BCP and it is confirmed with the greatest bond density of 2.837 e $Å^{-3}$. The C-O bonds at the C7-O3, C6-O4, and C1-O1 BCP positions show variations in BCP values. Specifically, when comparing the C7-O3 BCP density of 2.407 e $Å^{-3}$ is significantly higher when compared to the other carbon oxygen bonds, while the density of the BCPs at the C6-O4 and C1-O1 positions only differ by 3.1%. The major factor that is distinct with the C7-O3 bond, compared to all other C-O bonds, is the aldehyde functional group positioned at the adjacent C8 atom. It is likely that the aldehyde group in conjugation with the naphthalene ring is contributing partial double bond character along the C7-O3 bond.

The charge density of PAG is very similar to MG at equivalent bonds (Table 3). The C-C bonds within the naphthalene ring system in PAG contains higher density than all other C-C bonds due to the delocalization of the π-electrons in the rings. The C-C bonds not within the aromatic carbon rings have BCP densities that vary from 1.606 to 2.071 e $Å^{-3}$. The C5-C23 BCP is lower than the C23-C24 and C23-C25 BCPs. One factor that may contributing to this decreased density is the steric strain due to the bulky iso-propyl groups, since the C3-C21 bond critical point density is higher. Both alkyl chains originating from the N1 and N2 atoms,

C31→C33 and C34→C36 respectively, have C-C BCP densities that decrease as you move away from the nitrogen atoms. The majority of all BCP densities of C-H bonds are within the range of 1.6 to 1.7 e $Å^{-3}$ with the exception of the C4-H4 bond that has a density of 1.953 e $Å^{-3}$.

In PAG, the three C-O bonds consist of two alcohol groups and one carbon to oxygen atom where the oxygen has a formal negative charge. While the BCP densities at the alcohol groups are similar, the C7-$O2^-$ has the highest density of all the BCP densities at 2.696 e $Å^{-3}$. The O1-H1 has a BCP density of 2.606 e $Å^{-3}$ where as the O3-H3O bond has a BCP of 2.271 e $Å^{-3}$.

Both nitrogen atoms form a total of three bonds that show only minor differences in their corresponding BCP densities. The C22-N1 and C27-N2 have the second highest BCPs within the PAG molecule along the carbon nitrogen bond. The N2-H2 and N1-H1 BCP densities are almost identical and higher than all other alkyl C-H bonds. In the same manner, the N1-C31 and N2-C34 contain higher BCP densities than any other alkyl chain C-C bonds.

When evaluating the differences and similarities between PAG and MG at equivalent bonds, in many instances, it is the presence of the functional groups on each molecule that should predominately be the rational for differences observed in covalent BCP densities of corresponding bonds. When comparing the peak BCP densities in the naphthalene rings for PAG and MG, the C5-C6, C3-C4, and C1-C2 have the highest BCP densities in descending order. The C5-C10 ring bond, in both structures has the lowest BCP density within the naphthalene rings. The differences in all other bonds within the naphthalene rings in order from highest to lowest bond densities, overall, are very small. Specifically, the range from highest to lowest BCP in each ring are 2.342-1.902e $Å^{-3}$ for MG and 2.324-1.969 e $Å^{-3}$ for PAG. These similarities suggest charge densities of the naphthalene rings are not significantly influenced by

the amine alkyl group and the anionic oxygen on PAG or the additional alcohol groups and methoxy groups on MG. The C1-O1 BCP density on both PAG and MG differ only by 0.02 e Å^{-3}, and similar small differences are seen at the corresponding C11-O4 (PAG) and C1'-O1' (MG) bond positions. The C8-C22 BCP density differences are relatively small on both molecules and differ by only 0.018 e Å^{-3}. Initially, a greater change would have been expected due to adjacent bonds from the C22 atoms consisting of C□O for MG versus the C-N bond for PAG, but the data doesn't support this conclusion. The C7-O3 bond in MG and C7-O2 equivalent bond in PAG show a BCP density difference of 0.289e Å^{-3} where the larger BCP density is likely from the $O2^{-}$ anion accumulating excess charge density. The C6-O4 bond has a BCP density of 2.010 e Å^{-3} on MG and the corresponding bond on PAG, the C6-O3 bond, has a BCP density of 2.265 e Å^{-3}. The differences, in this case, are probably due to the O4 oxygen atom bonded to a methyl group and the O3 bonded to a hydrogen atom. Both the isopropyl groups and methyl groups have similar C-C BCP densities, but the C-H bonds on these alkyl groups show BCP density deviations on average of 0.2123e Å^{-3} where the higher values are present on MG.

Oddershede and Larsen have successfully conducted detailed charge density studies on naphthalene at various low temperatures that included 100 and 135 K [148]. In the following analysis, the focus will be on the data conducted on the naphthalene rings at 135 K (Table 4). The naphthalene structure has BCP densities that are symmetric via an inversion center located in the middle of the C3 to C3' bond (or the C9-C10 bond for DMG and PAG) where the highest BCP densities are at the C1-C2 and C4-C5 positions. MG at equivalent bonds C1-C2, C3-C4, C5-C6, and C7-C8 on one ring (and C1'-C2', C3'-C4', C5'-C6', and C7'-C8' on the equivalent ring) also contain the highest BCP densities. PAG has a similar decreasing order for the four highest peaks (also including the C11-C12, C13-C14, C15-C16, and C17-C18 on the second

ring) on both rings with the BCP density similar to MG except at the C7-C8 and C17-C18 BCP positions. The BCP density ranges for naphthalene are between 2.030-2.252 e $Å^{-3}$, which are very similar to those of both the PAG and MG ring structures. These similarities in the BCP densities in the aromatic rings leads to the conclusion that the functional groups that distinguish PAG and MG have only a small effect on the electronic structures of the rings.

When examining the global fit of the model to x-ray data in the region of the ring systems in both PAG and MG, the static residual maps ($\Delta\rho_{residual}$) are nearly flat and a good indicator that the multipole models are in good agreement with the experimental data (fig. 4.1 & fig. 4.2). When examining the MG residual, specifically, circular contours exist at the centers of both rings that are attributed to Fourier series termination effects, and similar features have been observed in other charge density studies. Features of similar size are also observed in the residual density of PAG, but since they are not located at the ring centers, they cannot be easily attributed to series termination errors. Since these residual densities have not been included in the valence electrons density model, they can be attributed to noise associated with random errors in the experimental data. In conclusion, the residual densities indicate that satisfactory multipole models were successfully obtained from the x-ray data, and the resulting electron density distributions are in agreement with general considerations of covalent bonding theory.

In addition, the gradient trajectories provide detailed geometric representations of the hydrogen bonding. In figure 4.3, depicts two hydrogen bonds within the MG molecule. The figure to the left shows the gradient trajectories associated with hydrogen bonding between the O3-H3... O2 atoms. The figure to the right shows the gradient trajectories in the plane of the C22-H22 ... O(1) intramolecular hydrogen bond. Both figures show the bond critical points not

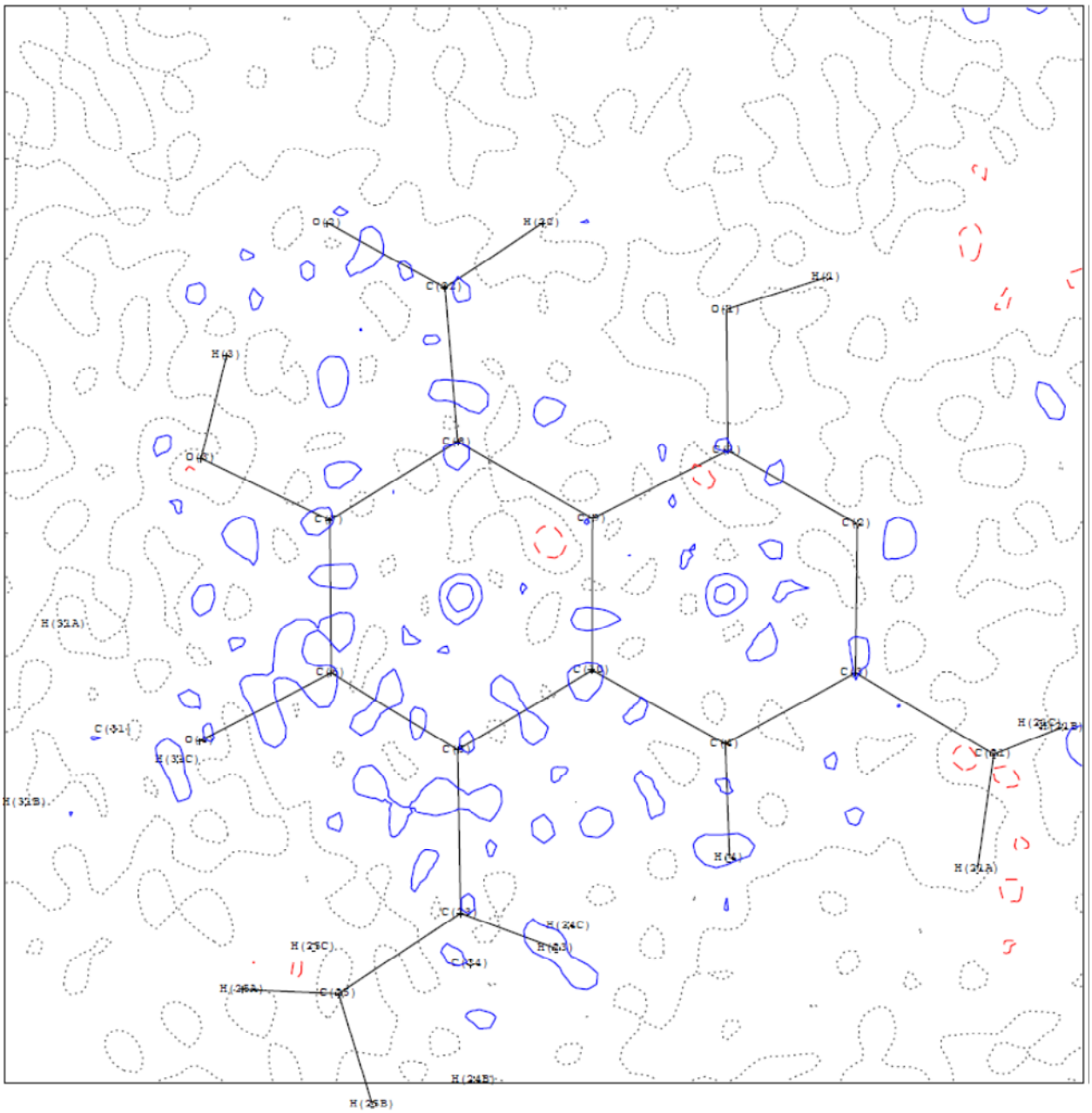

Figure 4.1 Residual density maps of Di(methoxy)gossypol through one of the naphthalene rings. Contours are plotted at 0.1 e Å^{-3} intervals with positive contours represented by solid (blue) lines, negative contours by dashed (red) lines, and zero contour by dotted (black) lines.

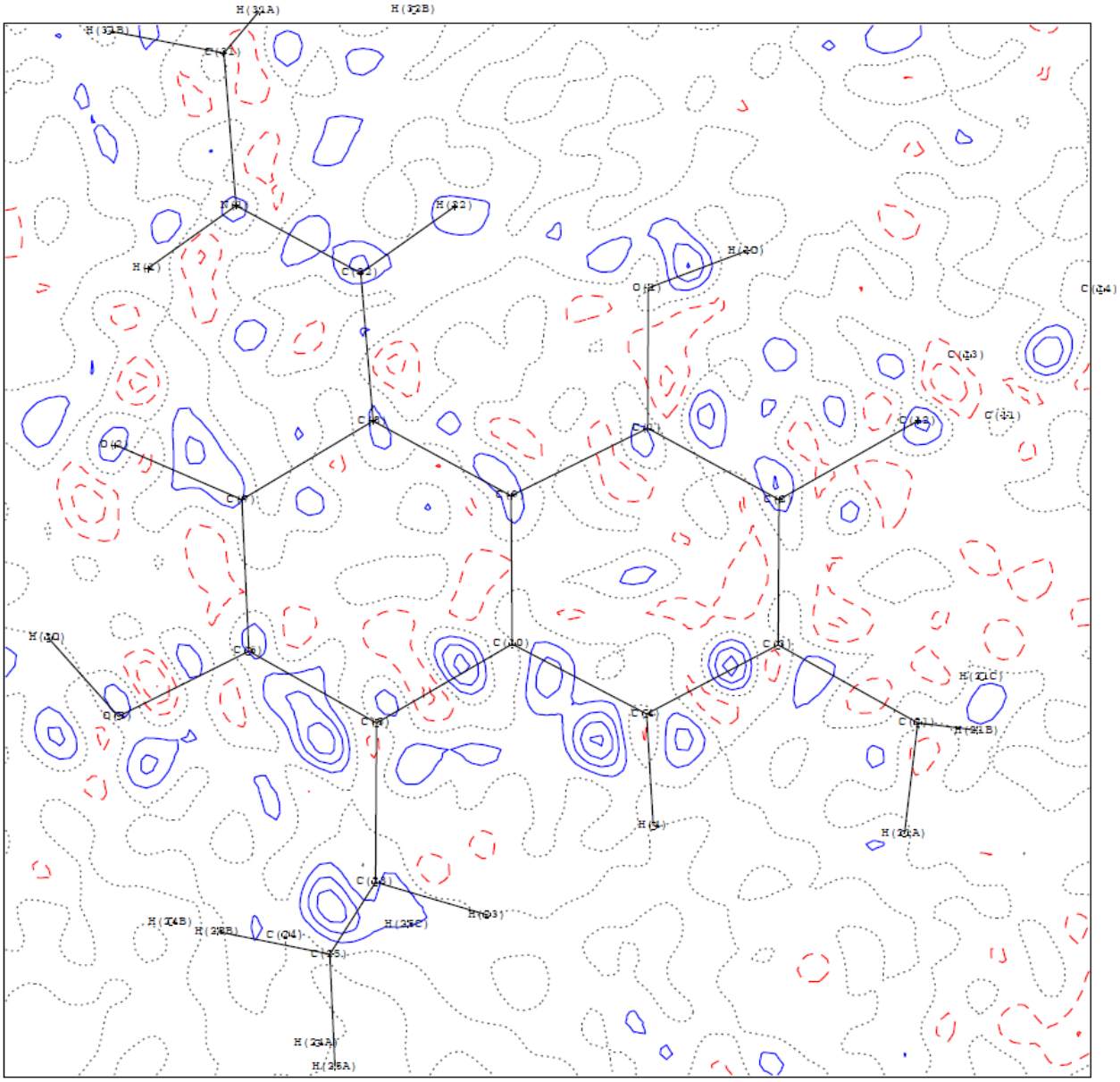

Figure 4.2 Residual density maps of di(propylamino)gossypol through one of the naphthalene rings. Contours are plotted at 0.1 e Å^{-3} intervals with positive contours represented by solid (blue) lines, negative contours by dashed (red) lines, and zero contour by dotted (black) lines.

only present in covalent interactions, but in the hydrogen bonds as well. Thus, according to topological analysis, the hydrogen bond interactions are naturally defined as bonds. Both ring and cage critical points are also present and exist in areas where they were expected, further validating Bader's analysis on complex chemical systems. A more global picture of the gradient trajectories superpositioned with the experimental charge density for one of the naphthalene rings in MG is shown in figure 4.4. Like the previous trajectory maps, critical points are identified and positioned in areas where covalent bonds, rings, and hydrogen bonds should exists.

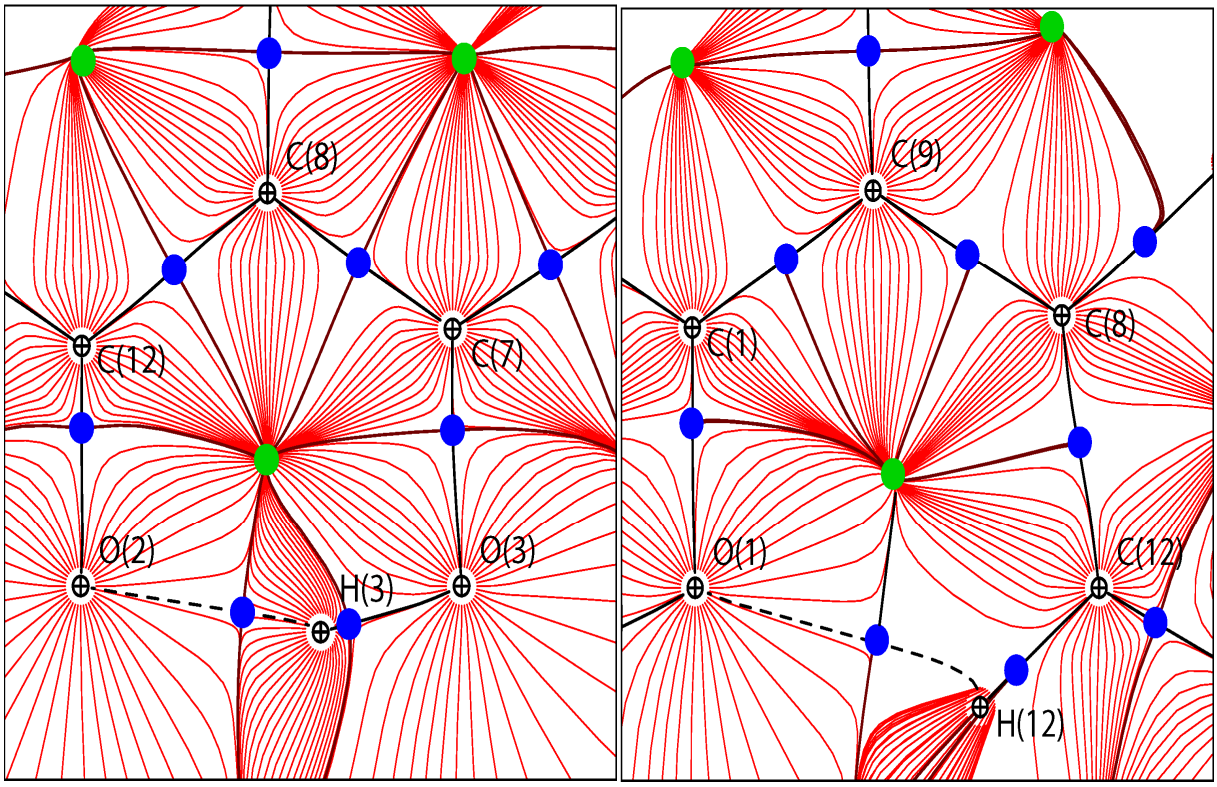

Figure 4.3 (Left) Gradient trajectories (red lines) of the experimental electron density distribution of 6,6'-dimethoxygossypol in the plane of the O(3)-H(3) . . . O(2) intramolecular hydrogen bond. Bond critical points are indicated by blue circles, ring critical points by green circles, and cage critical points by pink circles.

Figure 4.3 (Right) Gradient trajectories (red lines) of the experimental electron density distribution of 6,6'-dimethoxygossypol in the plane of the C(22)-H(22) . . . O(1) intramolecular hydrogen bond. Bond critical points are indicated by blue circles, ring critical points by green circles, and cage critical points by pink circles.

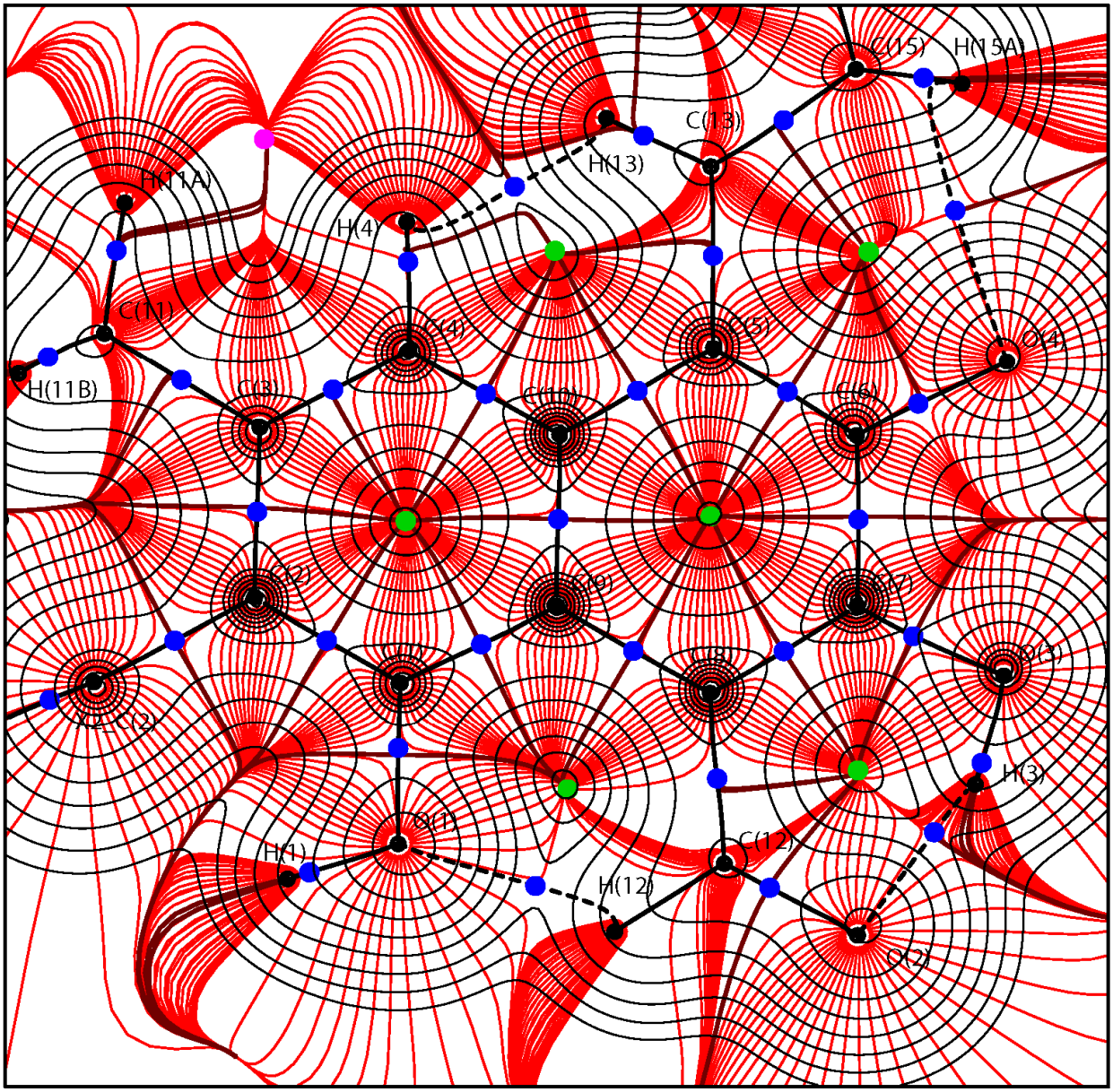

Figure 4.4 Superposition of the total electron density (black contour lines) and gradient trajectories (red lines) in the experimental electron density distribution of 6,6'-dimethoxygossypol. Bond critical points are indicated by blue circles, ring critical points by green circles, and cage critical points by pink circles.

Table 3		DMG VS PAG(at equivalent bonds)		
	DMG			PAG
Bond	$\rho(r_b)(eA^{-3})$		Bond	$\rho(r_b)(eA^{-3})$
C1-C2	2.257(1)		C1-C2	2.222(1)
C2-C3	2.098(1)		C2-C3	2.144(1)
C3-C4	2.246(1)		C3-C4	2.318(2)
C5-C6	2.319(2)		C5-C6	2.324(2)
C6-C7	2.095(1)		C6-C7	2.089(1)
C7-C8	2.150(1)		C7-C8	2.103(1)
C8-C9	1.987(1)		C8-C9	1.957(1)
C9-C10	2.100(1)		C9-C10	2.066(1)
C11-C12	2.274(1)		C11-C12	2.240(1)
C12-C13	2.091(1)		C12-C13	2.151(1)
C13-C14	2.232(1)		C13-C14	2.321(2)
C15-C16	2.342(2)		C15-C16	2.328(2)
C16-C17	2.102(1)		C16-C17	2.113(1)
C17-C18	2.146(1)		C17-C18	2.113(1)
C18-C19	2.006(1)		C18-C19	1.982(1)
C19-C20	2.100(1)		C19-C20	2.051(1)
C14-C20	2.144(1)		C14-C20	2.172(1)
C15-C20	1.902(1)		C15-C20	1.984(1)
C18-C27	2.053(1)		C18-C27	2.047(1)
C13-C26	1.839(1)		C13-C26	1.836(1)
C15-C28	1.676(1)		C15-C28	1.611(1)
C28-C29	1.666(1)		C28-C29	1.695(1)
C28-C30	1.607(1)		C28-C30	1.634(1)
C8-C22	2.053(1)		C8-C22	2.071(1)
C3-C21	1.839(1)		C3-C21	1.837(1)
C5-C23	1.676(1)		C5-C23	1.608(1)
C23-C24	1.666(1)		C23-C24	1.687(1)
C23-C25	1.607(1)		C23-C25	1.718(1)
C8-C22	2.053(1)		C8-C22	2.071(1)
C5-C10	1.902(1)		C5-C10	1.969(1)
C4-C10	2.144(1)		C4-C10	2.177(1)
C4-H4	1.839(1)		C4-H4	1.953(1)
C14-H14	1.839(1)		C14-H14	1.956(1)
C21-H21A	1.982(1)		C21-H21A	1.729(1)
C21-H21B	1.939(1)		C21-H21B	1.727(1)
C21-H21C	1.947(1)		C21-H21C	1.718(1)
C22-H22	1.851(1)		C22-H22	1.854(1)
C23-H23	1.964(1)	Table Continued	C23-H23	1.630(1)

C24-H24A	1.969(1)		C24-H24A	1.778(1)
C24-H24B	1.978(1)		C24-H24B	1.774(1)
C24-H24C	1.971(1)		C24-H24C	1.778(1)
C25-H25A	1.960(1)		C25-H25A	1.787(1)
C25-H25B	1.952(1)		C25-H25B	1.773(1)
C25-H25C	1.960(1)		C25-H25C	1.775(1)
C26-H26A	1.952(1)		C26-H26A	1.699(1)
C26-H26B	1.939(1)		C26-H26B	1.703(1)
C26-H26C	1.947(1)		C26-H26C	1.688(1)
C28-H28	1.964(1)		C28-H28	1.591(1)
C29-H29A	1.969(1)		C29-H29A	1.780(1)
C29-H29B	1.978(1)		C29-H29B	1.773(1)
C29-H29C	1.971(1)		C29-H29C	1.784(1)
C30-H30A	1.960(1)		C30-H30A	1.783(1)
C30-H30B	1.952(1)		C30-H30B	1.778(1)
C30-H30C	1.960(1)		C30-H30C	1.779(1)
O1-C1	2.167(1)		O1-C1	2.187(1)
O3-C7	2.407(1)		O2-C7	2.696(2)
O4-C6	2.010(1)		O3-C6	2.265(1)
O4-C11	2.167(1)		O4-C11	2.214(1)
O7-C17	2.407(1)		O5-C17	2.653(2)
O8-C16	2.010(1)		O6-C16	2.250(1)
O1-H1	2.136(1)		O1-H1	2.606(2)
O5-H5	2.136(1)		O4-H4O	2.851(3)

Table 4	Comparison of Naphthalene with PAG and MG			
		$\rho(r_b)$ (eA^{-3})		
Bonds	PAG	MG	Naphthalene	
C1-C2	2.222(1)	2.274(1)	2.252(1)	
C2-C3	2.144(1)	2.091(1)	2.030(1)	
C3-C4	2.318(2)	2.232(1)	2.234(1)	
C4-C10	2.177(1)	2.144(1)	2.038(1)	
C5-C10	1.969(1)	1.902(1)	2.058(1)	
C5-C6	2.324(2)	2.342(2)	2.252(1)	
C6-C7	2.089(1)	2.102(1)	2.030(1)	
C7-C8	2.103(1)	2.146(1)	2.234(1)	
C8-C9	1.975(1)	2.006(1)	2.038(1)	
C9-C10	2.066(1)	2.100(1)	2.024(1)	
C9-C1	2.123(1)	1.944(1)	2.058(1)	
C11-C12	2.240(1)	2.274(1)	2.252(1)	
C12-C13	2.151(1)	2.091(1)	2.030(1)	
C13-C14	2.321(2)	2.232(1)	2.234(1)	
C14-C20	2.172(1)	2.144(1)	2.038(1)	
C15-C20	1.984(1)	1.902(1)	2.058(1)	
C15-C16	2.328(2)	2.342(2)	2.252(1)	
C16-C17	2.113(1)	2.102(1)	2.030(1)	
C17-C18	2.113(1)	2.146(1)	2.234(1)	
C18-C19	1.982(1)	2.006(1)	2.038(1)	
C19-C11	2.128(1)	1.994(1)	2.058(1)	
C19-C20	2.051(1)	2.100(1)	2.024(1)	

Conclusion

The structures of 6,6'-dimethoxygossypol (MG) and eight new crystalline forms of amine gossypol derivatives have been determined. These structures provide evidence that while amine gossypol derivatives are limited in their intermolecular bonding with other molecules, when compared to gossypol, they still retains the ability to incorporate guest molecules into the crystalline state. Like gossypol, both MG and the amine gossypol derivatives contain a number of functional groups, internal symmetry, and possible alternate tautomeric states. In addition, MG and the amine gossypol derivatives retain a great deal of the rich chemistry present in gossypol. Much of gossypol's complex chemical behavior has been elucidated by x-ray diffraction studies, and while MG possesses many of structural components of gossypol, the presence of the methyl groups and the absence of the alcohol group provides a significant change in both the chemical and physical behavior of MG. Thus, crystallographic analysis of gossypol derivatives, like MG and the amine derivatives, are needed to understand how substitution, for example, of hydroxyl groups with methoxy groups or aldehyde groups with imine groups changes the structural and electronic character of the molecule.

In addition to structural studies, this dissertation reports the first experimental determinations of the electron density distributions of gossypol related compounds using high resolution single crystal x-ray diffraction measurements. Refinement of x-ray data collected at 120 K from single crystals of MG and dipropylaminegossypol (PAG) using a multipole deformation model show well resolved features associated with covalent bonding and non-bonding lone pair electron distributions. In addition, topological analysis of the electron density

using AIM concepts yields parameters which characterize not only the covalent bonds, but also weaker intra- and intermolecular interactions as well.

Of the many possible chemical modifications of gossypol, the amine derivatives are perhaps the most actively researched. Interestingly, substitution of the aldehyde group with an imine group in PAG has little effect on the electron distribution in the naphthalene rings, when compared to MG. Even when compared to the electron density of naphthalene itself, it appears that substitution of various groups have little effect on the pi electron character of the aromatic rings system. Most importantly, these studies demonstrate that reliable experimental methods now exist that give the ability to answer complex questions dealing with the electron density of complex molecules of this type that were not present before.

While the number of publications for gossypol far exceeds that of MG, the numbers of crystal structures for MG will more than likely increase in the future. Few structural studies of gossypol derivatives, other than amino based gossypol derivatives, are currently present in the literature and many gossypol derivatives are being investigated. For instance, gossypolone a well known derivative of gossypol that has proven to be a central in many paths for synthesizing other gossypol derivatives, has only two known structure determinations. However because of active research with gossypol and its derivatives; x-ray structure analysis is providing indispensable information on the molecular behavior of these biological active molecules. Currently, at the fore front of this research are apogossypol, apogossypol derivatives, apogossypolone, and apogossypolone derivatives. While the biochemistry and physiology of apogossypol and its derivative are moderately understood, there have yet to be any crystal structures reported for these molecules. In the last 30 years, enzymology has greatly advanced because of molecular structural studies and studies of how enzymes interact with their molecular

counterparts. Thus, x-ray structural analysis of apogossypol and its derivative coupled with modeling and activity studies are crucial in providing a better understanding of the biochemical mechanisms that are inherent in these molecules which may help further in understanding anticancer activity and other pharmacological effects.

Future research endeavors will include not only attempts in generating new crystal forms of gossypol and gossypol derivatives, but will also include further detailed charge density studies based on additional accurate high-resolution crystallographic data sets. Currently, charge density studies are becoming a more mainstream tool in understanding chemical behavior. The number of charge density studies published per year is increasing and, with the advancement of x-ray crystallographic technology becoming cheaper and more powerful, will advance the utilization of topological analysis in chemistry. Data bases of charge densities are being constructed on a large array of molecules ranging from amino acids to newly synthesized drugs. These data bases will aid not only on a more comprehensive understanding of the electronic nature of molecules but likely be applied to very complex electronic interactions such as protein analysis and organometallic chemistry.

Computational chemistry is also developing at a rapid pace, largely driven by increases in technological advancement. However, experimentation is still the litmus test for theoretical methods, and charge density studies provide a detailed benchmark against which new molecular theories and computational techniques may be rigorously tested.

References

1.) Dowd, M. K.; Pelitire, S. M. Isolation of 6-Methoxy Gossypol and 6, 6'-Dimethoxy Gossypol from *Gossypium barbadense* Sea Island Cotton, *J. Agric. Food Chem.* **2006**, *54,* 3265- 3270.

2.) Howell, C.R.; Hanson L. E.; Stipanovic R. D.; Puckhaber L. S. Induction of terpenoid synthesis in cotton roots and control of *Rhizoctonia solani* by seed treatment with Trichoderma virens. *Phytopathology* **2000**, *90*, 248- 252.

3.) Hoeffer A. P.; Agarwal A.; Meltzer P.; Naqvi R.; Matlin S. A. Antifertility, spermicidal, and ultrastructural effects of gossypol and derivatives administered orally and by intratesticular injections. *Contraception* **1988**, *37*, 301.

4.) Flack, M. R.; Pyle, R. G.; Mullen, N. M.; Lorenzo, B.; Wu, Y. W.; Knazek, R. A.; Nisula, B. C.; Reidenberg, M. M. Oral gossypol treatment of metastatic adrenal cancer. *J. Clin. Endocrinol. Metabol.* **1993**, *76*, 1019-1024.

5.) Coyle, T.; Levante, S.; Shetler, M.; Winfield J. In vitro and in vivo cytotoxicity of gossypol against central nervous system tumor cell lines. *J. Nuero-Oncol*. **1994**, *19*, 25-35.

6.) Bottger, G. E.; Sheehan, E. T.; Lukefahr, M. J. Relation of gossypol content of cotton plants to insect resistance. *J. Econ. Entomol.* **1964**, *57*, 283.

7.) Dowd, M. K.; Stevens, E. D. The gossypol-cyclododecanone (1/2) inclusion complex. *Acta Cryst., Sect. C: Cryst. Struct. Commun.* **2003**, *59*, 397- 399.

8.) Zelaya, C. A.; Dowd, M. K.; Stevens, E. D. 6, 6'-Dimethoxygossypol: molecular structure, crystal polymorphism, and solvate formation. *Struct. Chem*. **2010**, *21*, 113-122.

9.) Marchlewski, L. Gossypol: Ein Bestandtheil de Baumwollsamen, *J. Prakt. Chem*. **1899**, *60*, 84-94.

10.) Longmore, J. Cotton Seed Oil: Its Coloring Matter and Mucilage, and Description of a New Method of Recovering the Loss Occurring in the Refining Process. *J. Chem. Ind.* (London) **1886**, *5*, 200-206.

11.) Miller, R. F.; Adams, R. The Structure of Gossypol 4. Anhydrogossypol and Its Derivatives. *Ibid*. **1937**, *59*, 1736-1738.

12.) Adams, R.; Morris, R. C.; Kirkpatrick, E. C. Structure of Gossypol IX. Oxidiation and Degradation of Gossypol Hexamethyl Ether; Gossic Acid. *Ibid.* **1938**, *60*, 2170-2174.

13.) Adams, R.; Friedman, B. S.; Pierce, C. C.; Morris, R. C.; Kirkpatrick, E. C.; Structures of Gossypol VI. Addition Products with Butadienes. *Ibid*. **1938**, *60*, 2160-2162.

14.) Adams, R.; Kirkpatrick, E. C. Structure of Gossypol. XI. Absorption Spectra of Gossypol, Its Derivatives and of Certain Dinaphthalene Compounds. *Idib*. **1938**, *60*, 2180-2184.

15.) Campbell, K. N.; Morris, R. C.; Adams, R. The Structures of Gossypol. I. *J. Am. Chem. Soc*. **1937**, *59*, 1723-1728.

16.) Adams, R.; Geissman, T. A. Structures of Gossypol. VII. Gossypol Dimethyl Ether, *Ibid*. **1938**, *60*, 2163-2166

17.) Adams, R.; Butterbaugh, D. J. Structure of Gossypol. X. Appogossypol and Its Degradation Products. *Ibid* **1938**, *60*, 2174-2180.

18.) Adams, R.; Morris, R. C.; Butterbaugh, D. J.; Kirkpatrick, E. C. Structure of Gossypol. XIV. Apogossypolic Acid. *Ibid*. **1938**, *60*, 2191-2193.

19.) Adams, R.; Baker, B. R. Structure of Gossypol. XXI. Synthesis of 1, 2-Dimethoxy-3-isopropyl-4-benzoic Acid and of Apogossypolic Acid. *Ibid.* **1939**, *61*, 1138-1142.

20.) Adams, R.; Geissman, T. A.; Morris, R. C. Structures of Gossypol XVI. Reduction Products of Gossypolone Tetramethyl Ether and Gossypolonic Acid Tetramethyl Ether. *Ibid*. **1938**, *60*, 2967-2970.

21.) Adams, R.; Hunt, M. Structure of Gossypol. XIX. Synthesis of 1, 2-Dihydroxy-3-isopropyl-6-benzoic Acid. *Ibid*. **1939**, *61*, 1132-1133.

22.) Adams, R.; Hunt, M.; Morris, R. C.; Structure of Gossypol. XVII. Synthesis of 1,2-Dimethoxy-3-isopropyl-5-aminobenzene, a Degradation Product of Gossypol. *Ibid*. **1938**, *60*, 2972-2974.

23.) Adams, R.; Geissman, T. A.; Dial, W. R.; Fitzpatrick, J. T. Structure of Gossypol, XXVI. Gossypolic Acid. *Ibid*. **1941**, *63*, 2439-2441.

24.) Adams, R.; Geissman, T. A. Structure of Gossypol, XXIII. Attempts to Prepare Desapogossypolone Tetramethyl Ether. Condensation of Hexadiene-2, 4 with Dibenzoylethylene. *Ibid*. **1939**, *61*, 2083-2089.

25.) Adams, R.; Baker, B. R. Structure of Gossypol, XXV. Synthesis of Desapogossypolone Tetramethyl Ether. *Ibid*. **1941**, *63*, 535-537

26.) Edwards Jr., J.D.; Cashaw, J. L. Studies in the Naphthalene Series. III. Synthesis of Apogossypol Hexamethyl Ether. *Ibid*. **1957**, *79*, 2283-2285.

27.) Boatner, C. H. *Pigments of Cottonseed, in Cottonseed and Cottonseed Products, Their Chemistry and Chemical Technology*, Bailey, A. E. Eds.; Interscience: New York, 1948; pp 213-363.

28.) Edwards, J. D. Total Synthesis of Gossypol. *J. Am. Chem. Soc*. **1958**, *80*, 3798- 3799.

29.) Edwards, J. D.; Cashew, J. L. Synthesis of Apogossypol Hexamethyl Ether. *Ibid*. **1956**, *78*, 3224- 3225.

30.) Kenar, J. A. Reaction Chemistry of Gossypol and Its Derivatives. *JAOCS*. **2006**, *83*, 269-296.

31.) Withers, W. A.; Carruth, F. E. Gossypol a Toxic Substance in Cottonseed. A preliminary Note. *Science*, **1915**, *41*, 324.

32.) Withers, W. A.; Carruth, F. E. Gossypol a Toxic Substance in Cottonseed Meal. *J. Agric. Res.,* **1915**, 5, 261- 288.

33.) National Coordinating Group on Male Infertility Agents. Gossypol-a new ant fertility agent for males. *China Med. J. (New Series)* **1978**, 417.

34.) Waller , D. P.; Zanevald, L. J. D.; Farnsworth, N. R. Gossypol: Pharmacology and Current Status as a Male Contraceptive. *Econ. Med. Plant Res*. **1985**, *1*, 87-112

35.) Segal, S. J. *Gossypol, A Potential Contraceptive for Men*, Plenum Press: New York, 1985.

36.) Qian, S. Z.; Wang, Z. G. Gossypol: A Potential Antifertility Agent for Males. *Annu. Rev. Pharmacol. Toxicol.* **1984**, *24*, 329-360.

37.) Sang, G. W.; Lorenzo, B.; Reidenberg, M. M. Inhibitory Effects of Gossypol on Corticosteriod 11-β-Hydroxysteriod Dehydrogenase from Guinea Pig Kidney: A Possible Mechanism Hypokalemia. *J. Steroid Biochem. Mol. Biol*. **1991**, *30*, 169-176.

38.) Waites, G. M.; Wang, C.; Griffin, P. D. Gossypol: Reasons for its Failures to be Accepted as Safe, Reversible Male Antifertility Drug. *Int J Androl*. **1998**, *21*(5), 8-12

39.) Coutinho, E. M. Gossypol: A Contraception for Men. *Contraception* **2002**, *65*, 259-263.

40.) Reidenberg, M. M.; Gu, Z. P.; Lorenzo, B. J. Differences in serum potassium concentrations in normal men in different geographic locations. *Clinical. Chem*. **1993**, *39*, 72-75.

41.) Zhan, Y.; Jia, G. A Novel Method of Apogossypolone and its Antitumor Activity. *Letters in Drug Design and Discovery* [Online] **2009**, *6*, 129-132
http://www.ingentaconnect.com/content/ben/lddd/2009/00000006/00000002/007aj

42.) Meng, Y.; Tang, W.; Dai, Y.; Wu, X.; Liu, M.; Ji, Q.; Ji, M.; Pienta, K.; Lawrence, T.; Xu, L. Natural BH3 mimetic (-)- Gossypol Chemosensitizes Human Prostate Cancer via Bxl-xl Inhibition Accompanied by Increase of Puma and Noxa. *Mol. Cancer Ther*. **2008**, *7*(7), 2192-2202.

43.) Arnold, A.; Aboukameel, A.; Chen, J.; Yang, D.; Wang, S.; Al-Katib, A.; Mohammad, R. M. Preclinical studies of Apogossypolone: a new nonpeptidic pan small-molecule inhibitor of Bcl-2, Bcl-X_L and Mcl-1 proteins in Follicular Small Cleaved Cell Lymphoma model. *Molecular Cancer* [Online] **2008**, *7*, 1-10
http://www.molecular-cancer.com/content/7/1/20/abstract

44.) Abdullaev, N. D.; Tsychenko, A. A.; Nazarova, I. P.; Ul'chenko, N. T.; Yagudaev, M. R.; Glushenkov, A. I. H and C NMR Spectra of Transformation Products of Gossypol in Solutions. *Chem. Nat. Compd*. **1990**, *26*, 129-138.

45.) Vander Jagt, D. L.; Deck, L. M.; Royer, R. E. Gossypol: Prototype of Inhibitors Targeted to Dinucleotide Folds. *Curr. Med. Chem*. **2000**, *7*, 479-498.

46.) Gdaniec, M.; Ibragimov, B. T.; Talipov, S.A.; *Gossypol*. *Comprehensive Supramolecular Chemistry*, Vol. 6, *Solid-State Supramolecular Chemistry: Crystal Engineering*, edited by D. D. MacNicol, F. Toda & R. Bishop, 117-146. Oxford: Pergamon Press **1996**, 6, 117-146.

47.) Stipanovic, R. D.; Lopez, J. D.; Dowd, M. K.; Puckhaber, L. S.; Duke, S. E. Effect of Racemic and (+)- and (−)-Gossypol on the Survival and Development of *Helicoverpa zea* Larvae *J. Chem. Ecol*. **2006**, *32*, 959–968.

48.) Zhu, G. D.; Chen, D. H.; Huang, J. H.; Chi, C. S. Regioselective Bromination and Fluorination of Apogossypol Hexamethyl. *J. Org. Chem*. **1992**, *57*, 2316-2320.

49.) Datta, S. C.; Murti, V. V. S.; Seshadri, T. R. Isolation and Study of (+)-Gossypol from Thespesia populnea. *Indian J. Chem. Sect. B* **1972**, *10*, 263-266.

50.) Seshadri, T. R.; Sharma, N. N. Isolation of the Hexamethyl Ether of the Dilactol Form of Racemic Gossypol. *Indian J. Chem. Sect. B* **1975**, *13*, 865-866.

51.) Seshadri, T. R.; Sharma, N. N. Further Study of the Three Forms of (+)-Gossypol Hexamethyl Ether. *Ibid*. **1975**, *13*, 866-868.

52.) O'Connor, R. T.; Von der Haar, P.; DuPre, E. F.; Brown, L. E.; Pominski, C. H. The Infrared Spectra of Gossypol. *J. Am. Chem. Soc*. **1954**, *76*, 2368-2373.

53.) Wichmann, K.; Krusius, T.; Sinervirta, R.; Puranen, J.; Janne, J. Studies on Structure-Activity Relationship of Gossypol, Gossypol Ethers, and Three Naphthaldehydes in the Inhibition of Spermatozol Metabolism. *Contracepton* **1967**, *33*, 519-528.

54.) Baram, N. I.; Ismailov, A. I. Biological Activity of Gossypol and Its Derivatives. *Chem. Nat. Compd*. **1994**, *29*, 275-287.

55.) Carruth, F. E. Contribution to the Chemistry of Gossypol, the Toxic Principle of Cottonseed. *Ibid*. **1918**, *40*, 647-663.

56.) Clark, E.P. Studies on Gossypol. I. The Preparation, Purification, and Some of the Properties of Gossypol, the Toxic Principle of Cottonseed. *J. Biol. Chem*. **1927**, *75*, 725-739.

57.) Miller, R. F.; Butterbaugh, D. J.; Adams, R. Structure of Gossypol. II. Acylation. *J. Am. Chem. Soc.* **1937**, *59*, 1729-1731.

58.) Correa, O. G.; Cappi, H. M.; Salem, M.; Staffa, C. New Gossypol Derivatives. *J. Am. Oil Chem. Soc*. **1966**, 43, 678-680.

59.) Clark, E. P. Studies on Gossypol III. The Oxidation of Gossypol. *J. Biol. Chem*. **1928**, *77*, 81-87.

60.) Dao, V.-T.; Dowd, M. K.; Gaspar, C.; Martin, M.-T.; Hemez, J.; Laprevote, O.; Mayer, M.; Michelot, R. J. New Thioderivatives of Gossypol and Gossypolone, as Prodrugs of Cytotoxic Agents. *Bioorg. Med. Chem*. **2003**, *11*, 2001-2006.

61.) Hass, R. H.; Shirley, D. A. The Oxidation of Gossypol. II. Formation of Gossypolone with Ferric Chloride. *J. Org. Chem*. **1965**, *30*, 4111-4113.

62.) Scheiffele, E. W.; Shirley, D. A. The Oxidation of Gossypol. I. Early Stages in the Reaction of Gossypol and Oxygen. *J. Org. Chem*. **1965**, *29*, 3617-3620.

63.) Dao, V.-T.; Dowd, M. K.; Martin, M.-T.; Gaspard, C.; Mayer, M.; Mechelot, R. J. Cytotoxicity of enantiomers of gossypol Schiff's bases and optical stability of gossypolone. *Eur. J. Med. Chem*. **2004**, *39*, 619-624.

64.) Carruth, F. E. Contribution to the Chemistry of Gossypol, the Toxic Principle of Cottonseed. *Ibid*. **1918**, *40*, 647-663.

65.) Clark, E. P. Studies on Gossypol V. The Action of Chromic Acid upon Some Gossypol Derivatives. *J. Am.Chem. Soc*. **1929**, *51*, 1475-1478.

66.) Wei, J.; Rega, M. F.; Kitada, S.; Yuan, H.; Zhai, D.; Risbood, P.; Seltzman, H. H.; Twine, C. E.; Reed, J. C.; Pellecchia, M. Synthesis and Evaluation of Apogossypol Atropisomers as Potential Bcl-xL antagonists. *Cancer Letters* **2009**, *273*, 107-113.

67.) Zhan, Y.; Jia, G. A Novel Synthesis Method of Apogossypolone and its Antitumor Activity. Lett. Drug De. Discovery [Online] **2009**, *6*, 129-133 http://www.ingentaconnect.com/content/ben/lddd/2009/00000006/00000002/007aj

68.) Jia, L.; Coward, L. C.; Kerstner-Wood, C. D.; Cork, R. L.; German, G. S.; Noker, P. E.; Kitada, S.; Pellechia, M.; Reed, J. C. Comparison of pharmacokinetic and metabolic profiling among gossypol, apogossypol and apogossypol hexaacetate. *Cancer Chemother. Pharmacol.* **2008**, *61*, 63-73.

69.) Carruth, F. E. Methods for Approximating the Relative Toxicity of Cottonseed Products. *J. Biol. Chem.* **1917**, *32*, 87-90.

70.) Clark, E. P. Studies on Gossypol. II. Concerning the Nature of Carruth's D Gossypol. *Ibid.* **1928**, *76*, 229-335.

71.) Abou-Donia, M. B. Physiological Effects and Metabolism of Gossypol. *Residue Rev.* **1976**, *61*, 125-160.

72.) Dao, V. T.; Gaspard, C.; Mayer, M.; Werner, G. H.; Nguyen, S. N.; Michelot, R. J. Synthesis and cytotoxicity of gossypol related compounds. *Eur. J. Med. Chem*. **2000**, *35*, 805-813.

73.) Royer, R. E.; Mills, R. G.; Deck, L. M.; Mertz, G. J.; Vander-Jagt, D. L. Inhibition of Human Immunodeficiency Virus Type I Replication by Derivatives of Gossypol. *Pharmacol. Res*. **1991**, *24*, 407-412.

74.) Lin, T. S.; Schinazi, R. F.; Zhu, J.; Birks, E.; Carbone, R.; Si, Y.; Wu, K.; Huang, L.; Prusoff, W. H. Anti-Hiv Activity and Cellular Pharmacology of Various Analogs of Gossypol. *Biochem. Pharmacol*. **1993**, *46*, 251-255.

75.) Bejcar, G.; Przybylski, P.; Brzeinski, B. NMR, FT-IR as Well as PM5 Semiempirical Studies of New Hydrazone of Gossypol with 3-Oxa-n-Butylhydrazine. *J. Mol. Struct*. **2005**, *734*, 45-49.

76.) Ziyaev, Kh. L.; Kamaev, F. G.; Baram, N. I.; Biktimirov, L.; Ismailov, A. I. New Gossypol Imines. *Chem. Nat. Compd*. **1997**, *33*, 545-547.

77.) Matlin, S. A.; Roshdy, S.; Cass, G. B.; Freitas, C. G.; Longo, R. L.; Malvestiti, I. Structual Investigations of Gossypol Schiff's Bases. *J. Brazil. Chem. Soc*. **1990**, *1*, 128-133.

78.) Baram, N. I.; Kamaev, F. G.; Ziyaev, Kh. L.; Biktimirov, L.; Ismailov, A. I.; Nazarov, G. B.; Ibragimov, B. T. Structure of Gossypol Arylimines. *Ibid.* **1988**, *24*, 550-553.

79.) Przybylski, P.; Schilf, W.; Kamienski, B.; Brzezinski, B.; Bartl, F. C-13, N-15, CP-MAS, FT-IR and PM5 Studies of Some Schiff Bases of Gossypol in Solid. *Ibid.* **2005**, *748*, 111-117.

80.) Przybylski, P.; Schilf, W.; Brezinski, B. C-13, N-15, NMR and CP-MAS as Well as FT-IR and PM5 Studies of Schiff Bases of Gossypol with L-Phenylalanine Methyl Ester in Solution and Solid. *Ibid*. **2005**, *734*, 123-128.

81.) Przybylski, P.; Jasinski, K.; Brezinski, B.; Bartl, F. Spectroscopic Studies and PM5 Semiempirical Calclulations of New Schiff Bases of Gossypol with Amino Deriviatives of Crown Ethers. *Ibid.* **2002**, *611*, 193-201.

82.) Przybylski, P.; Schilf, W.; Brzezinski, B. C-13, N-15 NMR and CP-MAS as Well as FT-IR and PM5 Studies of Schiff Base of gossypol with l-Phenylalainine Methyl Ester in Solution and Solid. *Ibid*. **2005**, *734*, 123-128.

83.) Przybylski, P.; Wlodarz, M.; Schroeder, G.; Pankiewicz, R.; Brzezinski, B.; Bartl, F. ESI MS and PM5 Semiemperical Studies of Gossypol Base with (R)-Tetrahydrofurfuryl-amine Complexes and Monovalent Cations. *Ibid*. **2005**, *693*, 95-102.

84.) Przybyski, P.; Woldarz, M.; Brzezinski, B.; Bartl, F. Spectroscopic Studies and PM5 Semiempirical Calclulations of Tautomeric Forms of Gossypol Schiff Bases with (R)-Tetrahydrofurfurylamine. *Ibid*. **2004**, *691*, 227-234.

85.) Przybylski, P.; Ratajczak-Sitarz, M.; Katrusiak, A.; Schilf, W.; Wojciechowski, G.; Brzezinski, B. Crystal Structures of Schiff Base Derivative of Gossypol with 3, 6, 9,-Trioxa-decylamine. *Ibid*. **2003**, *655*, 293-300.

86.) Przybylski, P.; Schroeder, G.; Pankiewicz, R.; Brzezinski, B.; Bartl, F. Complexes of Schiff Base of Gossypol with n-Butylamine and Some Monovalent or Bivalent Cations Studied by ESI MS, NMR, FT-IR as Well as PM5 Semiemperical Methods. *Ibid*. **2003**, *658*, 193-205.

87.) Przybylski, P.; Brzezinski, B. The Complexes Between Schiff Base of Gossypol with L-Phenylalanine Methyl Ester and Some Monovalent Cations Studied by HNMR, ESI MS, FT-IR as Well as PM5 Semi-empirical Methods. *J. Mol. Struct*. **2003**, *654*, 167-176.

88.) Pryzbylski, P.; Schroeder, G.; Brzezinski, B. The Schiff Base of Gossypol with 2-(Aminomethyl)-18-crown-6 Complexes and H, Li, Na, K, Rb, Cs Cations Studied by ESI MS, HNMR, FT-IR and PM5 Semiempirical Methods. *Ibid*. **2004**, *669*, 65-77.

89.) Przybylski, P.; Bejcar, G.; Schroeder, G.; Brzezinski, B. Complexes of Schiff Base of Gossypol with 5-Hydroxy-3-oxapentylamine and Some Monovalent Cations Studied by ESI MS as Well as PM5 Semiempirical Methods. *Ibid*. **2003**, *654*, 245-252.

90.) Przybylski, P.; Brzezinski, B. Spectroscopic studies and PM5 semiempirical calculations of new Schiff bases of gossypol with polyoxaalkylamines.
Biopolymers **2002**, *67*, 61-69.

91.) Lyman, C. M.; Cronin, J. T.; Trant, M. M.; Odell, G. V. Metabolism of Gossypol in the Chick. *J. Am. Oil Chem. Soc*. **1969**, *46*, 100-104.

92.) Talipov, S.A.; Manakov, A.; Ibragimov, B. T.; Lipkwoski, J.; Tilijakov, Z. G. Sorption of Ammonia, Methylamine, and Methanol by the P3 Poloymorph of Gossypol. Synthesis of Unsymmetrical Monoamine Derivatives of Gossypol by a Solid State Reaction. *J. Inclusion Phen. Macrocyclic Chem.* **1997**, *29*, 33-39.

93.) Baram, N. I.; Ziyaev, Kh. L.; Ismailov, A. I.; Ziyamov, D.; Mangutova, Y. S. New Azoderivatives of Gossypol. *Chem. Nat. Compd*. **2000,** *36*, 185-188 & 541-542.

94.) Nazarova, I. P.; Glushenkova, A. I.; Markman, A. L. Some Products from the Combining of Gossypol with Diazotized Amines. *Khim. Prir. Soedin*. **1976**, *5*, 607-609.

95.) Bekarek, V.; Rothschein, K.; Vetesnik, P.; Vecera, M.; Estimation of Azo-Hydroazo Tautomeric Equilibrium in Orthohydroxy-azocompounds by NMR. *Tetrahedron Lett*. **1968**, *9*, 3711-3713.

96.) Kaul, B. L.; Nair, P. M.; Rama Rao, A. V.; Venkataraman, K. NMR Spectra of Azophenol and Quinone Hydrazones. *Tetrahedron Lett*. **1966**, *7*, 3897-3903.

97.) Rezhepov, K. Zh.; Ziyaev, Kh. L.; Baram, N. I.; Kamaev, F. G.; Levkovich, M. G.; Saiitkulov, A. M.; Ismailov, A. I. Azo-derivitives of Gossypol and Its Imines. *Khim. Prir. Soedin.* **2003**, *4*, 289-291.

98.) Fischer, P. B.; Kaul, B. L.; Zollinger, H. Untersuchungen uber die Struktur von Formazanen I N-H-Kopplung des Chelatwasserstoffatoms. *Helv. Chim. Acta* **1968**, *51*, 1449-1451.

99.) Zhu, G. D.; Chen, D. H.; Huang, J. H.; Chi, C. S. Regioselective Bromination and Flourination of Appogossyopol Hexamethyl Ether. *J. Org. Chem*. **1992**, *57*, 2316-2320.

100.) Royer, R. E., Deck, L. M.; Campos, N. M.; Hunsaker, L. A.; Vander-Jagt, D. L. Biologically Active Derivatives of Gossypol: Synthesis and Antimalarial Activities of Peri-acylated Gossylic Nitriles. *J. Med. Chem*. **1986**, *29*, 1799-1801.

101.) Vander Jagt, D. L.; Deck, L. M.; Royer, R. E. Gossypol: Prototype of Inhibitors Targeted to Dinucleotide Folds. *Curr. Med. Chem*. **2000**, *7*, 479-498.

102.) Adams, R., Geissman, T. A.; Edwards, J. D. Gossypol a Pigment of Cottonseed. *Chem. Rev*. **1960**, *60*, 555-574.

103.) Markman, A. L.; Rzhekhin, V. P. Gossypol and Its Derivatives. Israel Programs for Scientific Translations: Jerusalem 1965, 148.

104.) Ramaswamy, H. N.; O'Connor, R. T. Physical and Chemical Properties of Selected Metal Complexes of Gossypol. *J. Am. Oil Chem. Soc*. **1968**, *45*, 841-844.

105.) Berardi, L. C.; Goldblatt, L. A. *Gossypol in Toxic Constituents of Plant Foodstuffs*; 2nd ed.; Liener, I. E. ed.; Academic Press: New York, 1980; p 184-237.

106.) Ramaswamy, H. N., O'Conner, R. T. Metal Complexes of Gossypol. *J. Agric. Food Chem.* **1969,** *17*, 1406-1408.

107.) Przybylski, P.; Schroeder, G.; Brzezinski, B. Complexes of Schiff Base of Gossypol with 5-Hydroxy-3-oxapentylamine and Ca, Ba, or Pb Cations Studied by NMR, FT-IR, ESI MS, as Well as PM5 Semiempirical Methods. *Ibid*. **2003**, *658*, 115-124.

108.) Brzezinski, B.; Marciniak, B.; Paszyc, S.; Zundel, G. The Tautomerization of Gossypol as a Function of the Presence of Ni, Cu, Zn Cations. *Ibid.* **1992**, *268*, 61-66.

109.) Brzezinski, B.; Rozwadowski, J.; Marciniak, B.; Paszyc, S. Spectroscopic Study of Gossypol-Lanthanide Cation Complexes in Acetonitrile Solution. *J. Mol. Struct*. **1997**, 435, 275-279.

110.) Brezinski, B.; Paszyc, S.; Zundel, G. The Structure of Gossypol as a Function of the Presence of $HAuCl_4$ and of Be Ions. *Ibid*. **1991**, *246*, 45-51.

111.) Zaidi, R., S. M. Hadi. Strand Scission in DNA by Gossypol and Cu (II): Role of Cu(I) and Oxygen-Free Radicals. *J. Biochem. Toxicol*. **1992**, *7*, 213-217.

112.) Zaidi, R.; Hadi, S. M. Complexes Involving Gossypol, DNA and Cu (II). *Biochem. Int*. **1992**, *28*, 1135-1143.

113.) Laatsch, H. Dimeric Naphthaquinones. X. A Convienent Synthesis of Deapogossypolone Tetraethyl Ether. *Anorg. Chem. Org. Chem*. **1984**, *38B(2)*, 244-247.

114.) Edwards, J. D.; Cashaw, J. L. The Synthesis of 1, 2- Dimethoxy-3-isopropylbenzene. *J. Org. Chem*. **1955**, *20*, 847-849.

115.) Manmade, A.; Herlihy, P.; Quick, J.; Duffley, R. P.; Burgos, M.; Hoffer, A. P. Gossypol. Synthesis and in vitro Spermicidal Activity of Isomeric Hemigossypol Derivatives. *Experienta* **1983**, *39*, 1276-1278.

116.) Ognyanov, V. I.; Petrov, O. S.; Tiholov, E. P.; Mollov, N. M. Synthesis of Gossypol Analogues. *Helv. Chim. Acta* **1989**, *72*, 353-360.

117.) Venuti, M. C., Efficient Synthesis of the Gossypol Binaphthyl Backbone. *Ibid*. **1981**, *46*, 3124-3127.

118.) Yu, Y.; Deck, J. A.; Hunsaker, L. A.; Decker, L. M.; Royer, R. E.; Goldberg, E.; Vander-Jagt, D. L. Selective Active Site Inhibitors of Human Lactate Dehydrogenases A4, B4, and C4. *Biochem. Pharmacol*. **2001**, *62*, 81-89.

119.) Meltzer, P. C.; Bickford, P. H.; Lambert, G. J. A Regioselective Route to Gossypol Analogs: The Synthesis of Gossypol and 5, 5' –Didesisopropyl-5,5'-diethyl Gossypol. *Ibid*. **1985**, *50*, 3121-3124.

120.) Meyers, A. I.; Willemsen, J. J. The Synthesis of (S)-(+)-Gossypol. *Tetrahedron Lett.* **1998**, *54*, 10493-10511.

121.) Meyers, A. I.; Willemsen, J. J. An Asymmetric Synthesis of (+)-Apogossypol Hexamethyl Ether. *Tetrahedron Lett*. **1996**, *37*, 791-792.

122.) Meyers, A. I.; Willemsen, J. J. The Synthesis of (S)-(+)-Gossypol via an Asymmetric Ullmann Coupling. *J. Chem. Soc., Chem. Commun*. **1997**, *16*, 1573-1574.

123.) Weber, E.; Josel, H. P. A Propasol for the Classifcation and Nomenclature for Host-Guest-Type Compounds. *J. Inclusion Phenom*. **1983**, *1*, 79-84.

124.) Ibragimov, B. T.; Talipov, S. A.; Aripov, T. F.; Sadykov, A. S. Inclusion Complexes of the Natural Product Gossypol. Crystal Structure of the 2:1 Complex of Gossypol with *m*-Xylene. *J. Inclusion Phenom. Mol. Recognit. Chem*. **1990**, *8*, 323-333.

125.) Green, B. S.; Knossow, M. Lamellar Twinning Explains the Nearly Racemic Composition of Chiral, Single Crystals of Hexahelicene. *Science* **1981**, *214*, 795.

126.) Talipov, S. A.; Ibragimov, B. T.; Nazarov, G. B.; Aripov, T. F.; Sadykov, A. S. An X-ray Structural Investigiation of Gossypol and Its Derivatives. V. Crystal Structures of the Ligroin Modification of Gossypol. Chem. *Abstr*. **1986**, *104*, 139.

127.) Ibragimov, B. T.; Nazarov, G. B.; Talipov, S. A. X-ray Structural Investigation of Gossypol and Its Derivatives. VIII. A New Class of Inclusion Compounds Based on Dianilinegossypol. *Chem. Nat. Compd*. **1988**, *24*, 565-567.

128.) Gdaniec, M.; Ibragimov, B. T.; Dadabaev, B. N. Lattice inclusion compounds of gossypol. Structure of the 2:3 gossypol-benzaldehyde coordinatoclathrate. *Acta Crystallogr., Sect. C: Cryst. Struct. Commun.* **1991**, *47*, 573-577.

129.) Jeffrey, G. A.; Saenger, W. *Hydrogen Bonding in Biological Structures*; Springer: Berlin, 1991; pp 24.

130.) Gdaniec, M.; Czajka, H. Inclusion Compounds of Gossypol. Structure of the Gossypol-n-Valeric Acid (1/2) Coordinato-clathrate. *J. Inclusion Phenom. Mol. Recognit. Chem*. **1995**, *22*, 187.

131.) Gdaniec, M. Lattice inclusion compounds of gossypol. Structure of the 1:2 Gossypol/Salicylaldehyde Coordination Clathrate. *Acta Crystallogr., Sect. C: Cryst. Struct. Commun.* **1991**, *47*, 1499-1503.

132.) Dowd, M.; Stevens, E. *The gossypol-cyclododecanone (1/2) inclusion complex. Acta Crystallogr., Sect. C: Cryst. Struct. Commun*. **2003**, *59*, 397-399.

133.) Gdaniec, M.; Ibragimov, B. T.; Talipov, S. A. In *Gossypol: Solid-state supramolecular chemistry: crystal engineering*, Vol. 6, MacNicol, D.D.; Bishop, T. F., Eds.; Pregamon Press: Oxford, 1996; pp 117-146.

134.) Dowd, M.; Stevens, E. Inclusion complexes of gossypol with 2-pentanone, 3-pentanone and 2-hexanone. *J. Inclusion Phenom. & Macrocyclic Chem*. **2005**, *51*, 65-71.

135.) Dowd, M.; Stevens, E. The (-)-gossypol-2, 4-pentanedione (1:2) inclusion complex. *J. Chem. Crystallogr*. **2004**, *34(8)*, 559-564.

136.) Coppens, P. *X-Ray Charge Densities and Chemical Bonding, (International Union of Crystallographers Text on Crystallography)* USA ed.; Oxford University Press: USA, 1997; pp 1-14.

137.) Vermel, E. M.; Kruglyak, S. A. Anitcancer Activity of Some Alkaloids. *Vopr. Onkol*., **1962**, *8*, 9-17.

138.) Sampath, D. S.; Balaram, P. Resolution of racemic gossypol and interaction of enantiomers with serum albumins and model peptides. *BBA*, **1992**, *882*, 183-186.

139.) Ibragimov, B. T.; Talipov, S. A. Supramolecular Association of Gossypol in the Crystalline State. *J. Struc. Chem*., **1999**, *40(5)*, 686-703.

140.) Dowd, M. K.; Stevens, E. D. Crystal and Molecular Structure of 6,6'-Dimethoxy gossypol:Acetic acid (1:1). *J. Chem. Crystallogr*., **2007**, *37*, 765-770.

141.) Bader, R. F. W. *Atoms in Molecules: A Quantum Theory (International Monograph in Chemistry)*; Oxford University Press: USA, 1994; pp 1-97.

142.) Vahvaselka, A; Kurki-Suonio, K. Analysis of ionic charge distributions in NH_4Cl. *Physica Fennica*, **1975**, *10*, 87-99.

143.) Merisalo, M.; Larsen, F. K.; Kurki-Suonio, K. A low temperature neutron diffraction study of NH_4C. *Physica Fennica,* **1975,** *10*, 199-205.

144.) Stevens, E. D.; Dowd, M. K.; Johnson, G. P.; French, A. D. Experimental and theoretical electron density distribution of α,α-trehalose dihydrate. *Carbohydr Res.*, **2010,** *345(10)*, 1469-81.

145.) Su, Z.; Coppens, P. *Acta Crystallogr., Sect. A* **1992**, *48*, 188-197.

146.) Hübschle, C. B.; Lugar, P. *J. Appl. Crystallogr*., **2006**, *39*, 901-904.

147.) Haleblian, J.; McCrone, W. Pharmaceutical Applications of Polymorphism. *J. Pharm. Sci*., **1969**, *58*, 911-929.

148.) Oddershede, J.; Larsen, S. Charge Density Study of Naphthalene Based on X-ray Diffraction Data at Four Different Temperatures and Theoretical Calculations. *J. Phys. Chem. A*., **2004**, *108(6)*, 1057-1063.

149.) Bader, R. F. W.; Beddall, P. M.; Virial Field Relationship for Molecular Charge Distributions and the Spatial Partitioning of Molecular Properties. *J. Chem. Phys*., **1972**, *56*, 3320.

150.) Bader, R. F. W.; Anderson, S. G.; Duke, A. J. Quantum topology of molecular charge distributions. *J. Am. chem. Soc*., **1979**, *101(6)*, 1389-1395.

151.) Bader, R. F. W.; Essen, H. The Characterization of atomic interactions. *J. Chem. Phys.,* **1984**, *80(5)*, 1943-1960.

152.) Bader, R. F. W.; Tal, Y.; Anderson, S. G.; Nguyen-Dang, T. T. Quantum Topology: Theory of Molecular Structure and its Change. *Israel J. Chem.,* **1980**, *19*, 8-29.

153.) Bader, R. F. W.; Nguyen-Dang, T. T.; Tal, Y. Quantum topology of molecular charge distributions. II. Molecular structure and its change. *J. Chem. Phys.,* **1979**, *70*, 4316.

154.) Cade, P. E.; Bader, R. F. W.; Pelletier, J. Molecular Charge Distributions and Chemical Bonding. V. Molecular Excitation, Ionization, and Electron Attachment. *J. Chem. Phys.*, **1971**, *51*, 3517.

155.) Boyd, R.; Knop, O.; Choi, S. C. Sulfur-sulfur bond lengths, or can a bond length be estimated from a single parameter? *J. Am. chem. Soc.*, **1988**, *110*, 7299-7301.

156.) Cremer, D.; Kraka, E.; Slee, T. S.; Bader, R. F. W.; Lau, C. D. H.; Nguyen-Dang, T. T.; MacDougall, P. J. Description of homoaromaticity in terms of electron distributions. *J. Am. chem. Soc.*, **1983**, *105(150)*, 5069-5075.

157.) Bader, R. F. W. Quantum topology of molecular charge distributions. III. The mechanics of an atom in a molecule. *J. Chem. Phys.,* **1980**, *73*, 2871.

158.) Bader, R. F. W.; Becker, P. Transferability of atomic properties and the theorem of Hohenberg and Kohn. *Chem. Phys. Lett*., **1988**, *148*, 452-458.

159.) Bader, R. F. W.; Nguyen-Dang, T. T. Quantum Theory of Atoms In Molecules-Dalton Revisted. *Adv. Quantum Chem*., **1981**, *14*, 63-124.

160.) Stevens, E. D.; Coppens, P.; Feld, R.; Lehmann, M.S. Electron density in the water molecule in α-oxalic acid dihydrate and the nature of short hydrogen bonds. *Chem. Phys. Lett.,* **1979**, *67*, 541-543.

161.) Stevens, E. D.; Coppens, P. Experimental electron density distributions of the hydrogen bond. High-resolution study of α-oxalic acid dihydrate at 100K., *Acta Cryst.* **1980**, *B36*, 1864–1876.

162.) Stevens, E. D.; Coppens, P. Electron population analysis of accurate diffraction data. VIII. Refinement of metal d-orbital occupancies from X-ray diffraction data. *Acta Cryst.,* **1979**, *A35*, 536.

163.) Hansen, N. K.; Coppens, P. Electron population analysis of accurate diffraction data. VI. Testing aspherical atom refinements on small-molecule data sets, N. K. Hansen and P. Coppens, *Acta Cryst.,* **1978**, *A34*, 909–921.

164.) Stevens, E. D.; Rys, J.; Coppens, P. Quantitative comparison of theoretical calculations with the experimentally determined electron density distribution of formamide. *J. Am. Chem. Soc.* **1978**, *100*, 2324–2328.

165.) Coppens, P.; Hansen, N. K. The combination of aspherical-atom least-squares refinements with Fourier Methods. *Israel J. Chem.,* **1977**, *16*, 163.

166.) Coppens, P.; Stevens, E. D. Static versus dynamic densities. *Israel J. Chem.,* **1977**, *16*, 175.

167.) Stevens, E. D.; Lehmann, M. S.; Coppens, P. Experimental electron density distribution of sodium hydrogen diacetate. Evidence for covalency in a short hydrogen bond. *J. Am. Chem. Soc.,***1977***, 99*, 2829.

168.) Lehmann, M. S.; Coppens, P. An estimate of the effect of series termination on deformation density peak heights. *Acta Chem. Scand.,* **1977**, *A31*, 530.

169.) Coppens, P. Overcoming the free-atom bias with modified least-squares formalisms. *Israel J. Chem.,* **1977**, *16*, 159.

170.) Coppens, P.; Yang, Y. W.; Blessing, R. H.; Cooper, W. F.; Larsen, F. K. The experimental charge distribution in sulfur containing molecules: Analysis of cyclic octasulfur at 300 and 1000K. *J. Am. Chem. Soc.,* **1977**, *99*, 760.

171.) Stevens, E. D.; Rys, J.; Coppens, P. Calculation of dynamic electron density distributions from static molecular wavefunctions. *Acta Cryst.,* **1977**, *A33*, 333.

172.) Bats, J. W.; Coppens, P. The experimental charge distribution in sulfur containing molecules: A study of the deformation density in NH_4SCN at 81K by combined X-ray and neutron diffraction. *Acta Cryst.,* **1977**, *B33*, 1542.

173.) Bats, J. W.; Coppens, P.; Kvick, A. The experimental charge distribution in sulfur containing molecules: Structure determination and electron density study of NaSCN at reduced temperatures. *Acta Cryst.,* **1977**, *B33*, 1534.

174.) Rys, J.; King, H. F.; Coppens, P. Fitting atomic scattering factors to molecular charge distributions. *Chem. Phys. Lett.*, **1976**, *41*, 383.

175.) Stevens, E. D.; Coppens, P. A priori estimates of the errors in experimental electron densities. *Acta Cryst.,* **1976**, *A32*, 915–917.

176.) Bats, J. W.; Coppens, P.; Koetzle, T. F. The experimental charge distribution in sulfur containing molecules: A study of the deformation density in sulfamic acid at 78K by X-ray and neutron diffraction. *Acta Cryst.,* **1977**, *B33*, 37–45.

177.) Becker, P. J.; Coppens, P. Extinction within the limit of validity of the Darwin transfer equations. III. Non-spherical crystals and anisotropy of extinction. *Acta Cryst.,* **1975**, *A31*, 417.

178.) Stevens, E. D.; Coppens, P. Experimental measurements of the X-ray scale factor for charge density studies. *Acta Cryst.,* **1975**, *A31*, 612.

179.) Griffin, J. F.; Coppens, P. The valence electron distribution in a-Perdeutero glycylglycine: A high-resolution study of the peptide bond. *J. Am. Chem. Soc.,* **1975**, *97*, 3496–7604.

180.) Coppens, P. Charge transfer in TTF-TCNQ by direct integration of X-ray diffraction amplitudes. *Phys. Rev. Lett.,* **1975**, *35*, 98.

181.) Coppens, P.; Stevens, E. D. Accurate X-ray diffraction and quantum chemistry: The study of charge density distributions. *Advances in Quantum Chem.,* **1977**, *10*, 1–35.

182.) Coppens, P.; Ross, F. K.; Blessing, R. H.; Cooper, W. F.; Larsen, F. K.; Leipoldt, J. G.; Rees, B.; Leonard, R. A cryostat for collection of three-dimensional diffractometer data at liquid helium temperature. *J. Appl. Cryst.,* **1974**, *7*, 315–319.

183.) Becker, P. J.; Coppens, P.; Ross, F. K. The valence electron distribution in cubic tetracyanoethylene by the combined use of X-ray and neutron diffraction. *J. Am. Chem. Soc.,* **1973**, *95*, 7604.

184.) Coppens, P. Some implications of combined X-ray and neutron diffraction studies. *Acta Cryst.,* **1974**, *B30*, 255.

185.) Blessing, R. H.; Coppens, P.; Becker, P. Computer analysis of step-scanned X-ray data. *J. Appl. Cryst.,* **1974**, *7*, 488.

186.) McIver, J. W.; Coppens, P.; Nowack, D. Charge densities and bond order for zero differential overlap wavefunctions: Comparison with *ab-initio* calculations and diffraction results. *Chem. Phys. Lett.,* **1971**, *11*, 82.

187.) Cooper, W. F.; Kenny, N. C.; Edmonds, J. W.; Nagel, A.; Wudl, F.; Coppens, P. Crystal and molecular structure of the aromatic sulfur compound, bis-1,3-dithiole: Evidence for d-orbital participation in bonding. *Chem. Comm.*, **1971**, *889***,** 1.

188.) Coppens, P. The use of a polarized hydrogen atom in X-ray structure refinement. *Acta Cryst*., **1972**, *B28*, 1648.

189.) Coppens, P.; Cooper, W. F. Charge distribution in the light atom mineral kernite. *Science* **1972**, *176*, 165.

190.) Jones, D. S.; Pautler, D.; Coppens, P. Electron population analysis of accurate diffraction data. IV. Evaluation of two-center formalisms. *Acta Cryst*., **1972**, *A28*, 635.

191.) Coppens, P.; DeMeulenaer, J.; Tompa, H. A comparison of analytical and numerical methods for the evaluation of the absorption correction in crystal structure analysis. *Acta Cryst.,* **1967**, *22*, 601.

192.) Coppens, P.; Coulson, C. A. The effect of asymmetry on the atomic charge distribution on the positions of terminal atoms as determined with X-rays. *Acta Cryst.,* **1967**, *23*, 718.

193.) Coppens, P. Comparative X-ray and neutron diffraction study of bonding effects in s-Triazine. *Science* **1967**, *158*, 1577–1579.

194.) Coppens, P.; Hamilton, W. C. Errors in electron density maps and the use of integrated densities in the study of charge density distributions. *Acta Cryst.,* **1968**, *B24*, 925.

195.) Coppens, P. Errors in the calculated structure factors caused by the spherical form factor model. *Acta Cryst.,* **1969**, *A25*, 180.

196.) Coppens, P.; Sabine, T. M. Neutron diffraction study of hydrogen bonding and thermal motion in deuterated α and β oxalic acid dehydrate. *Acta Cryst.,* **1969**, *B25*, 2442-2451.

197.) Coppens, P.; Sabine, T. M.; Delaplane, R. G.; Ibers, J. A. An experimental determination of the asphericity of the atomic charge distribution in oxalic acid dihydrate. *Acta Cryst.,* **1969**, *B25*, 2451–2458.

198.) Tanaka, K.; Elkaim, E.; Li, L.; Jue, Z. N.; Coppens, P.; Landrum, L. Electron density studies of porphyrins and phthalocyanines. IV. Electron density distribution in crystals of (meso-tetraphenylporphinato)iron(II). *J. Chem. Phys.,* **1986**, *84*, 6969–6978.

199.) Elkaim, E.; Tanaka, K.; Coppens, P.; Scheidt, W. R. Low temperature study of bis(2-methylimidazole)(octathylporphinato) iron(III) perchlorate. *Acta Cryst.,* **1987**, *B43*, 457–461.

200.) Paturle, A.; Coppens, P. Normalization factors for spherical harmonic density functions. *Acta Cryst.,* **1988**, *A44*, 6–7.

201.) Mallinson, P. R.; Koritsansky, T.; Elkaim, E.; Li, N.; Coppens, P. The Gram-Charlier and multipole expansions in accurate X-ray diffraction studies: can they be distinguished? *Acta Cryst.,* **1988**, *A44*, 336–343.

202.) Petricek, V.; Coppens, P. Structure analysis of modulated molecular crystals III: scattering formalism and symmetry considerations: extension to higher dimensional space groups. *Acta Cryst.,* **1988**, *A44*, 235–239.

201.) Umland, S.; Allie, S.; Kuhlmann, T.; Coppens, P. Relation between geometry and charge transfer in low-dimensional organic salts. *J. Phys. Chem.,* **1988**, *92*, 6456–6460.

202.) Coppens, P.; Lee, P.; Gao, Y.; Sheu, H. S. Application of the Selective Atom Diffraction method to the cation distribution in high Tc bismuth cuprates. *J. Phys. Chem. Solids,* **1991**, *52*, 1267–1272.

203.) Su, Z.; Coppens, P. On the mapping of electrostatic properties from the multipole description of the charge density. *Acta Cryst.,* **1992**, *A48*, 188–197.

204.) Cisarova, I.; Maly, K.; Petricek, V.; Coppens, P. On the use of Fourier methods in the analysis of composite structures. *Acta Cryst.,* **1993**, *A49*, 336–341.

205.) Stweart, R. F.; Feil, D. A Theoretical Study of Elastic X-Ray Scattering. *Acta Cryst*., **1980**, *A36*, 503.

206.) Savariault, J. M.; Lehmann, M. S. Experimental determination of the deformation electron density in hydrogen peroxide by combination of x-ray and neutron diffraction measurements. *J. Am. Chem. Soc.*, **1980**, *102*, 1298-1303.

207.) Harel, M.; Hirshfeld, F. L. Difference densities by least-squares refinement. II. Tetracyanocyclobutane. *Acta Cryst*., **1975**, *B31*, 162-172.

208.) **SAINT**, **SADABS**: Bruker-AXS, Madison, WI, USA, **1996**.

209.) Sheldrick, G. M. *Acta Crystallogr. Sect. A,* **2008**, *64*, 112-122.

210.) Spek, A. L. *J. Appl. Crystallogr*., **2003**, *36*, 7-13.

VITA

The author was born in La Cieba, Honduras. Carlos A. Zelaya served as a flight medic in the U.S. Army for six years. He received bachelor degrees in molecular biology and chemistry (chemical physics) from the University of New Orleans in 2005. He joined the University of New Orleans graduate school in chemistry to pursue a masters and Ph.D in physical chemistry. He joined Professor Edwin Stevens' research group at the University of New Orleans and Dr. Michael Dowd's research labs at the USDA in 2006 and received his masters in physical chemistry in 2011.